

**Tool Wear Improvement and Machining Parameter  
Optimization in Non-generated Face-hobbing of Bevel Gears**

Mohsen Habibi

A Thesis  
In the Department  
of  
Mechanical and Industrial Engineering

Presented in Partial Fulfillment of the Requirements  
For the Degree of

Doctor of Philosophy (Mechanical Engineering) at

Concordia University  
Montreal, Quebec, Canada

May 2016

© Mohsen Habibi, 2016

**CONCORDIA UNIVERSITY  
SCHOOL OF GRADUATE STUDIES**

This is to certify that the thesis prepared

By: Mohsen Habibi

Entitled: Tool Wear Improvement and Machining Parameter

Optimization in Non-generated Face-hobbing of Bevel Gears

and submitted in partial fulfillment of the requirements for the degree of

complies with the regulations of the University and meets the accepted standards with respect to originality and quality.

Signed by the final examining committee:

|                               |                     |
|-------------------------------|---------------------|
| <u>Lan Lin</u>                | Chair               |
| <u>Deyi Xue</u>               | External Examiner   |
| <u>Liangzhu Wang</u>          | External to Program |
| <u>Sivakumar Narayanswamy</u> | Examiner            |
| <u>Wen Fang Xie</u>           | Examiner            |
| <u>Zezhong Chevy Chen</u>     | Thesis Supervisor   |

Approved by

Martin Pugh / Ali Dolatabadi  
Chair of Department or Graduate Program Director

Amir Asif  
Dean of Faculty

*Dedicated to my family*

## Abstract

Face-hobbing is the dominant and the most productive machining process for manufacturing bevel and hypoid gears. Bevel gears are one of the most important power transmission components, in automobile to aerospace industries, where the power is transmitted between two non-parallel axes. In current industries, the face-hobbing process confronts two major challenges, the tool wear and trial and error experiments to select machining parameters. In the present work, these two problems are targeted.

The tool wear in face-hobbing happens at the tool corners of the cutting blades due to the multi-flank chip formation and large gradient of working rake and relief angles along the cutting edge at the corners. In addition, the cutting fluid absence contributes in the tool wear phenomena. In the present work, a cutting tool design method is proposed in order to improve the tool wear characteristics especially at the tool corners. The rake and relief surfaces of the conventional cutting blades are re-designed in such a way that normal rake and relief angles during the face-hobbing process are kept constant and consequently the gradients of these two angles are minimized, theoretically to zero. Using mathematical tool wear characterization relationship and also FEM simulation, the improvements in tool wear are approved.

In addition, in the present thesis, semi-analytical methods are proposed to optimize the face-hobbing process in order to select appropriate machining settings. The optimization problem is constructed in such a way that the machining time is minimized subject to the tool rake wear or cutting force related constraints. In order to predict the tool rake wear (crater wear depth), methods are proposed to calculate un-deformed chip geometry, cutting forces, normal stresses, interface cutting temperature and chip sliding velocity.

The un-deformed chip geometry is obtained using two proposed methods numerically and semi-analytically. In the numerical method, the workpiece in-process model is obtained and then the un-deformed chip geometry is approximated using the in-process model. In the semi-analytical method, an un-deformed chip boundary theory is constructed in such a way that the boundary curves of the un-deformed chip are formulated by closed form equations.

The obtained un-deformed chip geometry is discretized along the cutting edge of the blades. Each infinitesimal element is considered as a small oblique cut. The differential cutting forces are

predicted for each individual element using oblique cutting transformation theory. The total cutting forces are derived by integrating the differential cutting forces along the cutting edge.

The proposed methods are applied on case studies of non-generated face-hobbing of gears to show the capability of the methods to find the un-deformed chip geometry, predict cutting forces and finally find the optimum machining parameters in non-generated face-hobbing.

## Preface

This thesis is an integrated, manuscript-based thesis as defined in 2013 Thesis Preparation, Examination Procedures and Regulations of School of Graduate Studies of the Concordia University. It consists of the following peer-reviewed journal articles (published or currently under review):

1. Habibi, M., Chen, Z.C., 2016, “A Semi-analytical Approach to Un-deformed Chip Boundary Theory and Cutting Force Prediction in Face-hobbing”, *Computer Aided Design*, 73, pp. 53-65, doi: 10.1016/j.cad.2015.12.001.
2. Habibi, M., Chen, Z.C., 2015, “An Accurate and Efficient Approach to Un-deformed Chip Geometry in Face-hobbing and its Application in Cutting Force Prediction”, *ASME Journal of Mechanical Design*, 138(2):023302-023302-11, doi: 10.1115/1.4032090.
3. Habibi, M., Chen, Z.C., 2015, “A New Approach to Blade Design with Constant Rake and Relief Angles for Face-hobbing of Bevel Gears”, *ASME Journal of Manufacturing Science and Engineering*, 138(3):031005-031005-16, doi: 10.1115/1.4030936.
4. Habibi, M., Chen, Z.C., 2016, “Machining Setting Optimization for Formate® Face-hobbing of Bevel Gears with the Tool Wear Constraint”, *ASME Journal of Mechanical Design*, Submitted.

The body of this thesis consists of Chapters 3-7, in which the above-listed papers are reproduced in such a way that the flow of the contents is organized logically.

## Acknowledgment

During my Ph.D. studies, I have been privileged to work closely with leading researchers in my field of study who I used to always see their names on the cover of key and pioneer literature. Their kind help and consultation paved the jagged research path for me and shed light on the dark and obscure research areas which led to real meaningful academic and industrial contributions.

First of all, I would like to thank my supervisor, Dr. Zezhong Chevy Chen, deeply for his supports during the past four years of my Ph.D. studies. In my opinion, the bed rock of any Ph.D. thesis is casted in the first days when the thesis topic is going to be defined by a supervisor. Dr. Chen's deep knowledge about technology boundaries, which led to his wise choice of my Ph.D. thesis topic, was the most important component in my studies. In addition, his constant feedbacks and suggestions about every step in my thesis helped me to compensate myself to be on the right path.

I would like to express my appreciation to Dr. Hermann J. Stadtfeld, Vice President of Research and Development Center of Gleason Co (Rochester, NY, USA), for his generous supports from my very first year of Ph.D. studies. His perpetual help and supports have been always a relief for me in hardships of the research. As the worldwide leading scientist in gear manufacturing, he has been providing essential information and crucial advices which facilitate the development of the present work. Without his supports, much of the present work could not be accomplished as successfully as it is. His positive comments on my research were my main motivation to continue my work more seriously and his sharp critics always assisted me to take a new direction and modify my work.

I am also thankful for Dr. Yusuf Altintas's generous help from University of British Columbia (Vancouver, BC, Canada). Almost in every paper that I have published so far, I have used his fundamental methods in cutting force prediction and machining theory. In the optimization part of my thesis, he provided me generously several important experimental coefficients. Without those data, the optimization section of the present thesis would not be developed and completed thoroughly.

I am so grateful for Dr. Claude Gosselin's kind help and supports, President at Involute Simulation Softwares Inc. (Quebec City, QC, Canada). He spent time and efforts to run several simulations on his own software, HyGEARS®, and provided me some vital machine settings for face-hobbing of bevel gears. Those data were the core input throughout the proposed methods in the present thesis. His kind and friendly manner made me feel comfortable to ask him to provide required information in areas that were not the focus of the present thesis and saved a lot of energy to concentrate on the main theme of my work.

Finally, I am a debtor to my family who always provide me with their unconditional supports throughout my undergraduate and graduate studies. I would like to thank them for their patience and kindness.

Mohsen Habibi

2<sup>nd</sup> April, 2016



# Contents

|  |      |
|--|------|
| Chapter 1 Introduction .....   | 1—1  |
| 1.1 Motivation .....   | 1—2  |
| 1.2 Thesis objectives.....   | 1—3  |
| 1.3 Approach .....   | 1—3  |
| 1.4 Outline of the thesis.....   | 1—4  |
| Chapter 2 Literature Review .....  | 2—5  |
| <b>2.1 The cutting system and machine geometry</b> .....   | 2—6  |
| 2.2 Tool wear .....  | 2—8  |
| 2.3 In-process CAD model and un-deformed chip geometry.....  | 2—9  |
| 2.4 Cutting force prediction.....  | 2—10 |
| 2.5 Machining parameters optimization .....  | 2—11 |
| Chapter 3 Mathematical Representation of the Cutting System Geometry, Machine Tool Kinematic Chain and the Workpiece ..... | 3—12 |
| 3.1 Introduction .....   | 3—12 |
| <b>3.2 Cutting system</b> .....  | 3—13 |
| 3.2.1 Mathematical representation of the blade geometry .....  | 3—14 |
| 3.2.2 Cutting edge and rake face .....   | 3—14 |
| 3.2.3 Relief Surfaces .....  | 3—21 |
| 3.2.4 Cutter head .....  | 3—23 |
| 3.3 Kinematic structure of Formate™ (non-generated) face-hobbing and workpiece setup .....                                 | 3—25 |
| 3.4 Workpiece discretization .....   | 3—30 |
| 3.5 Conclusion.....  | 3—31 |
| Chapter 4 Tool Wear Characterization and Improvement .....   | 4—32 |
| <b>4.1 Introduction</b> .....  | 4—32 |

|  |  |      |
|--|--|------|
| 4.2  | Working rake and relief angles.....                                | 4—33 |
| 4.3  | Tool wear characterization in gear cutting.....                    | 4—37 |
| 4.4  | The proposed method to design the blades.....                      | 4—39 |
| 4.5  | Validation.....  | 4—44 |
| 4.6  | Conclusion.....  | 4—52 |
| Chapter 5 Workpiece in-process model and un-deformed Chip Geometry in Face-hobbing of Bevel Gears..... |  |      |
|  |  | 5—54 |
| <b>5.1</b>   | <b>Introduction</b> .....  | 5—54 |
| 5.2  | Numerical Approach.....  | 5—56 |
| 5.2.1  | In-process Model.....  | 5—56 |
| 5.2.2  | Chip geometry.....   | 5—59 |
| 5.2.3  | Case study.....  | 5—62 |
| 5.3  | Analytical Approach.....   | 5—63 |
| 5.3.1  | Projection of un-deformed chip geometry on rake face, $Ch_p$ ..... | 5—63 |
| 5.3.2  | Case study.....  | 5—71 |
| Chapter 6 Cutting Force Prediction.....  |  |      |
|  |  | 6—73 |
| 6.1  | Cutting force calculation.....                                     | 6—73 |
| <b>6.2</b>   | <b>Case Studies using numerical un-deformed chip</b> .....         | 6—78 |
| <b>6.2.1</b>   | <b>Case study I</b> .....  | 6—80 |
| <b>6.2.2</b>   | <b>Case study II</b> .....   | 6—82 |
| <b>6.3</b>   | <b>Case Studies using semi-analytical un-deformed chip</b> .....   | 6—84 |
| <b>6.3.1</b>   | <b>Case study I</b> .....  | 6—84 |
| <b>6.3.2</b>   | <b>Case study II</b> .....   | 6—87 |
| 6.4  | Conclusion.....  | 6—88 |
| Chapter 7 Machining Parameters Optimization based on Cutting Force and Tool Wear Constraints.....      |  |      |
|  |  | 7—90 |
| 7.1  | Introduction.....  | 7—90 |
| 7.2  | Face-hobbing simulation.....                                       | 7—92 |

|  |  |       |
|--|--|-------|
| 7.2.1  | Kinematic chains .....                                       | 7—92  |
| 7.2.2  | Un-deformed chip geometry and cutting force prediction ..... | 7—93  |
| 7.3  | Wear rate model.....   | 7—94  |
| 7.3.1  | Chip sliding velocity, $V_s$ .....                           | 7—94  |
| 7.3.2  | Average normal stress, $\bar{\sigma}_n$ .....                | 7—95  |
| 7.3.3  | Average interface temperature, $\bar{T}_{int}$ .....         | 7—96  |
| 7.4  | Constructing optimization problems .....                     | 7—101 |
| 7.5  | Case studies .....   | 7—104 |
| 7.5.1  | Case I: Optimization considering cutting force limit .....   | 7—105 |
| 7.5.2  | Case II: Optimization considering tool wear.....             | 7—107 |
| 7.6  | Conclusion .....   | 7—109 |
| Chapter 8 Summary, Contributions and Recommendations .....   |  | 8—112 |
| 8.1  | Summary.....   | 8—112 |
| 8.2  | Contributions .....  | 8—114 |
| 8.3  | Future works .....   | 8—114 |
| References .....   |  | 116   |
| Appendix: Permissions to Reproduce Copyrighted Material..... |  | 123   |

## List of Figures

|  |      |
|--|------|
| Fig. 2-1 Face-milling (left) and Face-hobbing(right) [21].   | 2—5  |
| Fig. 2-2 Illustration of the head cutter and blade geometries [21].  | 2—6  |
| Fig. 2-3 Schematic view of a blade group mounted in the head cutter [4].   | 2—7  |
| Fig. 2-4 Head cutter and blades arrangement [1].   | 2—7  |
| Fig. 2-5 Kinematic model of hypoid generators [15].  | 2—8  |
| Fig. 3-1 The cutting system of face-hobbing.   | 3—14 |
| Fig. 3-2 The outside blade.  | 3—15 |
| Fig. 3-3 The blade profile sketched on $XtZt$ for the outside blade.   | 3—16 |
| Fig. 3-4 The illustration of $c_e$ , blade angle ( $\alpha_e$ ) and rake angle ( $k_e$ ) in coordinate system $Se$ .                                 | 3—17 |
| Fig. 3-5 The representation of relief surfaces.  | 3—22 |
| Fig. 3-6 Gouging between the blade and the cutting surface, a) gouging accrued, b) gouging avoided.  | 3—23 |
| Fig. 3-7 The schematic view of the cutter head and the blade orientation.  | 3—24 |
| Fig. 3-8 The illustration of the transformation from $St$ to $Sh$ .  | 3—25 |
| Fig. 3-9 Formate™ machine tool structure and the workpiece setup.  | 3—26 |
| Fig. 3-10 Five cutting surfaces of the outside blade.  | 3—28 |
| Fig. 3-11 The cutting surface of the first rotation.   | 3—29 |
| Fig. 3-12 Discretization of the workpiece along $Z3$ by $\Delta z$ .   | 3—30 |
| Fig. 4-1 Velocity direction.   | 4—34 |
| Fig. 4-2 Derivation of the working rake ( $\gamma$ ) and relief ( $\alpha$ ) angles.   | 4—35 |
| Fig. 4-3 The theoretical cutting velocity, $V_{th}$ .  | 4—36 |
| Fig. 4-4 The working and theoretical rake angles   | 4—38 |
| Fig. 4-5 The working and theoretical relief angles   | 4—38 |
| Fig. 4-6 The proposed method to design the rake and relief surfaces by assigning working rake ( $\gamma$ ) and relief ( $\alpha$ ) angles directly.  | 4—39 |
| Fig. 4-7 The modeled blade using designed rake and relief surfaces, Left: The modeled rake and relief surfaces using generating line ( $V_l$ ).      | 4—43 |
| Fig. 4-8 Measuring the working rake ( $\gamma$ ) and relief ( $\alpha$ ) angles at the corner on (a) the conventional blade, (b) the proposed blade. | 4—45 |

|   |      |
|---|------|
| Fig. 4-9 The working rake ( $\gamma$ ) and relief ( $\alpha$ ) angles along the cutting edge for the conventional and proposed blade.....   | 4—48 |
| Fig. 4-10 FE machining simulations, a and b: Conventional and proposed blade tests modeled in Third Wave®, respectively. c and d: Conventional and proposed blade chip removal simulations in Third Wave®, respectively. .... | 4—50 |
| Fig. 4-11 Temperature distribution in the conventional (left) and proposed (right) blades.....  | 4—51 |
| Fig. 4-12 Mises stress distribution in the conventional (left) and proposed (right) blades.....   | 4—51 |
| Fig. 5-1 The discretized workpiece and cutting surface.....   | 5—56 |
| Fig. 5-2 Intersection between cutting edge and a disk .....   | 5—57 |
| Fig. 5-3 The engagement of two blade groups with $j^{th}$ disk.....   | 5—59 |
| Fig. 5-4 Un-deformed chip geometry derivation .....   | 5—61 |
| Fig. 5-5 An example of un-deformed chip geometry derived using the proposed methods at $\theta=16234$ deg and $BO=7.908$ mm.....  | 5—62 |
| Fig. 5-6 The in-process model of 100 <sup>th</sup> disk for different cutting system rotation angle, $\theta$ , the green area is the removed area. ....  | 5—63 |
| Fig. 5-7 The projection of the un-deformed chip geometry, $Ch_p$ , on the rake plane of the outside blade.....  | 5—65 |
| Fig. 5-8 Workpiece geometry.....  | 5—69 |
| Fig. 5-9 Examples of obtained $Ch_p$ for different $\theta$ (deg) and corresponding un-deformed chip area, $A_c$ (mm <sup>2</sup> ). ....   | 5—72 |
| Fig. 6-1 Differential cutting force components.....   | 6—76 |
| Fig. 6-3 Total cutting force estimated in the workpiece coordinate system in face-hobbing of case I for the outside, O.B. ( $n_b=1$ ) and inside, I.B. ( $n_b=13$ ) blades.....   | 6—81 |
| Fig. 6-4 Total cutting force estimated in the workpiece coordinate system in face-hobbing of case I for the outside, O.B. ( $n_b=1$ ) and inside, I.B. ( $n_b=20$ ) blades.....   | 6—83 |
| Fig. 6-5 The un-deformed chip thickness, $t_h$ , and cutting force distribution along the cutting edge, Top (left and right): Outside blade and Bottom (left and right): Inside Blade.....                                    | 6—84 |
| Fig. 6-6 Total cutting force estimated in the workpiece coordinate system in face-hobbing of case I for the outside blade ( $n_b=1$ ).....  | 6—85 |
| Fig. 6-7 An example of FE analysis (top) and obtained cutting forces (bottom).....  | 6—86 |

|  |       |
|--|-------|
| Fig. 6-8 Total cutting force estimated in the workpiece coordinate system in face-hobbing of case II for the outside blade ( $n_b=1$ ). .....  | 6—87  |
| Fig. 6-9 (a) Un-deformed chip thickness, $t_h$ , (b) Cutting force distribution along the cutting edge. ....   | 6—88  |
| Fig. 7-1 Non-generated (Formate®) face-hobbing kinematics. ....  | 7—93  |
| Fig. 7-2 Crater depth, Left: Measured crater depth, $KT$ , in oblique turning [56] (machining settings: $a_p=1.5\text{mm}$ , $\gamma_n=+1\text{deg}$ , $\lambda_s=+7\text{deg}$ and $\kappa_r=+75\text{deg}$ ), Right: Predicted average crater depth, $\overline{KT}$ (present work). ....            | 7—100 |
| Fig. 7-3 Crater worn volume, Left: measured worn volume, $w_{KT}$ [60] (machining settings: $a_p=3\text{mm}$ , $\gamma_n=-6\text{deg}$ , $\lambda_s=0\text{deg}$ , $\kappa_r=+90\text{deg}$ and $f=0.1\text{mm/rev}$ ), Right: Predicted average worn volume, $\overline{w}_{KT}$ (present work). .... | 7—101 |
| Fig. 7-4 Displacement of the cutter head towards the workpiece ( $BO_0 - BO$ ) with constant (Const. Acc.), linear (Linear Acc.) and optimized linear (Opt. Linear Acc.) acceleration, respectively. 7—  | 106   |
| Fig. 7-5 Predicted cutting forces for constant (Const. Acc.), linear (Linear Acc.) and optimized linear (Opt. Linear Acc.) acceleration, respectively. ....  | 7—107 |
| Fig. 7-6 Maximum average tool wear rate, $\dot{w}$ .....   | 7—108 |
| Fig. 7-7 Left: Tool life, $t_L$ , Right: Number of machined gears, $n_G$ . ....  | 7—109 |

## List of Tables

|   |       |
|---|-------|
| Table 3-1 The parameters describing the blade profile.....  | 3—17  |
| Table 3-2 The cutter head and outer blade parameters and the machine settings.....  | 3—29  |
| Table 4-1 Measured working rake ( $\gamma$ ) and relief ( $\alpha$ ) angles for the conventional and proposed blades..... | 4—47  |
| Table 5-1 The process parameters for case studies. ....   | 5—71  |
| Table 6-1 The process parameters for case studies. ....   | 6—79  |
| Table 7-1 AISI 1045 material properties.....  | 7—97  |
| Table 7-2 Comparison of analytical predicted temperature with finite element and experimental results. ....               | 7—99  |
| Table 7-3 The process parameters for case studies. ....   | 7—105 |
| Table 7-4 Machining settings for case-studies, without and with optimization.....   | 7—105 |

## Nomenclature

|  |   |
|--|---|
| $St, Sm, Sw, Sh, Se$                                     | Tool, machine and workpiece, cutter head and axillary tool coordinate systems           |
| $r_e, \rho, L_1, L_2, L_5, L_6$                          | Blade profile parameters  |
| $K_b, K_e$   | Blade rake angles measured in $Sb$ and $Se$   |
| $\alpha_b, \alpha_e$                                     | Blade angles measured in $Sb$ and $Se$  |
| $h_f$  | Blade height  |
| <b>TT, P</b>   | Tool Tip, Pitch Point   |
| $c_e$  | Connecting vector between <b>P</b> and <b>TT</b>  |
| $\mathbf{n}_e, \mathbf{V}_b, \mathbf{V}_{bw}$            | Normal vector to the rake face in coordinate systems, $Se, Sh$ and $Sw$                 |
| $s$  | Curve parameter for blade profile and cutting edge                                      |
| $H, V_p, \lambda_m, \Delta X_p$                          | Machine settings: horizontal, vertical, root angle and center to back                   |
| $N_g$  | Number of gear teeth  |
| $N_b$  | Number of blade groups  |
| $n_b$  | Blade group number  |
| $R_b$  | workpiece rotation ratio  |
| $\theta$   | cutter head rotation angle  |
| $\omega_H$   | Cutter head rotary speed in rpm   |
| $BO$   | cutter head offset  |
| $\mathbf{r}_h, \mathbf{r}_w$                             | Cutting edge in cutter head and workpiece coordinate systems                            |
| $\Gamma, C, F, a, b$                                     | Gear blank dimensions: pitch angle, outer cone distance, face width, addendum, dedendum |
| $\mathbf{W}_1, \mathbf{W}_2, \mathbf{W}_3$               | Peripheral surfaces of the workpiece  |
| $u, \varphi$   | Surface parameters of $\mathbf{W}_1, \mathbf{W}_2, \mathbf{W}_3$                        |
| $Ch_p$   | Projection of un-deformed chip on rake face   |
| $\mathbf{C}_1, \mathbf{C}_2, \mathbf{C}_3, \mathbf{C}_4$ | Boundaries of $Ch_p$  |
| $\mathbf{C}_{41}, \mathbf{C}_{42}, \mathbf{C}_{43}$      | Intersection of rake face with $\mathbf{W}_1, \mathbf{W}_2$ and $\mathbf{W}_3$          |
| $\mathbf{C}_{4E}$  | Active boundary among $\mathbf{C}_{41}, \mathbf{C}_{42}$ and $\mathbf{C}_{43}$          |
| $\mathbf{S}_{EO}, \mathbf{S}_{EI}$                       | Effective cutting surface of outside and inside blades                                  |



|  |  |
|--|--|
| $n_b$  | The number of a blade group that $Ch_p$ is obtained on   |
| $n_{EI}, n_{EO}$                                       | Effective inside and outside blade groups  |
| $p, p_v$   | Perpendicular planes to cutting edge and cutting velocity  |
| $\mathbf{V}$   | Cutting velocity vector  |
| $\mathbf{V}_{pro}$                                     | Projection of $\mathbf{V}$ on plane $p$  |
| $\mathbf{T}_1$   | Cutting edge tangent vector  |
| $\gamma_n$   | Normal rake angle  |
| $\lambda$  | Inclination (oblique) angle  |
| $dA_c$   | Differential un-deformed chip  |
| $\mathbf{C}_{int}$                                     | Intersection of plane $p$ and rake face  |
| $\mathbf{C}_i$   | Cutting edge curve   |
| $\mathbf{C}_h$   | Boundary of $Ch_p$ on rake face  |
| $\mathbf{C}_{ip}, \mathbf{C}_{hp}$                     | Projections of $\mathbf{C}_i$ and $\mathbf{C}_h$ on the rake face, respectively.                   |
| $t_h$  | Un-deformed chip thickness   |
| $ds$   | Length of differential cutting edge element  |
| $K_{tc}, K_{rc}, K_{fc}$                               | Cutting force coefficients   |
| $K_{te}, K_{re}, K_{fe}$                               | Edge cutting coefficients  |
| $\mathbf{P}_e$   | A point on the cutting edge  |
| $\mathbf{n}_{tw}, \mathbf{n}_{rw}, \mathbf{n}_{fw}$    | Unit vectors in directions of the cutting velocity, normal and thrust at $\mathbf{P}_e$ .          |
| $d\mathbf{f}_{tw}, d\mathbf{f}_{rw}, d\mathbf{f}_{fw}$ | Differential cutting forces in directions of cutting velocity, normal and thrust at $\mathbf{P}_e$ |
| $\mathbf{F}_w$   | Total cutting force  |
| $\varphi_n$  | Normal shear angle   |
| $\beta_n$  | Normal friction coefficient  |
| $\tau_s$   | Shear yield stress   |
| $r_c$  | Chip compression ratio   |
| $R_1, R_2$   | Inside and outside radius of disk  |
| $\Delta z$   | Gear blank axial increment   |
| $EE$   | Effecting cutting edge   |

|                                |   |
|--------------------------------|---|
| $SA$                           | Cutter swept area   |
| $BA$                           | Boundary of SA  |
| $CL$                           | Chip line   |
| $Ch_p$                         | Projection of un-deformed chip on rake face   |
| $p, p_v$                       | Perpendicular planes to cutting edge and cutting velocity                               |
| $C_1, C_2, C_3, C_4$           | Boundaries of $Ch_p$  |
| $C_{41}, C_{42}, C_{43}$       | Intersection of rake face with $W_1, W_2$ and $W_3$                                     |
| $C_{4E}$                       | Active boundary among $C_{41}, C_{42}$ and $C_{43}$                                     |
| $f$                            | Feed rate   |
| $w, \dot{w}, \bar{\dot{w}}$    | volume loss per unit area, maximum and average volume loss per unit area per unit time, |
| $\sigma_n, \bar{\sigma}_n$     | local and average normal stress   |
| $V_s$                          | chip sliding velocity relative to the workpiece   |
| $T_{int}^{max}, \bar{T}_{int}$ | Maximum and average interface temperature   |
| $A, B$                         | material constants in Usui's model  |
| $A_l$                          | Chip contact area   |
| $ds_p$                         | Width of cut  |
| $t_m, t_p, t_i$                | Total machining, plunge and finish time   |
| $t_l$                          | Tool life   |
| $KT, \bar{KT}$                 | Crater depth and average crater depth   |
| $n_G$                          | Number of machined gears during tool life   |

# Chapter 1

## Introduction

The main trend towards manufacturing sectors for many industrialized countries have been outsourcing these sectors from other parts of the world where the labor, manufacturing and environmental handling costs are lower. However, this trend has caused many job opportunities for the middle class of the society to disappear and consequently this situation has created a huge economic inequality. The current trend for many world leaders such as in Canada or USA is to bring back manufacturing sectors to their countries to create jobs and hinder the middle class to be disappeared. However, reviving manufacturing industries cause serious problems for industrialized countries. Labor and material costs in these countries are higher than some other parts of the world. Moreover, they need to consider the effect of the manufacturing sectors on the environment more seriously. Considering these limitations, in order to keep up with the rest of the world, brought-back manufacturing industries must be “eco-friendly” and “cost effective” and to do so they need to be “innovative”.

Bevel gears are one of the most important types of gears which have a wide variety of usage in automobile to aerospace industries. These mechanical components used to be manufactured by a machining process called “face-milling”. Because of the indexing and discontinuous nature of the process, the process needed high electrical power and also relatively long machining time. In 2001, the leading manufacturer of gear manufacturing machine tools, Gleason Co. in Rochester, USA, leading by Dr. Stadtfeld invented a process called “dry-cut face-hobbing” for manufacturing bevel gears [1]. Face-hobbing is a dry-cut machining process which means it doesn't use any cutting fluids (eliminating 25,000 liters cutting fluids every day worldwide [2]). The process is continuous and the machining time was so reduced that the process now is known as the most productive process to manufacture bevel gears (Electricity consumption is reduced by approximately 22 Gigawatt hours per year [2]). This process is so dominant in big industries

nowadays in such a way that 90% of bevel gears of BMW company are manufactured using this method.

## **1.1 Motivation**

The first series of academic publications ([3], [4] and [5]) about face-hobbing released almost 5 years after the invention of the method. Therefore, despite other machining processes like milling or turning, face-hobbing is still relatively a new field of study among researchers. Current face-hobbing process encounters two main challenges: selecting machining parameters and tool wear.

The dominant trend in industries to select machining parameters, for face-hobbing and generally in gear manufacturing, is trial and error experiments. Recently, ThirdWave® company has launched a research project for simulating hobbing of helical gears in the commercial finite element software called Advantedge™ [6]. Despite the lack of reliability of FEM results in machining simulation, the long processing time is another issue which hinders FEM methods to be practical in machining industries. In order to select optimal machining parameters, many machining scenarios should be investigated to reach to a desired face-hobbing scenario in the optimization problem. The optimization problem requires a computationally efficient method to handle many iterations that it needs. The present research aims at proposing a computationally efficient method to calculate the un-deformed chip area, predict cutting forces, cutting temperature and estimate the tool wear rate along the cutting edge of the cutting blades. Finally using the estimated tool wear rates for each face-hobbing scenario, the optimal machining settings can be found.

50% of the total cost of gear manufacturing belongs to the cutting system costs [7]. The cutting systems in gear manufacturing also are the most expensive cutters in machining areas. A face-hobbing cutter from Gleason Co. called Pentac® [8] costs around \$16,000 which in machining industries it is a considerable price especially when the cutters need to be re-ground and re-coated so frequently. Face-hobbing is conducted mainly in dry-cut. The tool wear in the absence of cutting fluids would be a serious issue in face-hobbing process. Many experimental observations and research works ([9], [10], [11], [12], [13], [14], [15]) state that the tool corner is the most vulnerable region along the cutting edge of the cutting blades and would be worn faster than the other regions. The present research aims at re-designing the current cutting blades in order to have less tool wear especially at the tool corner.

## 1.2 Thesis objectives

In order to find the optimum face-hobbing scenario and re-design the cutting blades to improve the tool wear characteristics of the cutters, the following six steps should be accomplished one after another:

- 1- Defining the cutting system and machine geometry analytically.
- 2- Characterizing the tool wear and re-designing the cutting tools.
- 3- Approximating in-process CAD model of gears.
- 4- Obtaining un-deformed chip geometry (two methods).
- 5- Predicting cutting forces.
- 6- Optimizing machining settings based on cutting force and tool wear constraints.

## 1.3 Approach

In order to derive the mathematical representation of the cutting edge of the blades in the workpiece coordinate system, series of homogeneous matrix transformations are applied and then this representation is used to find the un-deformed chip geometry during the face-hobbing process. The un-deformed chip geometry is obtained using two methods, numerical and semi-analytical approach. In the numerical approach, the approximation of the workpiece in-process model is obtained and then the un-deformed chip area is calculated using the in-process model. In the semi-analytical approach, a boundary theory of the un-deformed chip is constructed to semi-analytically derive the geometry of the un-deformed chip.

Using the obtained un-deformed chip area and cutting force coefficients, cutting forces are calculated semi-analytically. The method for the force calculation is called “semi-analytical” because the cutting force coefficients need to be estimated by turning experiments. Then using the predicted cutting forces, normal stress along the cutting edge of the cutting blades is calculated. Interface temperature between cutter and the chip is derived using the energy method. Then, the tool wear rate on the rake face is predicted using Usui’s model [16] considering the predicted temperature and normal stress and calculated chip velocity on the rake face of the cutter.

In order to improve the tool wear characteristic, the cutting blade is re-designed in such a way that the normal rake and relief angles along the cutting edge in the face-hobbing process remains constant. In order to do so, rake and relief surfaces of the cutting blades are re-designed by a proposed method to make sure that the gradient of those angles along the cutting edge are kept zero.

#### **1.4 Outline of the thesis**

This chapter introduced the motivation and objectives of the present research. In Chapter 2, the literature review of the face-hobbing is discussed. Chapters 3-7 address the objectives mentioned in Section 1-2 by organizing the contents of the following journal papers:

- 1- [17] Habibi, M., Chen, Z.C., 2016, “A Semi-analytical Approach to Un-deformed Chip Boundary Theory and Cutting Force Prediction in Face-hobbing”, *Computer Aided Design*, 73, pp. 53-65, doi: 10.1016/j.cad.2015.12.001.
- 2- [18] Habibi, M., Chen, Z.C., 2015, “An Accurate and Efficient Approach to Un-deformed Chip Geometry in Face-hobbing and its Application in Cutting Force Prediction”, *ASME Journal of Mechanical Design*, 138(2):023302-023302-11, doi: 10.1115/1.4032090.
- 3- [19] Habibi, M., Chen, Z.C., 2015, “A New Approach to Blade Design with Constant Rake and Relief Angles for Face-hobbing of Bevel Gears”, *ASME Journal of Manufacturing Science and Engineering*, 138(3):031005-031005-16, doi: 10.1115/1.4030936.
- 4- [20] Habibi, M., Chen, Z.C., 2016, “Machining Setting Optimization for Formate® Face-hobbing of Bevel Gears with the Tool Wear Constraint”, *ASME Journal of Mechanical Design*, Submitted.

It should be mentioned that the contents of the papers are arranged in such a way that the reader would be exposed to a reasonable flow of material. Finally, in Chapter 8, the conclusion and future objectives of the present work are discussed.

# Chapter 2

## Literature Review

Bevel and Hypoid gears play vital role in some power transmission systems, such as those of helicopters, power generation machines and automobiles where two non-parallel axes are needed to be connected. Bevel and Hypoid gears are manufactured by two main machining processes (Fig. 2-1), face-milling (developed by Gleason Works) and face-hobbing (developed by Gleason, Oerlikon and Klingelnberg). Face-milling is a single indexing cutting process (only cutter rotates and workpiece is indexed) but face-hobbing is a continuous process (both cutter and workpiece rotate continuously). The manufacturing productivity in face-hobbing is more than face-milling because of the continuous indexing. The cutting tool in face-hobbing is also much more complicated than face-milling process. In other words, face-milling is a special and simple case of face-hobbing [21].

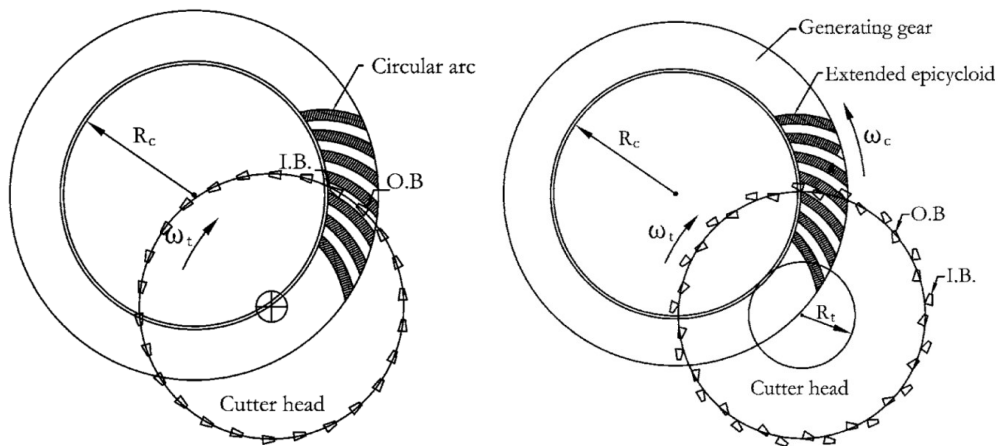


Fig. 2-1 Face-milling (left) and Face-hobbing(right) [21].

The first scientific publications on face-hobbing were released in 2005 by Fan [3] from Gleason Co. and Vimercati [5] in collaboration with FIAT Research Center. In these papers, researchers

tried to find the mathematical equations of the gear and pinion tooth surfaces. Using the kinematic chains of the machine tools and homogenous matrix transformations of the cutting edge of the blades to the workpiece coordinate system, mathematical representation of tooth surfaces have derived.

Both face-hobbing and face-milling can be categorized into non-generated (Formate®) and generated processes. The difference between these two types of processes is the number of active axes involved in the process. In non-generated, two rotary axes and one translational axis are involved while in generated process in order to create a rolling motion of the cutter in the gear or pinion slots, the involved axis could reach to 10 active axes. Gears and pinions are machined usually by non-generated and generated process, respectively.

In order to meet the objectives of the present work, for each objective in Section 1-2, the following literature review have been investigated.

## 2.1 The cutting system and machine geometry

Fan ([3] and [21]), Shih ([4] and [22]), and Vimercati [5] used different cutter systems from Gleason Works and Klingelnberg to represent mathematically the tooth surface of the machined hypoid gear and pinion. Fan ([3] and [21]) used PENTAC® and TRI-AC® cutter system of Gleason to propose a model to describe the surface of the hypoid gear and pinion mathematically. In these articles, cutter system is illustrated by schematic view and described roughly (Fig. 2-2).

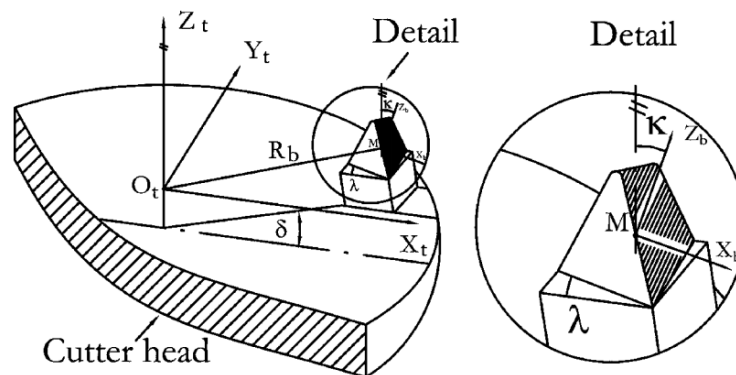


Fig. 2-2 Illustration of the head cutter and blade geometries [21].



Shih ([4] and [22]) used Klingelnberg's cutting system to propose a mathematical model to define surface of the machined hypoid gear. Vimercati [5] used TRI-AC<sup>®</sup> cutter system of Gleason to mathematically represent the surface of face hobbed hypoid gears and pinions. He described the head cutter and cutting blade (Fig. 2-3) and its effective profile in more details than the other papers based on input data to Gleason Special Analysis File<sup>®</sup> (SAF).

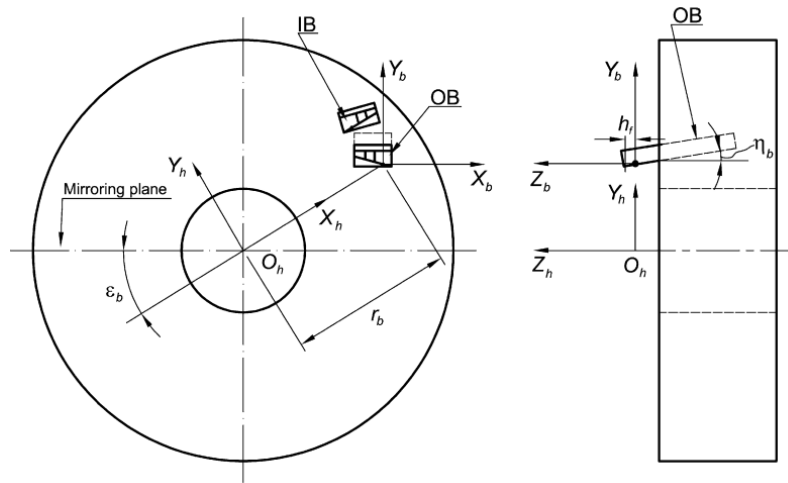


Fig. 2-3 Schematic view of a blade group mounted in the head cutter [4].

Stadtfeld ([1], [15]) explained the geometry of Gleason's face hobbing cutters and cutter head. He described how cutters are mounted on the cutter head and the cutting blades geometry (Fig. 2-4).

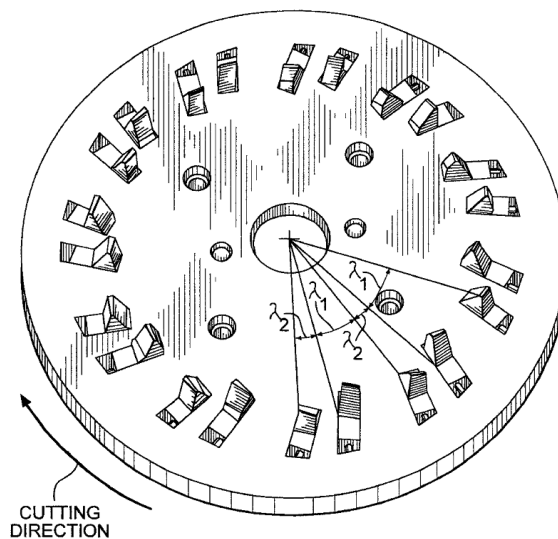


Fig. 2-4 Head cutter and blades arrangement [1].

Fan [21] extracted kinematic chains of general hypoid generators of Gleason Works and used this kinematic chain to estimate the final machined workpiece, gear or pinion (Fig. 2-5).

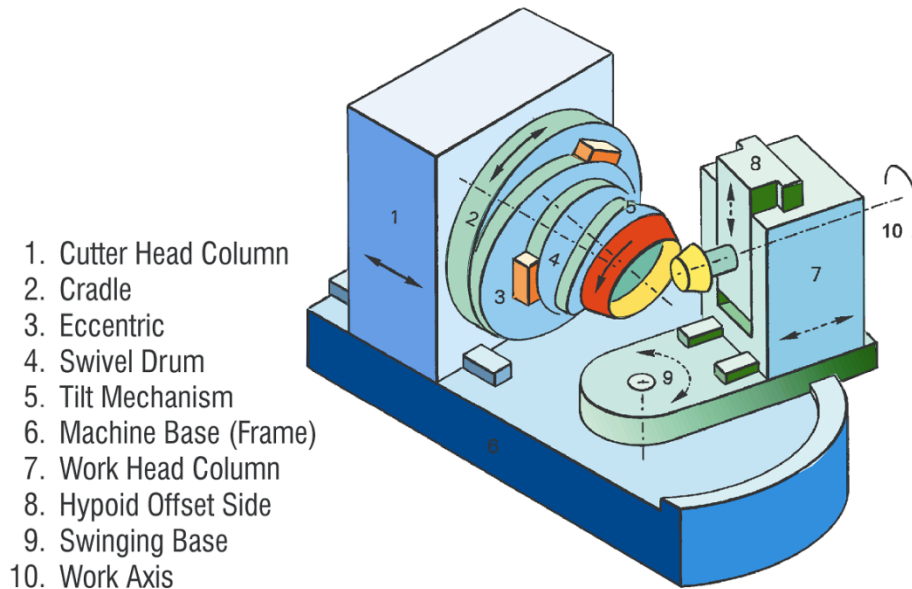


Fig. 2-5 Kinematic model of hypoid generators [15].

The relative movement of cutter and workpiece is as a result of movements and rotations of axis of the machine tools. Defining kinematic chains of a machine tool is the first step to analyze the movements of the axis and their influence on the workpiece. Habibi et al. [23] and Vahebi et al. [24] compensate geometrical and tool deflection errors in 3-axis CNC milling machines based on the kinematic chains of the machine tool that they used and HTM method (Homogenous Transformation Matrix). Their error compensation method is applicable for 5-axis milling machine tools as well. For face hobbing process, each company has their own special machine tools, so the kinematic chains may vary.

## 2.2 Tool wear

In bevel gear manufacturing processes, multi-flank chip formation occurs at corners of the blades of the cutting system which causes the tool wear at the corners ([9], [11], [12], [13], [14] and [15])). This unpredictable local wear decreases the tool life and causes unexpected shut down in the production line and imposes undesired cost to the industries. The purpose of the present research is to investigate generating cutting forces in bevel gear process and predicting and

reducing tool wear and preventing tool breakage. Moreover, by having an understanding of tool wear characteristics, cutting systems (blades and head cutter) can be designed with more sophisticated way than trial and error which currently industries are using.

A few researches have been carried out on the tool wear in bevel gear manufacturing. Klocke et al. ([13] and [14]) and Brecher et al. ([9], [10] and [11]) did important works in this field. They showed that large variations of the working rake and relief angles especially at the corner cause the local tool wear. In addition, they proposed a method to predict the tool wear. Moreover, an equation was introduced which is able to formulate the effecting characteristics in the tool wear. They suggested a method to decrease the tool wear by changing the shape of the gear tooth (consequently the shape of the cutting edge of the blades). In this way, the gear designer needs to compromise between the gear design and the tool wear which means applying limitations on the design process. Even after changing the gear design for the sake of having less tool wear, geometrical related effects on the tool wear still remain.

### **2.3 In-process CAD model and un-deformed chip geometry**

According to literature, there are three types of geometrical simulation of machining: a) image space (image based), b) vector based and c) object space (solid based). Each method has its own advantages and disadvantages with respect to calculation time and accuracy and capability of inspection on the work-piece [25]. Image based methods [26] generally uses graphical tools like Z-Buffer. It shows the machining results graphically so if the view angle changes it has to re-process again. In addition, it is not a simple and appropriate method for numerical inspection (in order to create section through workpiece and dimensions and tolerances inspection) [27]. Vector based or discrete vector methods (DVM) define the work-piece by points and vectors along normal direction of the surface and outward. Z-map method [28] is a special case of DVM where all of the discrete vectors are along Z axis of the Cartesian coordinate system [27]. Using this method, it is not yet possible to obtain the solid model of the machined workpiece directly. Also in some cases where the normal vectors of the surface have severe variation, this method is not suitable [25]. The two previous methods are approximation methods for machining simulation. Solid based methods are so far the exact way to simulate machining and inspect the work-piece accurately but it needs a very high CPU time. There are three methods for solid modeling simulations, Constructive Solid Geometry (CSG), Boundary representation (B-rep) and space

division. Spence and Altintas [29] proposed a simulation system for 2.5 axis milling process by CSG for representing the work-piece. One of the limitations of CSG is the high computational cost during NC code generation, due to thousands of movements required for this process [25]. The simulation cost is reported to be  $O(n^4)$ , where  $n$  is the number of tool movements [30]. Feng [31] used commercial CAD/CAM software CATIA to determine the boundary of engaged surface between the tool and work-piece for 3-axis chip geometry calculations. Using a B-rep solid modeller ball-end milling simulation was reported by Mounayri [32]. The primary disadvantage of B-rep modellers for machining simulation, is the long running time. All of the mentioned researches were on milling and turning process and none of them worked on gear machining. Habibi [33] used CSG and Boolean operation in CATIA to simulate flat and ball end milling in 3-axis CNC machine tools in order to predict cutting forces. It can be seen that, up to now, all the reviewed researches are concentrated on milling.

The only series of researches on gear machining simulation were conducted by Nikolaos and Artomenis [34], Vasilis et al. [35] and Dimitrou and Antoniadis [36]. These researches were concentrated on hobbing process of helical gears. They used CSG and Boolean operation to simulate the process. The final result of these works is the software called “HOB3D” which all the algorithms and methods have been implemented in it.

Based on the literature review, there is no paper on simulation face-hobbing of hypoid gears and deriving in-process CAD model of the workpiece.

## 2.4 Cutting force prediction

The cutting force model proposed by Altintas [37] and Engin and Altintas [38] is the most common method among researches( [23], [39], [40] and [41]). For modeling a typical end mill tool it can be assumed that helical cutting edge is wrapped around the end mill envelop. The differential tangential ( $dF_t$ ), radial ( $dF_r$ ) and axial ( $dF_a$ ) cutting forces acting on an infinitesimal cutting edge segment are given as [38]

$$\begin{cases} dF_t = K_{te} ds + K_{tc} h(\phi_j, \kappa) db \\ dF_r = K_{re} ds + K_{rc} h(\phi_j, \kappa) db , \\ dF_a = K_{ae} ds + K_{ac} h(\phi_j, \kappa) db \end{cases} \quad (2-1)$$

where  $h(\phi_j, \kappa)$  is the uncut chip thickness normal to the cutting edge and varies with the position of the cutting point and cutter rotation. Sub-indices ( $c$ ) and ( $e$ ) represent shear and edge force components, respectively. The edge cutting coefficients  $K_{te}$ ,  $K_{re}$  and  $K_{ae}$  are constants and related to the cutting edge length  $dS$ . The shear force coefficients  $K_{tc}$ ,  $K_{rc}$ ,  $K_{ac}$  are identified either mechanistically from milling tests conducted at a range of feed rate or by a set of orthogonal cutting tests using an oblique transformation method.  $db$  ( $db = dz/\sin \kappa$ ) is the projected length of an infinitesimal cutting flute in the direction along the cutting velocity. Based on the reviewed researches, none of the works estimated cutting force for hobbing cutter for hypoid gear machining.

Based on the literature review, there is no research work on un-deformed chip geometry and cutting force prediction in face-hobbing of bevel gears. In the present work, a method is proposed to derive the un-deformed chip geometry and adopt the semi-analytical model of cutting force prediction in face-hobbing using the derived un-deformed chip geometry and considering the kinematics of the process.

## **2.5 Machining parameters optimization**

Machining parameters optimization has been always the major challenge in machining research areas [42]. However, there is no published research works on machining settings optimization in face-hobbing process. In the present work, a semi-analytical approach is introduced to construct an optimization problem and get the appropriate machining setting based on minimizing the process time subject to some constraints originated in tool wear or cutting forces.

## Chapter 3

# Mathematical Representation of the Cutting System Geometry, Machine Tool Kinematic Chain and the Workpiece

**Citation:** Habibi, M., Chen, Z.C., 2015, “An Accurate and Efficient Approach to Undeformed Chip Geometry in Face-hobbing and its Application in Cutting Force Prediction”, *ASME Journal of Mechanical Design*, 138(2):023302-023302-11, doi: 10.1115/1.4032090.

### 3.1 Introduction

Bevel and Hypoid gears play vital role in some power transmission systems, such as those of helicopters, power generation machines and automobiles where two non-parallel axes need to be connected. Bevel and Hypoid gears are manufactured by two main machining processes, face-milling (developed by Gleason Works) and face-hobbing (developed by Gleason, Oerlikon and Klingelberg). Face-milling is a single indexing cutting process (only cutter rotates and workpiece is indexed) but face-hobbing is a continuous process (both cutter and workpiece rotate continuously). The manufacturing productivity in face-hobbing is more than face-milling because of the continuous indexing. The cutting tool in face-hobbing is also much more complicated than

face-milling process. In other words, face-milling is a special and simple case of face-hobbing [4].

In order to model the cutting blades, mathematical representations of the cutting edge, rake and relief surfaces, the cutter head and kinematic chains of the machine tool are required. Although, many researches on mathematical model of face-milling have been conducted ( [43] and [44]) but a few papers on face-hobbing have been published ( [3], [5], [21], [22] and [45]). These researches proposed methods to represent gear and pinion tooth surfaces mathematically based on kinematic chains and matrix transformations. Fan ( [3] and [21]), Shih ( [4] and [22]), and Vimercati [5] used different cutting system from Gleason Works and Klingelnberg to represent the tooth surface of the machined hypoid gear and pinion mathematically. Fan ( [3] and [21]) used PENTAC<sup>®</sup> and TRI-AC<sup>®</sup> cutter system of Gleason, Shih [4] used Klingelnberg's cutting system and Vimercati [5] used TRI-AC<sup>®</sup> cutting system of Gleason to mathematically represent the surface of face-hobbed hypoid gears and pinions. Vimercati [5] described the cutter head, cutting blade and its effective profile in more details based on input data of Gleason Special Analysis File<sup>®</sup> (SAF). Stadtfeld [15] explained the geometry of Gleason's face hobbing and milling cutting systems. The tool wear characteristics severely depend on the geometry of rake and relief surfaces but none of the mentioned papers has discussed about them. In the present study, full mathematical representations of the cutting blades including the cutting edge and rake and relief surfaces are derived.

In the present chapter, in Section 3.2, the Gleason TRI-AC<sup>®</sup> cutting system is discussed and the mathematical representations of the cutting edge, rake and relief surfaces are presented. In Section 3.3, the kinematic chains of a non-generated face-hobbing machine are discussed and cutting surfaces are generated using the cutting edge geometry and the kinematic chains.

### **3.2 Cutting system**

The cutting system consists of a cutter head and blades. The blades are mounted on the cutter head in slots with special orientations (Fig. 3-1). Two consecutive blades (half profile blades) create a blade group. Gear teeth are machined by the blade groups, convex side of the teeth by the inside blade and concave side by the outside blade. In the following sections, mathematical representations of the Gleason TRI-AC<sup>®</sup> cutting system are discussed.

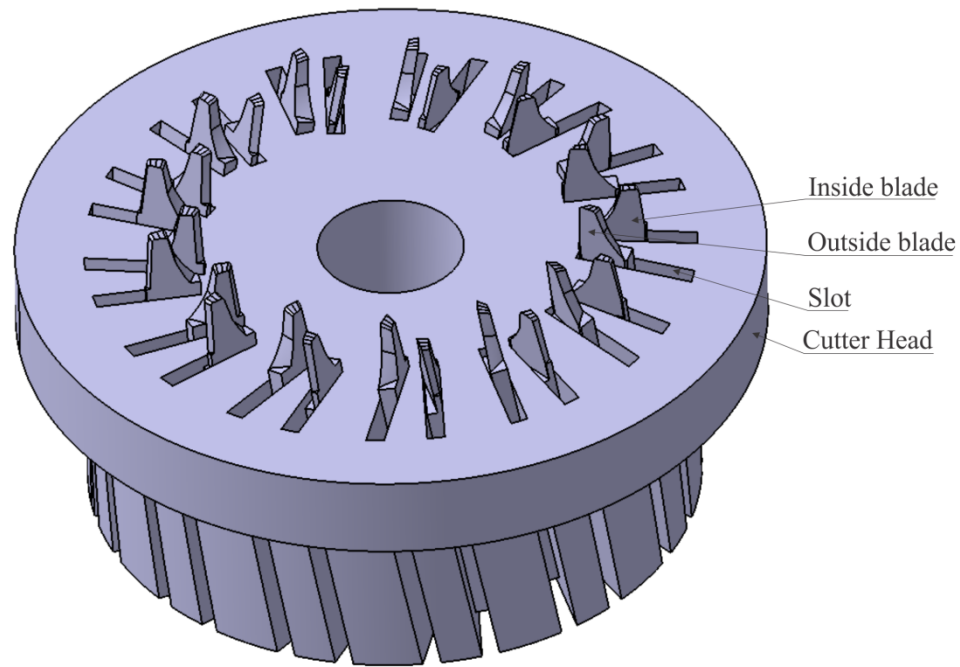


Fig. 3-1 The cutting system of face-hobbing.

### 3.2.1 Mathematical representation of the blade geometry

The procedure to represent the inside blade mathematically is the same as outside blade [5]. Therefore, the present work focuses on the outside blade. Blade geometry consists of three main parts: cutting edge, rake and relief surfaces. In the following sections, the mathematical representations of each part are derived.

### 3.2.2 Cutting edge and rake face

In this section the geometry of the cutting edge of the blades are discussed and the mathematical model of the cutting edge of the blade is derived using references [5] and [45]. Fig. 3-2 shows a view of the cutter blade. The red curve in Fig. 3-2 is the cutting edge of the blade. The successful and accurate modeling of the machining process and deriving cutting surface equations are severely dependent on precisely defining the cutting edge.



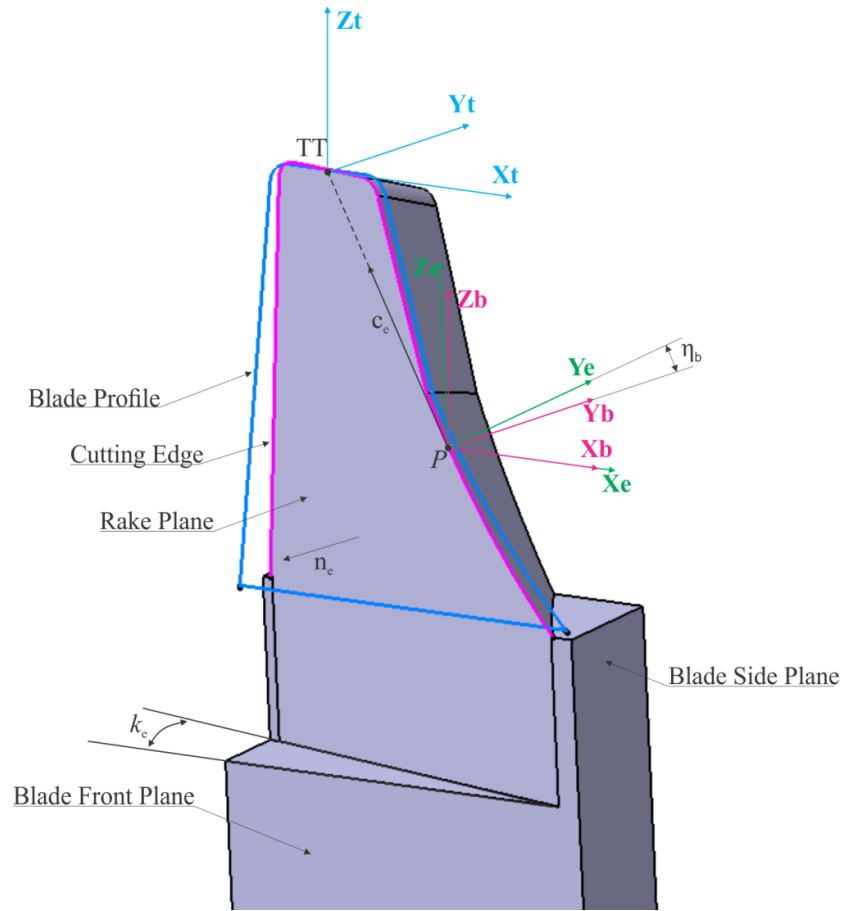


Fig. 3-2 The outside blade.

In order to model the cutting edge, three coordinate systems need to be created. Coordinate system  $S_e$  is defined at point  $P$  in such a way that plane  $Z_e X_e$  is parallel to blade front plane and plane  $Z_e Y_e$  is parallel to blade side plane (Fig. 3-2). Second coordinate system  $S_b$  is created at  $P$ .  $X_e$  and  $X_b$  as well as  $Y_b Z_b$  and  $Y_e Z_b$  are coincident but  $Y_b$  creates an angle with  $Y_e$  in amount of  $-\eta_b$  (hook angle). Third coordinate system  $S_t$  is created at the tool tip ( $TT$ ). The location of  $TT$  is defined by coordinates of  $P$  as

$$P_t = \begin{bmatrix} x_{pt} \\ y_{pt} \\ z_{pt} \\ 1 \end{bmatrix} = \begin{bmatrix} h_f \cdot \tan(\alpha_b) \\ -h_f \cdot \tan(\alpha_b) \cdot \tan(k_b) \\ -h_f \\ 1 \end{bmatrix}, \quad (3-1)$$

where  $k_b$  and  $\alpha_b$  are rake and blade angles measured in  $Sb$ , respectively and  $h_f$  is blade height.

The subscript  $t$  in  $P_t$  shows that  $P$  is calculated in coordinate system  $St$ . In addition, all the axes of  $St$  are parallel to the corresponding axis of  $Sb$ .

A profile called the blade profile, the core for the blade model, is sketched on  $ZtXt$  plane which consists of seven sections: I: Bottom (horizontal line), II: Fillet (circular arc), III: Toperm® (Inclined line), IV: Curved blade (circular arc), VI: Secondary cutting edge (Straight line), VII: Secondary fillet (Circular arc), VIII: Secondary Bottom (horizontal line). Fig. 3-3 shows details of the blade profile.

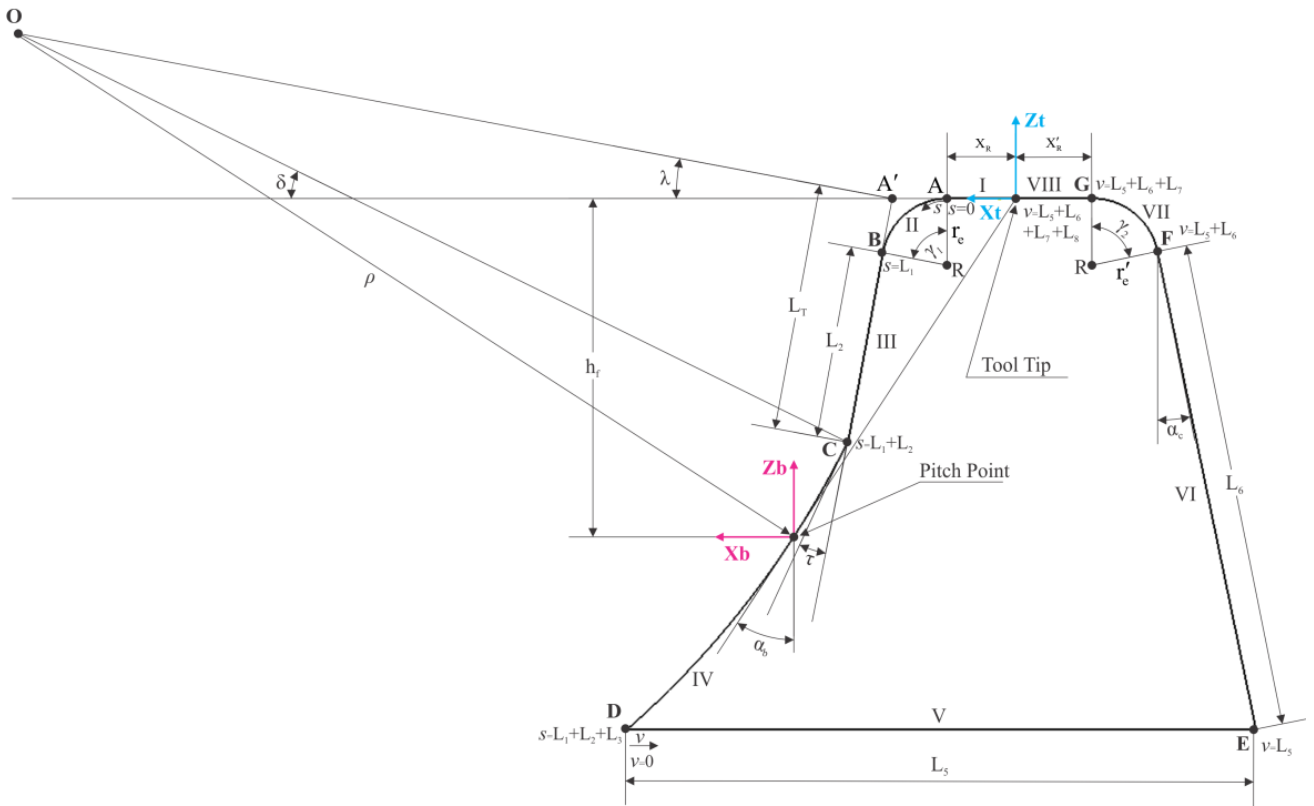


Fig. 3-3 The blade profile sketched on  $XtZt$  for the outside blade.

Table 1 shows parameters needed for drawing the blade profile.

Table 3-1 The parameters describing the blade profile

| Parameters            | Symbols    | Contributing to        |
|-----------------------|------------|------------------------|
| Blade height          | $h_f$      | Main cutting edge      |
| Edge radius           | $r_e$      |                        |
| Toperm length         | $L_T$      |                        |
| Toperm angle          | $\tau$     |                        |
| Radius of curvature   | $\rho$     |                        |
| Blade angle           | $\alpha_b$ |                        |
| Secondary blade angle | $\alpha_c$ | Secondary cutting edge |
| Secondary edge radius | $r'_e$     |                        |

The main cutting which creates gear surfaces (convex and concave surfaces of the gear teeth) is done by the main cutting edge (sections I, II, III and IV in Fig. 3). This cutting edge is in contact with the gear tooth surfaces.

$c_e$  is a directional vector from the pitch point to the tool tip measured in  $Se$  (Fig. 3-2 and Fig. 3-4).

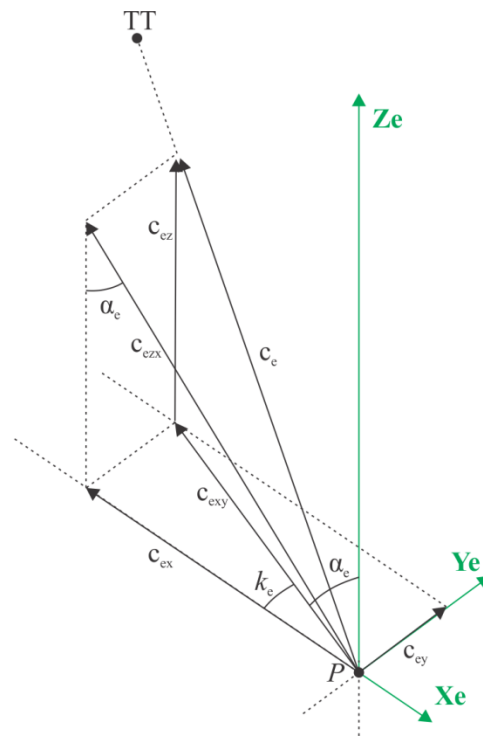


Fig. 3-4 The illustration of  $c_e$ , blade angle ( $\alpha_e$ ) and rake angle ( $k_e$ ) in coordinate system  $Se$ .

$k_e$  and  $\eta_b$  are usually set to  $12^\circ$  and  $4.42^\circ$  for TRI-AC<sup>®</sup> cutting system [11]. Assuming  $c_{ex}$  (Fig. 3-4) is equal to 1, the equation of  $c_e$  is as

$$c_e = \begin{bmatrix} -\sin(\alpha_e) \\ \sin(\alpha_e) \cdot \tan(k_e) \\ \cos(\alpha_e) \\ 1 \end{bmatrix}. \quad (3-2)$$

Then, a connecting vector from the pitch point to the tool tip can be written as

$$c_e^{PT} = (x_{pt}^2 + y_{pt}^2 + z_{pt}^2)^{.5} \cdot c_e / |c_e|. \quad (3-3)$$

$n_e$  is perpendicular to the rake plane and its equation is given by

$$n_e = \begin{bmatrix} -\sin(k_e) \\ -\cos(k_e) \\ 0 \\ 1 \end{bmatrix}. \quad (3-4)$$

The equations of  $c_e$  and  $n_e$  in coordinate system  $Sb$  are as follows:

$$c_b = \begin{bmatrix} 1 & 0 & 0 & 0 \\ 0 & \cos(\eta_b) & -\sin(\eta_b) & 0 \\ 0 & \sin(\eta_b) & \cos(\eta_b) & 0 \\ 0 & 0 & 0 & 1 \end{bmatrix} c_e, \quad (3-5)$$

$$n_b = \begin{bmatrix} 1 & 0 & 0 & 0 \\ 0 & \cos(\eta_b) & -\sin(\eta_b) & 0 \\ 0 & \sin(\eta_b) & \cos(\eta_b) & 0 \\ 0 & 0 & 0 & 1 \end{bmatrix} n_e. \quad (3-6)$$

Using Eq. (3-5) and Eq. (3-6),  $\alpha_b$  and  $k_b$  can be calculated in coordinate system  $Sb$  as

$$\alpha_b = \arctan\left(-\frac{c_{bx}}{c_{bz}}\right), \quad (3-7)$$

$$k_b = \arctan\left(-\frac{c_{by}}{c_{bx}}\right). \quad (3-8)$$

The cutting edge lies entirely on the rake plane. The rake plane passes through the pitch point and the normal vector of this plane is  $n_b$ , so the equation of this plane in  $St$  can be written as

$$(x - x_{pt}) \cdot n_{bx} + (y - y_{pt}) \cdot n_{by} + (z - z_{pt}) \cdot n_{bz} = 0. \quad (3-9)$$

By substituting  $x$  and  $z$  coordinates of the blade profile (Fig. 3-3) in Eq. (3-9) and solving for  $y$ , the equation of  $y$  component of the cutting edge is derived.

Mathematical representations of the cutting edge for each section of the profile blade are as follows:

$$r_t = \begin{bmatrix} x_{1t} \\ y_{1t} \\ z_{1t} \end{bmatrix} = \begin{bmatrix} s + X_R \\ y_{1t} \\ 0 \end{bmatrix}, \quad -X_R \leq s \leq 0, \quad (3-10)$$

$$r_t = \begin{bmatrix} x_{2t} \\ y_{2t} \\ z_{2t} \end{bmatrix} = \begin{bmatrix} X_R + r_e \cdot \sin\left(\frac{s}{r_e}\right) \\ y_{2t} \\ -r_e \cdot \left(1 - \cos\left(\frac{s}{r_e}\right)\right) \end{bmatrix}, \quad 0 \leq s \leq L_1, \quad (3-11)$$

$$r_t = \begin{bmatrix} x_{3t} \\ y_{3t} \\ z_{3t} \end{bmatrix} = \begin{bmatrix} X_R + r_e \cdot \sin\left(\frac{L_1}{r_e}\right) + (s - L_1) \cdot \sin(\delta - \tau) \\ y_{3t} \\ -r_e \cdot \left(1 - \cos\left(\frac{L_1}{r_e}\right)\right) - (s - L_1) \cdot \cos(\delta - \tau) \end{bmatrix}, \quad L_1 \leq s \leq L_1 + L_2, \quad (3-12)$$

$$r_t = \begin{bmatrix} x_{4t} \\ y_{4t} \\ z_{4t} \end{bmatrix} = \begin{bmatrix} x_o - \rho \cdot \cos\left(\delta + \frac{(s-L_1-L_2)}{\rho}\right) \\ y_{4t} \\ z_o - \rho \cdot \sin\left(\delta + \frac{(s-L_1-L_2)}{\rho}\right) \end{bmatrix}, L_1 + L_2 \leq s \leq L_1 + L_2 + L_3, \quad (3-13)$$

$$r_t = \begin{bmatrix} x_{5t} \\ y_{5t} \\ z_{5t} \end{bmatrix} = \begin{bmatrix} x_o - \rho \cdot \cos\left(\delta + \frac{L_3}{\rho}\right) - v \\ y_{5t} \\ z_o - \rho \cdot \sin\left(\delta + \frac{L_3}{\rho}\right) \end{bmatrix}, 0 \leq v \leq L_5, \quad (3-14)$$

$$r_t = \begin{bmatrix} x_{6t} \\ y_{6t} \\ z_{6t} \end{bmatrix} = \begin{bmatrix} x_o - \rho \cdot \cos\left(\delta + \frac{L_3}{\rho}\right) - L_5 + (v-L_5) \cdot \sin(\alpha_c) \\ y_{6t} \\ z_o - \rho \cdot \sin\left(\delta + \frac{L_3}{\rho}\right) + (v-L_5) \cdot \cos(\alpha_c) \end{bmatrix}, L_5 \leq v \leq L_5 + L_6, \quad (3-15)$$

$$r_t = \begin{bmatrix} x_{7t} \\ y_{7t} \\ z_{7t} \end{bmatrix} = \begin{bmatrix} x_o - \rho \cdot \cos\left(\delta + \frac{L_3}{\rho}\right) - L_5 + L_6 \cdot \sin(\alpha_c) + r'_e \cdot \cos\left(\frac{Pi}{2} - \gamma_2\right) - r'_e \cdot \cos\left(\frac{v-L_5-L_6}{re} + \frac{Pi}{2} - \gamma_2\right) \\ y_{7t} \\ z_o - \rho \cdot \sin\left(\delta + \frac{L_3}{\rho}\right) + L_6 \cdot \cos(\alpha_c) + r'_e \cdot \sin\left(\frac{v-L_5-L_6}{re} + \frac{Pi}{2} - \gamma_2\right) - r'_e \cdot \sin\left(\frac{Pi}{2} - \gamma_2\right) \end{bmatrix}, \quad (3-16)$$

$$L_5 + L_6 \leq v \leq L_5 + L_6 + L_7,$$

$$r_t = \begin{bmatrix} x_{8t} \\ y_{8t} \\ z_{8t} \end{bmatrix} = \begin{bmatrix} v - L_5 - L_6 - L_7 - L_8 \\ y_{8t} \\ 0 \end{bmatrix}, L_5 + L_6 + L_7 \leq v \leq L_5 + L_6 + L_7 + L_8, \quad (3-17)$$

$$y_{it} = y_{pt} + \frac{(x_{pt} - x_{it}) \cdot n_{bx} + (z_{pt} - z_{it}) \cdot n_{bz}}{n_{by}}, i=1, \dots, 8. \quad (3-18)$$

### 3.2.3 Relief Surfaces

In order to define exact working rake and relief angles, mathematical representations of the rake and relief surfaces are derived. In addition, in order to prevent gouging of the tool relief surfaces with the machined surface (the cutting surface), knowing the geometry of these surfaces are necessary. For this purpose, the cutting edge equations are transformed to  $Se$  as

$$C_{ei} = M_{et} r_{ti}, i = 1..8, \quad (3-19)$$

where  $C_{ei}$  are the cutting edge equations in  $Se$  and  $M_{et}$  is the transformation matrix given by

$$M_{et} = \begin{bmatrix} 1 & 0 & 0 & C_{ex}^{PT} \\ 0 & \cos(-\eta_b) & -\sin(-\eta_b) & C_{ey}^{PT} \\ 0 & \sin(-\eta_b) & \cos(-\eta_b) & C_{ez}^{PT} \\ 0 & 0 & 0 & 1 \end{bmatrix}. \quad (3-20)$$

The mathematical representations of the relief surfaces ( $ST_i$ ) in Fig. 3-5 are derived using a generating line,  $l$ . The direction vector ( $V_l$ ) of  $l$  is created using two angles  $\alpha_{xy}$  and  $\alpha_{yz}$ , a rotation around  $Ze$  and a rotation around  $Xe$  (Fig. 3-5 (left)) in  $Se$ , respectively. By these two rotations, the formula of  $V_l$  can be obtained as

$$V_l = \begin{bmatrix} 1 & 0 & 0 & 0 \\ 0 & \cos(-\alpha_{yz}) & -\sin(-\alpha_{yz}) & 0 \\ 0 & \sin(-\alpha_{yz}) & \cos(-\alpha_{yz}) & 0 \\ 0 & 0 & 0 & 1 \end{bmatrix} \begin{bmatrix} \cos(\alpha_{xy}) & -\sin(\alpha_{xy}) & 0 & 0 \\ \sin(\alpha_{xy}) & \cos(\alpha_{xy}) & 0 & 0 \\ 0 & 0 & 1 & 0 \\ 0 & 0 & 0 & 1 \end{bmatrix} \begin{bmatrix} 0 \\ 1 \\ 0 \\ 1 \end{bmatrix}. \quad (3-21)$$

Then this vector is translated to a point on the cutting edge so that the equation of the generating line can be written as

$$l = V_l \cdot t + C_e, \quad (3-22)$$

where  $t$  is the line parameter.

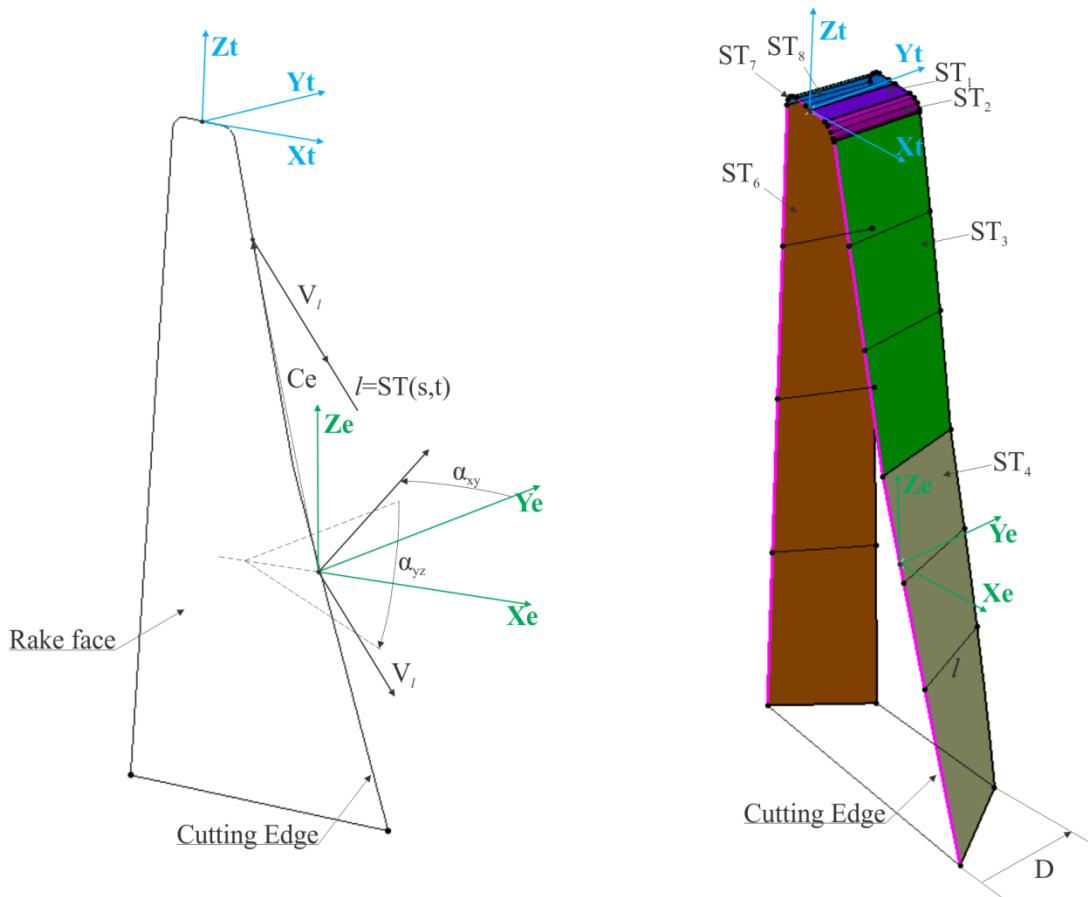


Fig. 3-5 The representation of relief surfaces.

Since  $\alpha_{xy}$  and  $\alpha_{yz}$  vary along the cutting edge by  $s$ , so  $V_l$  is in terms of  $s$ . On the other hand,  $C_e$  is also in terms of  $s$ , therefore,  $l$  is in terms of two independent parameters,  $s$  and  $t$ , which represents a set of equations ( $ST_i$ ) of the relief surfaces. Hence,  $ST_i = l_i$  (Fig. 3-5).

In order to avoid gouging between the blade relief surfaces and the cutting surface, proper  $\alpha_{xy}$ ,  $\alpha_{yz}$  and the blade thickness ( $D$  in Fig. 3-5) should be selected so that during whole machining process there would be no intersection between the relief faces and the cutting surface. In Fig. 3-6.a, the gouging case is shown and in Fig. 3-6.b the proper parameters are chosen which avoids gouging.



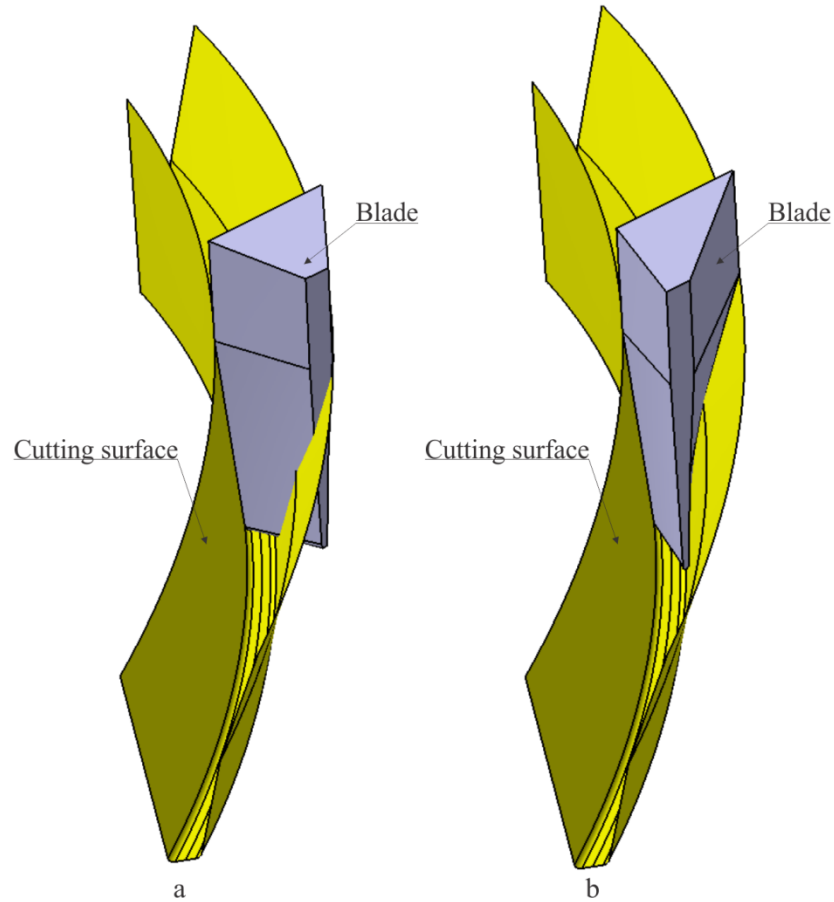


Fig. 3-6 Gouging between the blade and the cutting surface, a) gouging accrued, b) gouging avoided.

$\alpha_{xy}$  and  $\alpha_{yz}$  define the geometry of the relief surfaces and consequently effect on theoretical and working relief angles. In this paper,  $\alpha_{xy}$  and  $\alpha_{yz}$  are assumed linear and constant along the cutting edge, respectively.

### 3.2.4 Cutter head

The cutter head (Fig. 3-1) has  $N_b$  blade groups around the cutting head axis ( $Zh$  in Fig. 3-7). Each blade is mounted in a slot. By defining six angles ( $\lambda_1, \lambda_2, \lambda_3, \lambda_4, \lambda_5$  and  $\eta_b$ ), the slot orientation on the cutter head is defined (Fig. 3-7). The pitch points of the inside and outside blades are located on the reference circle with radius  $r_b$  [13].

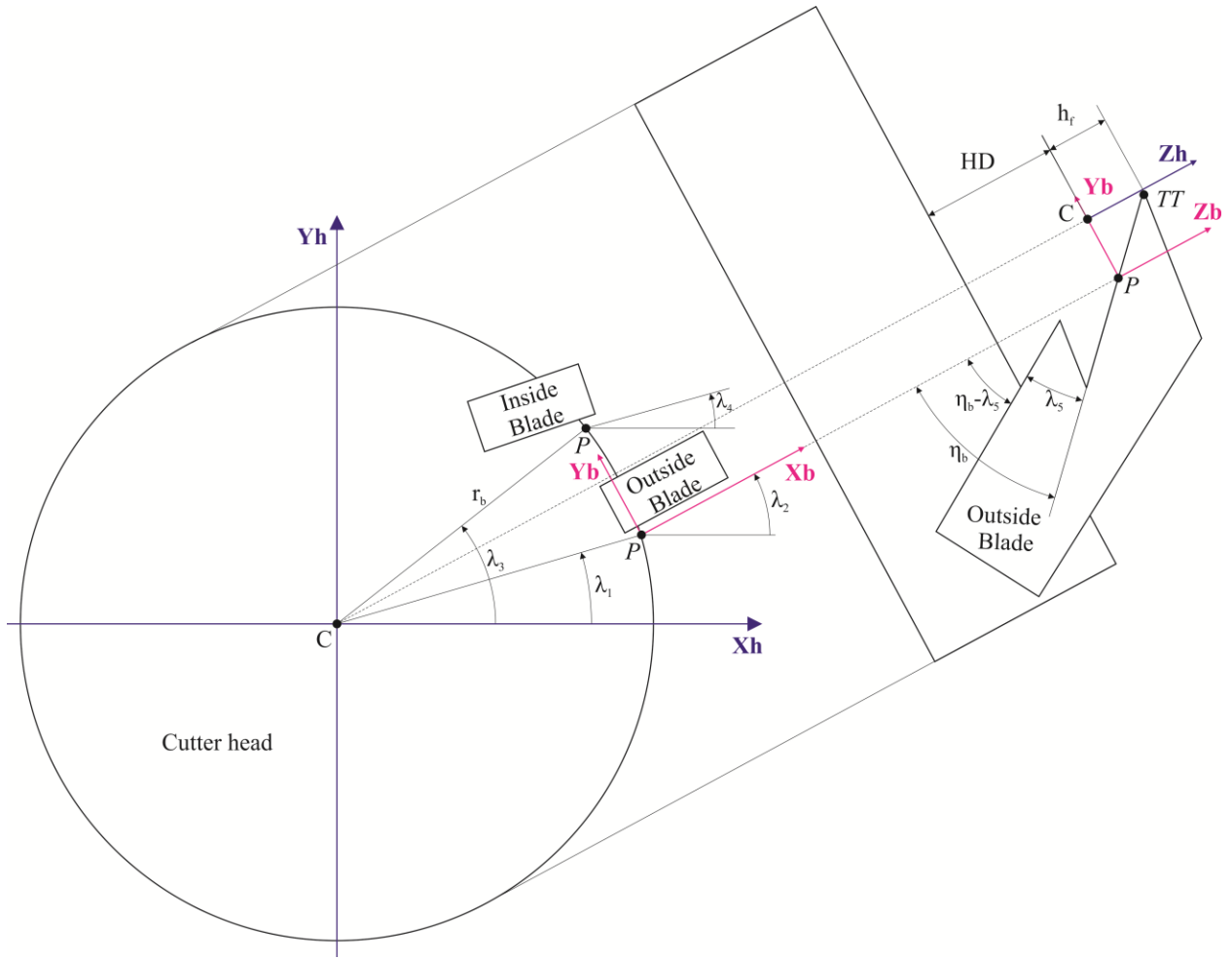


Fig. 3-7 The schematic view of the cutter head and the blade orientation.

By proper coordinate transformations, the cutting edge representation in the cutter head coordinate system,  $Sh$ , is derived. This Transformation consists of one translation ( $Tr(X, Y, h_f)$ ) and one rotation ( $Rot(z, \lambda_2)$ ). From Fig. 3-8, the equations of  $X$  and  $Y$  can be derived as follows:

$$l = x_{tp} - y_{tp} \cdot \tan(\lambda_2), \quad (3-23)$$

$$X = r_b \cdot \cos(\lambda_1) - l \cdot \cos(\lambda_2), \quad (3-24)$$

$$Y = r_b \cdot \sin(\lambda_1) - l \cdot \sin(\lambda_2) - y_{tp} / \cos(\lambda_2). \quad (3-25)$$

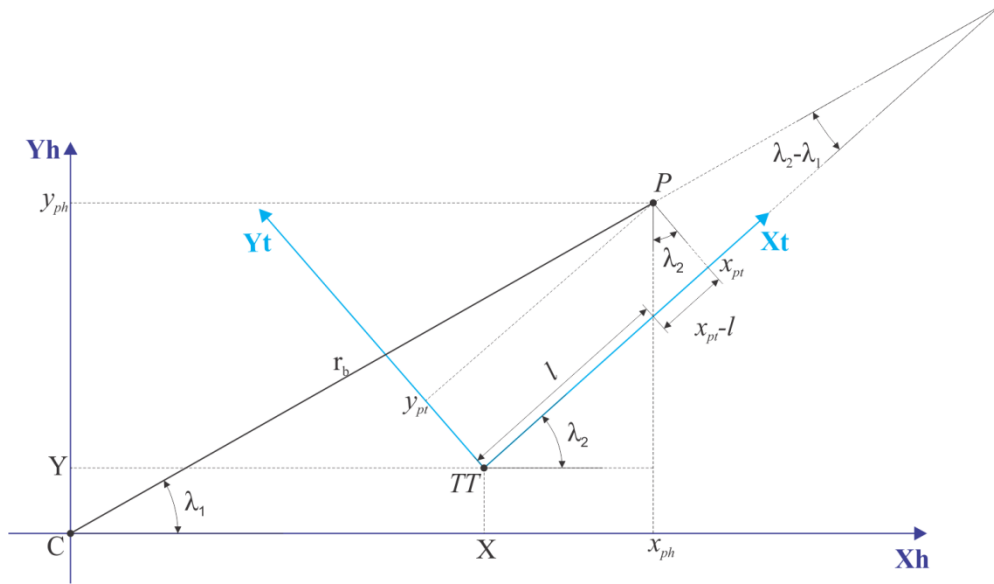


Fig. 3-8 The illustration of the transformation from  $St$  to  $Sh$ .

The transformation matrix from  $St$  to  $Sh$  is as

$$M_{ht} = Tr(X, Y, hf) Rot(Z, \lambda_2) = \begin{bmatrix} 1 & 0 & 0 & X \\ 0 & 1 & 0 & Y \\ 0 & 0 & 1 & hf \\ 0 & 0 & 0 & 1 \end{bmatrix} \begin{bmatrix} \cos(\lambda_2) & -\sin(\lambda_2) & 0 & 0 \\ \sin(\lambda_2) & \cos(\lambda_2) & 0 & 0 \\ 0 & 0 & 1 & 0 \\ 0 & 0 & 0 & 1 \end{bmatrix}. \quad (3-26)$$

Therefore, the cutting edge representation in  $Sh$  is as

$$r_h(s) = M_{ht} r_t(s), \quad (3-27)$$

where  $r$  is a vector pointed to the cutting edge from the coordinate system origin.

### 3.3 Kinematic structure of Formate™ (non-generated) face-hobbing and workpiece setup

In Formate™ process, the cradle does not have any rotation. The cutting system and the workpiece rotate proportionally and the cutter head has a feed movement along its axis, so two rotations and one translation. The machine tool structure is illustrated in Fig. 3-9.

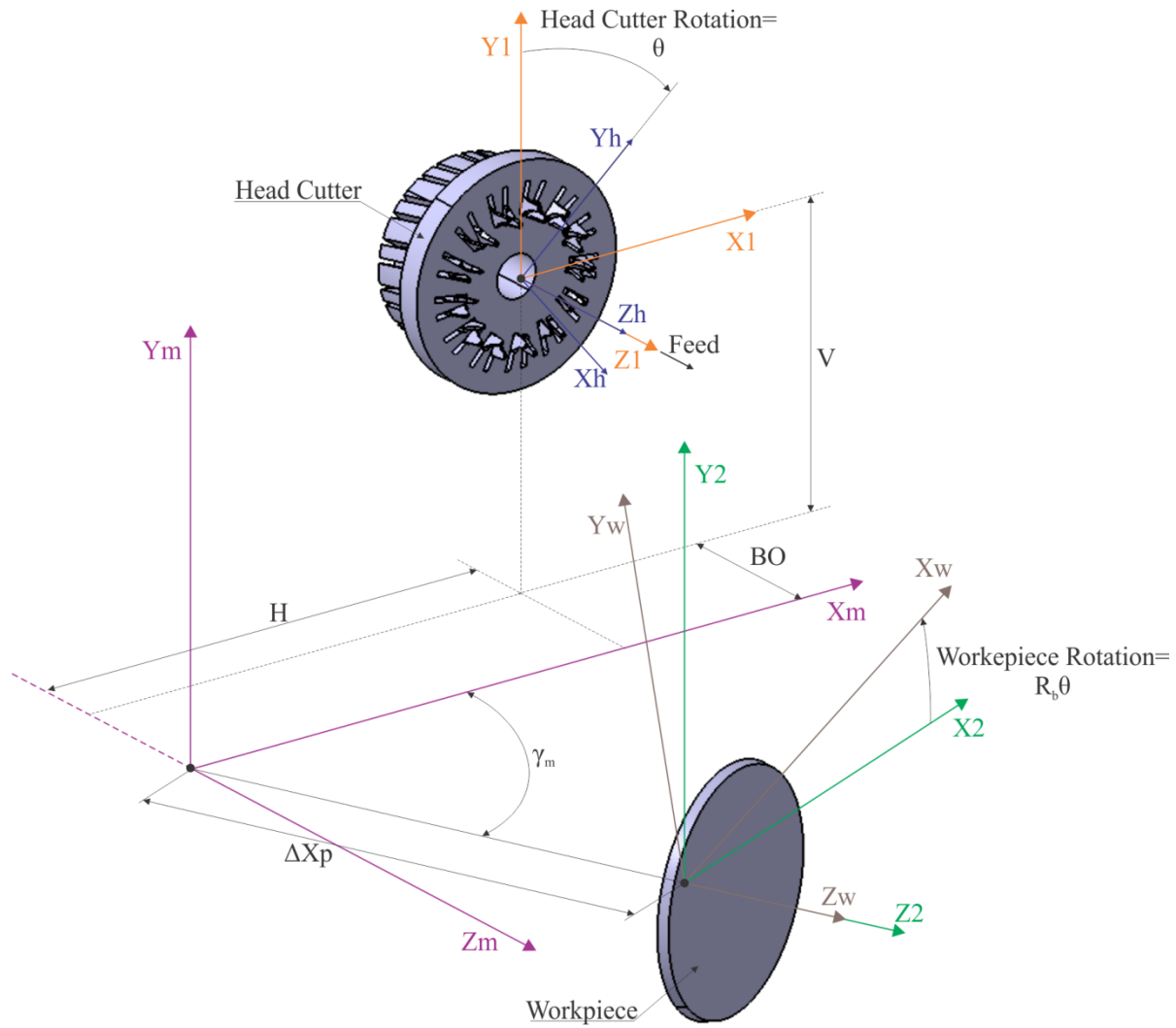


Fig. 3-9 Formate™ machine tool structure and the workpiece setup.

Coordinate system  $Sh$  is rigidly connected to the cutter head and rotates with it. The cutter head rotation,  $\theta$ , is measured in coordinate system  $SI$ .  $ZI$  ( $z$  axis of  $SI$ ) is common with  $Zh$  and plane  $XYI$  ( $xy$  plane of  $SI$ ) is coincident with  $XYh$ . At the beginning of the machining process, the cutter head has an offset ( $BO$ ) to the back of the machine plane ( $XYm$ ) and during machining; the cutter head is fed toward the machine plane ( $XYm$ ) by an axial translational movement (Feed in Fig. 3-7).  $ZI$  is perpendicular to the plane  $XYm$ . The workpiece coordinate system ( $Sw$ ) is rigidly attached to the workpiece and rotates with the workpiece. The machine settings are adjusted in  $Sm$  (machine coordinate system). For Formate™ process, four machining settings are required (Fig. 3-9), horizontal setting,  $H$ , vertical setting,  $V$ , machine root angle,  $\lambda_m$  and machine center to

back,  $\Delta X_p$ . In addition, the workpiece rotates proportionally with the cutter head by a ratio as  $R_b = N_b/N_g$ , where  $N_g$  is the number of gear teeth. The workpiece rotation is measured in coordinate system  $S_2$ .  $Z_2$  is common with  $Z_w$  and  $XY_2$  is coincident with  $XY_m$ . Because the workpiece and the cutter head have a relative motion with respect to each other, in order to know the effect of the blades when they remove material from workpiece, the representation of the blade cutting edge should be derived in the workpiece coordinate system ( $S_w$ ). For this purpose a set of coordinate transformations are required to transform the cutting edge from  $Sh$  to  $S_w$  as follows:

$$M_{1h} = \begin{bmatrix} \cos(-\theta) & -\sin(-\theta) & 0 & 0 \\ \sin(-\theta) & \cos(-\theta) & 0 & 0 \\ 0 & 0 & 1 & 0 \\ 0 & 0 & 0 & 1 \end{bmatrix}, \quad (3-28)$$

$$M_{m1} = \begin{bmatrix} 1 & 0 & 0 & H \\ 0 & 1 & 0 & V \\ 0 & 0 & 1 & -BO \\ 0 & 0 & 0 & 1 \end{bmatrix}, \quad (3-29)$$

$$M_{2m} = \begin{bmatrix} \cos(-(\pi/2 - \gamma_m)) & 0 & \sin(-(\pi/2 - \gamma_m)) & 0 \\ 0 & 1 & 0 & 0 \\ -\sin(-(\pi/2 - \gamma_m)) & 0 & \cos(-(\pi/2 - \gamma_m)) & -\Delta X_p \\ 0 & 0 & 0 & 1 \end{bmatrix}, \quad (3-30)$$

$$M_{w2} = \begin{bmatrix} \cos(-R_b\theta) & -\sin(-R_b\theta) & 0 & 0 \\ \sin(-R_b\theta) & \cos(-R_b\theta) & 0 & 0 \\ 0 & 0 & 1 & 0 \\ 0 & 0 & 0 & 1 \end{bmatrix}, \quad (3-31)$$

where  $M_{1h}$ ,  $M_{m1}$ ,  $M_{2m}$  and  $M_{w2}$  are transformations from  $Sh$  to  $S_1$ ,  $S_1$  to  $S_m$ ,  $S_m$  to  $S_2$  and from  $S_2$  to  $S_w$ , respectively. As it can be seen, the only variables in these matrixes are  $\theta$  and  $BO$ .

Using these transformations, the cutting edge equation in the workpiece coordinate system,  $r_w$ , can be obtained as

$$M_{WH} = M_{w2} M_{2m} M_{m1} M_{1h}, \quad (3-32)$$

$$r_w(s, \theta, BO) = M_{WH} r_h(s). \quad (3-33)$$

$BO$  and  $\theta$  are in terms of time,  $t$ , and  $s$  is an independent variable, therefore  $r_w = r_w(s, t)$  which means that Eq. (3-33) represents an equation of a surface in terms of two variables,  $s$  and  $t$ . For Formate™ process this equation directly gives a surface.  $BO$  decreases during machining process with a specified acceleration till it reaches zero. When  $BO$  is zero, gear tooth surfaces are finished when the machining settings are adjusted properly with no offset to back. At this position, the cutter head is held fixed (no axial feed) and rotates  $N_g$  times, to let the cutting system to finish cutting the desired gear tooth surfaces on the workpiece. At this position when  $BO$  is zero, five cutting surfaces resulting of five rotations of the cutter head for one outside blade are shown in Fig. 3-10.

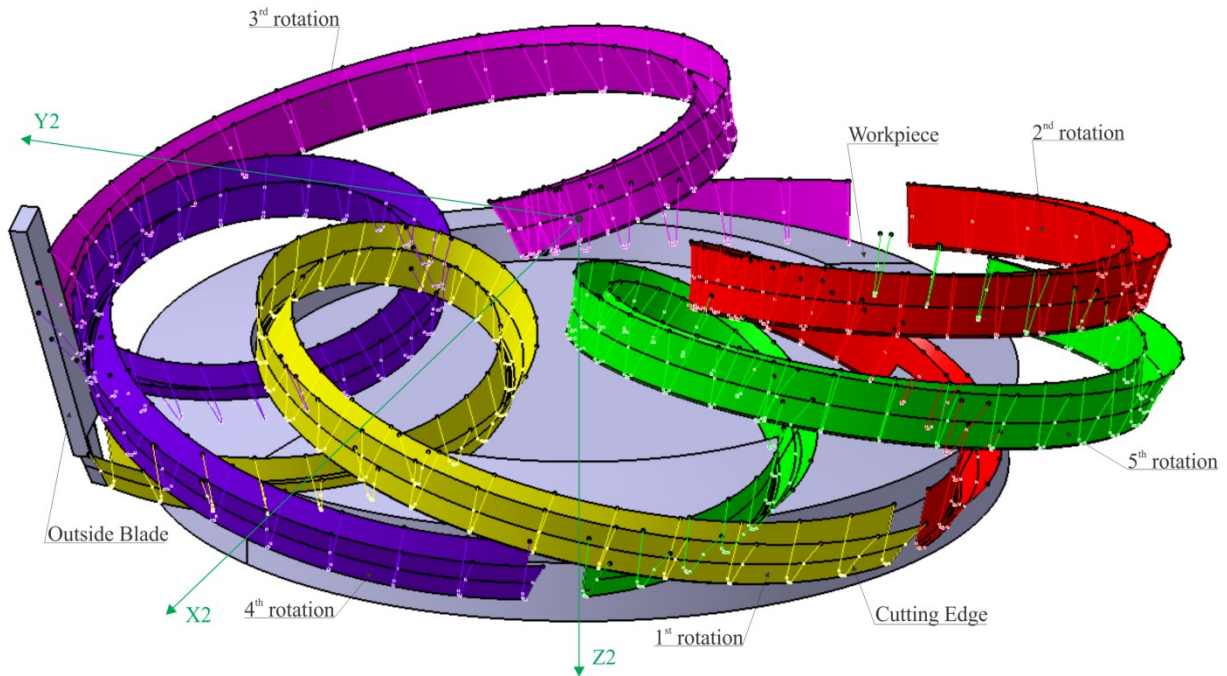


Fig. 3-10 Five cutting surfaces of the outside blade.

Using Eq. (3-33), the first rotation in Fig. 3-10 can be illustrated as Fig. 3-11.

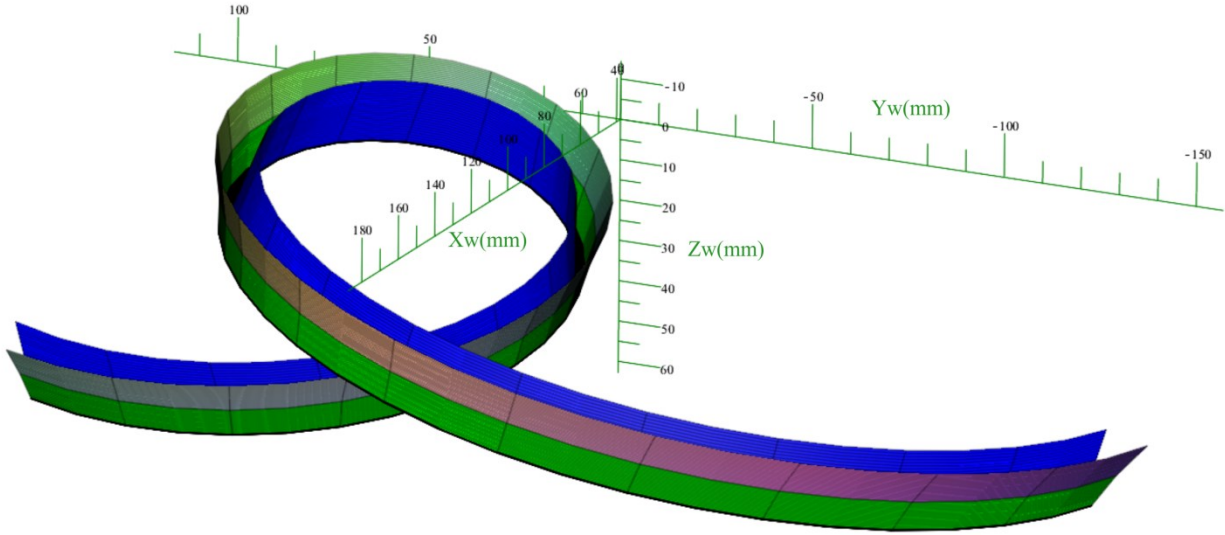


Fig. 3-11 The cutting surface of the first rotation.

Parameters of the cutting system and the machine settings used to create Fig. 3-10 and Fig. 3-11 are listed in Table 3-2.

Table 3-2 The cutter head and outer blade parameters and the machine settings

|                                      | Parameters   | value      |
|--------------------------------------|--------------|------------|
| The cutter head and blade parameters | $h_f$        | 12 mm      |
|                                      | $r_e$        | 1 mm       |
|                                      | $L_T$        | 10 mm      |
|                                      | $\tau$       | 6 deg      |
|                                      | $\rho$       | 762 mm     |
|                                      | $\alpha_e$   | 20 deg     |
|                                      | $\alpha_c$   | 5 deg      |
|                                      | $k_e$        | 12 deg     |
|                                      | $\eta_b$     | 4.420 deg  |
|                                      | $r_b$        | 76 deg     |
|                                      | $\lambda_1$  | 10 deg     |
|                                      | $\lambda_2$  | 10 deg     |
| The machine settings                 | H            | 63.521 mm  |
|                                      | V            | 101.295 mm |
|                                      | $\gamma_m$   | 67.111 deg |
|                                      | $\Delta X_p$ | 1.070 mm   |
|                                      | $R_b$        | 13/45      |

### 3.4 Workpiece discretization

The geometry of the workpiece in face-milling can be represented by parameters which some of them are the bevel gear geometrical parameters (pitch angle,  $\Gamma$ , outer cone distance,  $C$ , face width,  $F$ , addendum,  $A$ , and dedendum,  $D$ ). Other parameters are workpiece dimensions that can be obtained from the gear geometrical parameters as follows  $H_1 = F \cdot \cos(\Gamma)$ ,  $H_2 = (A+D) \cdot \sin(\Gamma)$ ,  $H_3 = (A+D) \cdot \sin(\Gamma) + F \cdot \cos(\Gamma)$ ,  $H_4 = D \cdot \sin(\Gamma) + C \cdot \cos(\Gamma)$  and  $L = C \cdot \sin(\Gamma) - D \cdot \cos(\Gamma)$ . Fig. 3-11 shows the axisymmetric section of the workpiece with the parameters.

In order to derive the chip geometry, the intersection between the workpiece and the blades is needed to be derived. For this purpose, the workpiece is discretized into disks with  $\Delta Z$  height along its symmetry axis, see Fig. 3-12, and then the intersection is calculated between these disks and the blades.

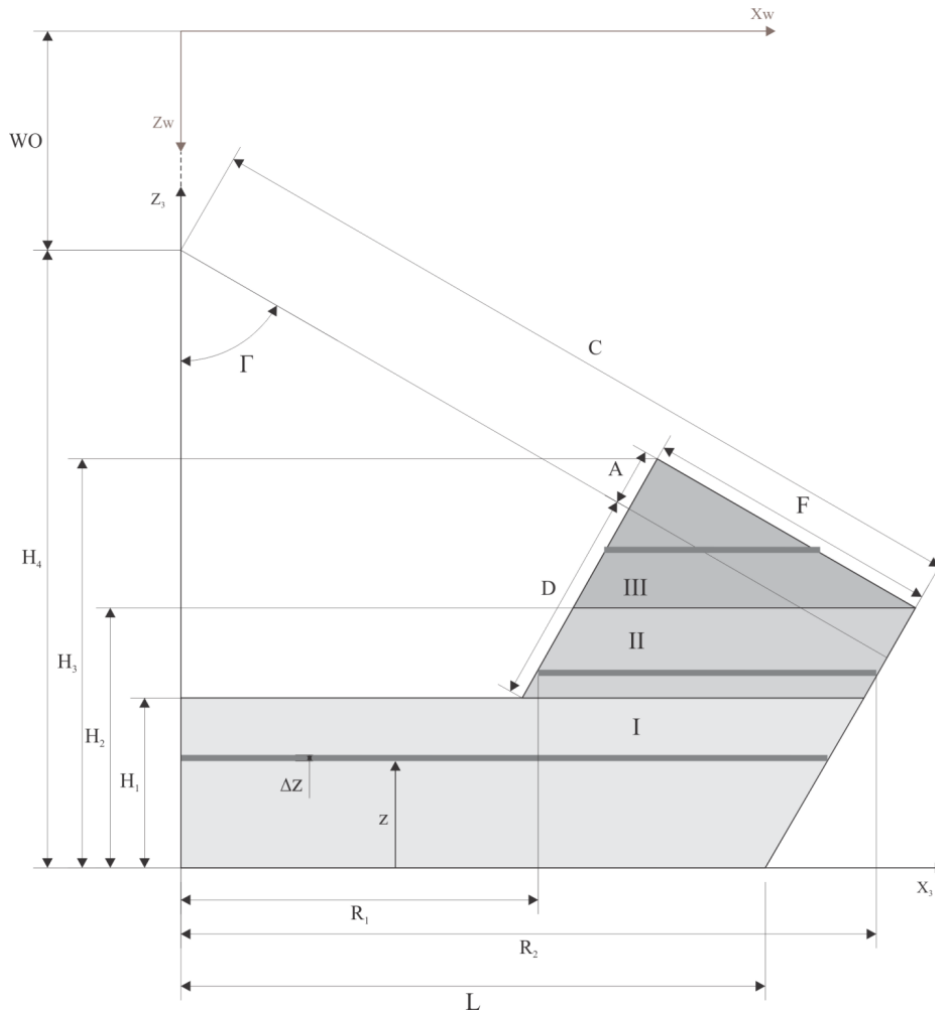


Fig. 3-12 Discretization of the workpiece along  $Z_3$  by  $\Delta z$ .



The workpiece in Fig. 3-11 has three sections, I, II and III, which in each the disks have different mathematical representations as follows:

$$I: \begin{cases} R_1 = 0 \\ R_2 = C \cdot \sin(\Gamma) - D \cdot \cos(\Gamma) + z / \tan(\Gamma) \end{cases}, 0 \leq z \leq H_1, \quad (3-34)$$

$$II: \begin{cases} R_1 = C \cdot \sin(\Gamma) - D \cdot \cos(\Gamma) - \frac{F}{\sin(\Gamma)} + \frac{z}{\tan(\Gamma)}, H_1 \leq z \leq H_2, \\ R_2 = C \cdot \sin(\Gamma) - D \cdot \cos(\Gamma) + z / \tan(\Gamma) \end{cases} \quad (3-35)$$

$$III: \begin{cases} R_1 = C \cdot \sin(\Gamma) - D \cdot \cos(\Gamma) - \frac{F}{\sin(\Gamma)} + \frac{z}{\tan(\Gamma)} \\ R_2 = C \cdot \sin(\Gamma) - D \cdot \cos(\Gamma) + \frac{H_2}{\tan(\Gamma)} - \frac{z - H_2}{\tan\left(\frac{\pi}{2} - \Gamma\right)}, H_2 \leq z \leq H_3. \end{cases} \quad (3-36)$$

In order to transform coordinates of the disks from S3 to Sw, the following translation is used

$$D_w = \text{Trans}(0, 0, -z + H_4 + WO) \cdot D_3, \quad (3-37)$$

where  $D_w$  and  $D_3$  are disk coordinates in Sw and S3, respectively.

### 3.5 Conclusion

In this chapter, the machine tool kinematics and cutting system geometry are defined mathematically with closed form equations. These representations will be used in following chapters to re-design the cutting blade, obtain the un-deformed chip geometry, predict the cutting forces and finally find the optimum machining parameters.

## Chapter 4

# Tool Wear Characterization and Improvement

**Citation:** Habibi, M., Chen, Z.C., 2015, “A New Approach to Blade Design with Constant Rake and Relief Angles for Face-hobbing of Bevel Gears”, *ASME Journal of Manufacturing Science and Engineering*, 138(3):031005-031005-16, doi: 10.1115/1.4030936.

### 4.1 Introduction

Many research works have been conducted on material and coating of cutting tools to improve tool wear characteristic ([46], [47], [48], [49] and [50]). However, the geometry of the cutting tools and machining processes also play important roles in the tool wear phenomena. In bevel gear manufacturing processes, multi-flank chip formation occurs at corners of the blades of the cutting system which causes the tool wear at the corners ([12] and [14]). This local wear decreases the tool life and causes unexpected shut down in the production line.

A few researches have been carried out on the tool wear in bevel gear manufacturing. Klocke et al. ([13] and [14]) and Brecher et al. ([9], [10] and [11]) did important works in this field. They showed that large variations of the working rake and relief angles especially at the corner cause the local tool wear. In addition, they proposed a method to predict the tool wear. Moreover, an equation was introduced which is able to formulate the effecting characteristics in the tool wear. They suggested a method to decrease the tool wear by changing the shape of the gear tooth (consequently the shape of the cutting edge of the blades). In this way, the gear designer needs to

compromise between the gear design and the tool wear which means applying limitations on the design process. Even after changing the gear design for the sake of having less tool wear, geometrical related effects on the tool wear still remain. In the present paper, a new method to design the cutting blades is introduced by which the cutting edge is kept unchanged. In the proposed method, the working rake and relief angles are kept constant by considering the varying cutting velocity along the cutting edge and the machine tool kinematics. A proposed blade model is designed using the new method. In order to prove that the proposed blade has constant working rake and relief angles, the measurements of the angles are carried out on the proposed blade and compared with the conventional one. In addition, in order to show better tool wear characteristics of the proposed blade, finite element (FE) machining simulations are carried out on the both proposed and conventional blades.

In industry, it is necessary to design the cutting tools based on the working rake and relief angles. In addition, these angles play crucial roles in the tool wear which it will be discussed in section 5. These angles obtained at each point on the cutting edge considering the cutting velocity at that point. Therefore, in face-hobbing process, the first step to find the working angles is to calculate the cutting velocity.

#### **4.2 Working rake and relief angles**

In order to define the actual velocity at each point on the cutting edge during machining, each point on the cutting edge is traced on the cutting surface. This is a curve (the red curve in Fig. 4-1) and can be calculated by substituting the corresponding value of  $s$  (the blade profile parameter) of each point into the equations of the cutting surface.

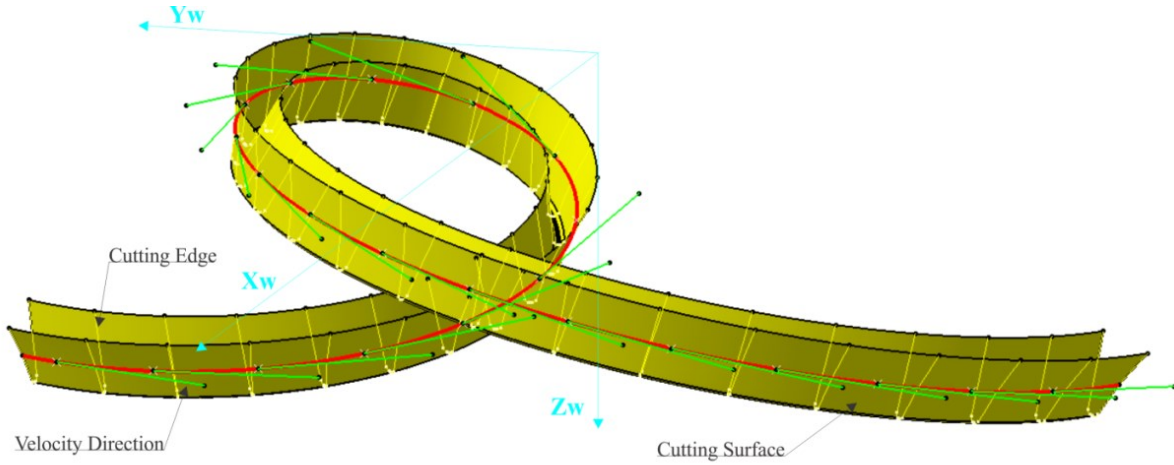


Fig. 4-1 Velocity direction.

The cutting velocity,  $V$ , at each point on the cutting surface can be derived as

$$V = \frac{\partial r_w(s, \theta)}{\partial \theta} \cdot \frac{d\theta}{dt} \quad (4-1)$$

The equation of  $V$  is calculated in the coordinate system  $S_w$ . In order to transform this vector to  $S_e$ , the following transformations are used:

$$M_{wh} = M_{w2} M_{2m} M_{m1} M_{1h} \quad (4-2)$$

$$M_{ew} = M_{et} (M_{ht})^{-1} (M_{wh})^{-1} \quad (4-3)$$

Then, the formula of  $V$  in  $S_e$  can be obtained as

$$V_e = M_{ew} V \quad (4-4)$$

The working relief and rake angles are defined on a plane perpendicular to the cutting edge. This plane,  $p$ , is determined by a vector tangent to the cutting edge,  $T_l$ , and a point,  $P_e$ , on the cutting edge (Fig. 4-2).

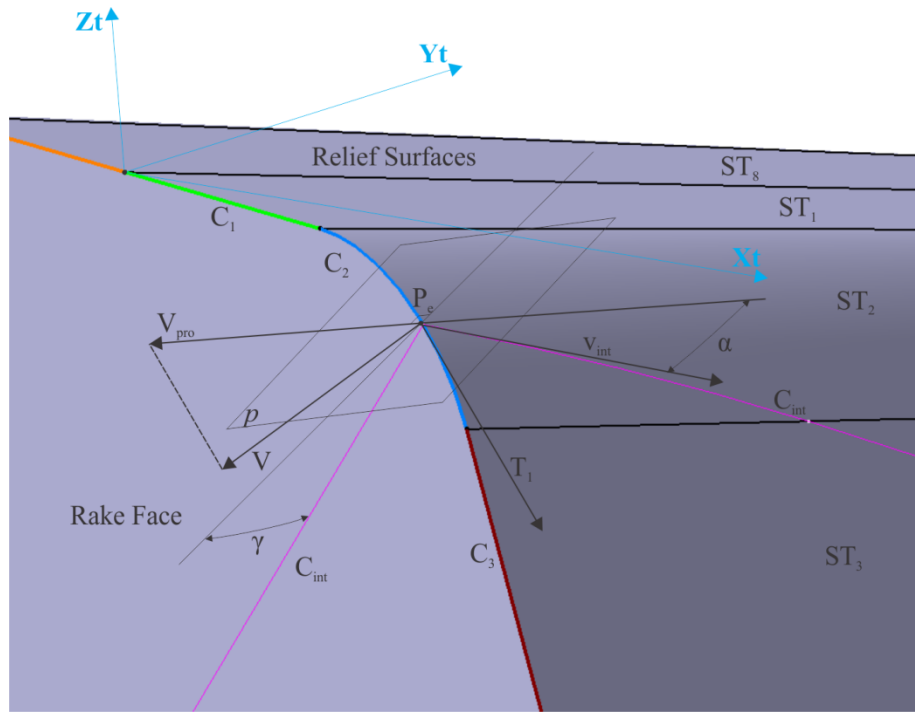


Fig. 4-2 Derivation of the working rake ( $\gamma$ ) and relief ( $\alpha$ ) angles.

The normal vector of the plane,  $p$ , can be derived as

$$T_1 = \frac{dC_i}{ds} = \begin{bmatrix} T_{1x} \\ T_{1y} \\ T_{1z} \end{bmatrix}. \quad (4-5)$$

Then, the equation of  $p$  can be written as

$$p: T_{1x} \cdot (x - x_{p_e}) + T_{1y} \cdot (y - y_{p_e}) + T_{1z} \cdot (z - z_{p_e}) = 0. \quad (4-6)$$

The projection of the cutting velocity,  $V$ , on  $p$  is  $V_{pro}$ . The intersection between  $p$  and the rake face and the relief faces are curves,  $C_{int}$ , in Fig. 4-2 (the pink curve).  $C_{int}$  on the rake face is always a straight line but on relief faces can be a curve. In order to derive  $C_{int}$  on the relief

surfaces,  $x$ ,  $y$  and  $z$  components of  $ST_i$  are substituted into  $p$  (Eq. (4-6)) and then by solving in terms of  $t$ , the equation of  $t$  is derived as

$$t = -\frac{T_1 \cdot (C_{ei}(s) - P_e)}{T_1 \cdot V_l(s)}. \quad (4-7)$$

It can be seen that  $t$  is in terms of  $s$ . By substituting  $t(s)$  from Eq. (4-7) to Eq. (4-6), the equation of  $C_{int}$  on relief faces can be derived.  $V_{int}$  is a vector tangent to  $C_{int}$  at point  $P_e$ . The angle between  $V_{int}$  and  $V_{pro}$  is the working relief angle ( $\alpha$ ) and the angle between  $C_{int}$  on the rake plane and a direction perpendicular to  $V_{pro}$  is the working rake angle ( $\gamma$ ).

The theoretical relief and rake angles are derived when only the cutter head rotates. In this case, the workpiece is fixed, there is no axial feed and the cutting velocity direction,  $V_{th}$ , is always perpendicular to a vector ( $L$ ) lying on a plane parallel to  $XhYh$ , from  $Zh$  axis to the point  $P_h$  (Fig. 4-3).

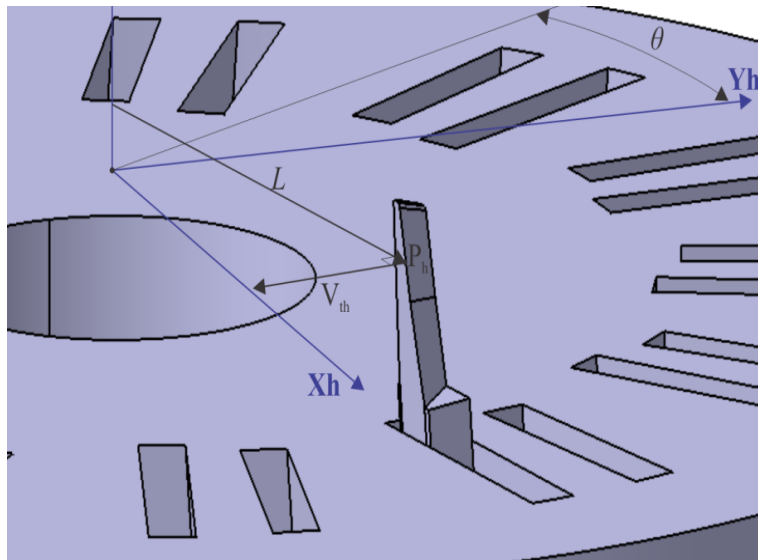


Fig. 4-3 The theoretical cutting velocity,  $V_{th}$ .

These theoretical angles are useful to see the influence of the relative motion between the workpiece and the cutting systems in values of the rake and relief angles. The equations of  $V_{th}$  in  $Sh$  can be written as

$$V_{th}^h = \begin{bmatrix} \cos\left(-\frac{\pi}{2}\right) & -\sin\left(-\frac{\pi}{2}\right) & 0 & 0 \\ \sin\left(-\frac{\pi}{2}\right) & \cos\left(-\frac{\pi}{2}\right) & 0 & 0 \\ 0 & 0 & 1 & 0 \\ 0 & 0 & 0 & 1 \end{bmatrix} \begin{bmatrix} P_h^x \\ P_h^y \\ P_h^z \\ 1 \end{bmatrix}. \quad (4-8)$$

The equation of  $V_{th}$  in  $Se$  is given by

$$V_{th}^e = M_{ew} M_{wh} \left( V_{th}^h - [0 \ 0 \ 0 \ 1]^T \right). \quad (4-9)$$

The theoretical rake and relief angles are calculated using  $V_{th}$  instead of  $V$  in Fig. 4-3.

### 4.3 Tool wear characterization in gear cutting

Brecher et al. ([9], [10] and [11]), Klocke et al. ([13] and [14]) and Klein [12] did important researches on the tool wear characterization in bevel gear cutting. They state that the tool wear increases locally by increasing gradients of un-deformed chip thickness ( $h_{cu}$ ) and the working rake and relief angles ( $\alpha$  and  $\gamma$ ) along the cutting edge ( $l_s$ ). The working rake and relief angles influence the tool load and the thermal stress on the cutting edge, respectively [14]. Ref. [14] suggests an equation to formulate the effects of  $h_{cu}$ ,  $\alpha$  and  $\gamma$  on the tool wear as

$$K_G = l_e \cdot \frac{\Delta h_{cu}}{\Delta l_s} \cdot \frac{\Delta \alpha}{\Delta l_s} \cdot \frac{\Delta \gamma}{\Delta l_s}, \quad (4-10)$$

where  $l_e$  is working length which is the contact length between blade and the workpiece during machining. A high  $K_G$  represents a higher tool wear at a specific point on the cutting edge.

Only a portion of the cutting surface in one revolution of the cutter head is in contact with the workpiece as it can be seen in Fig. 3-10. Therefore, the working rake and relief angles along the cutting edge are calculated during this portion ( $\theta \approx [30^\circ, 70^\circ]$ ). Theoretical and working relief ( $\alpha$ ) and rake ( $\gamma$ ) angles are shown in Fig. 4-4 and Fig. 4-5.

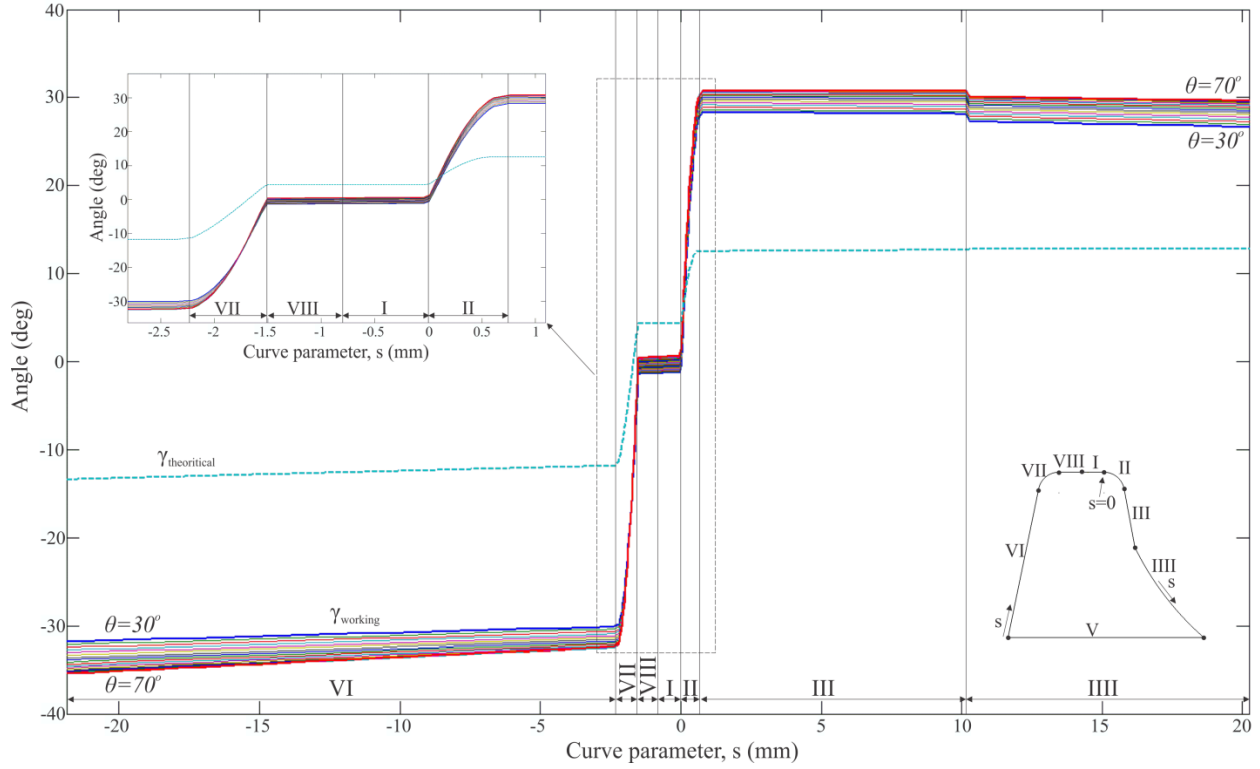


Fig. 4-4 The working and theoretical rake angles

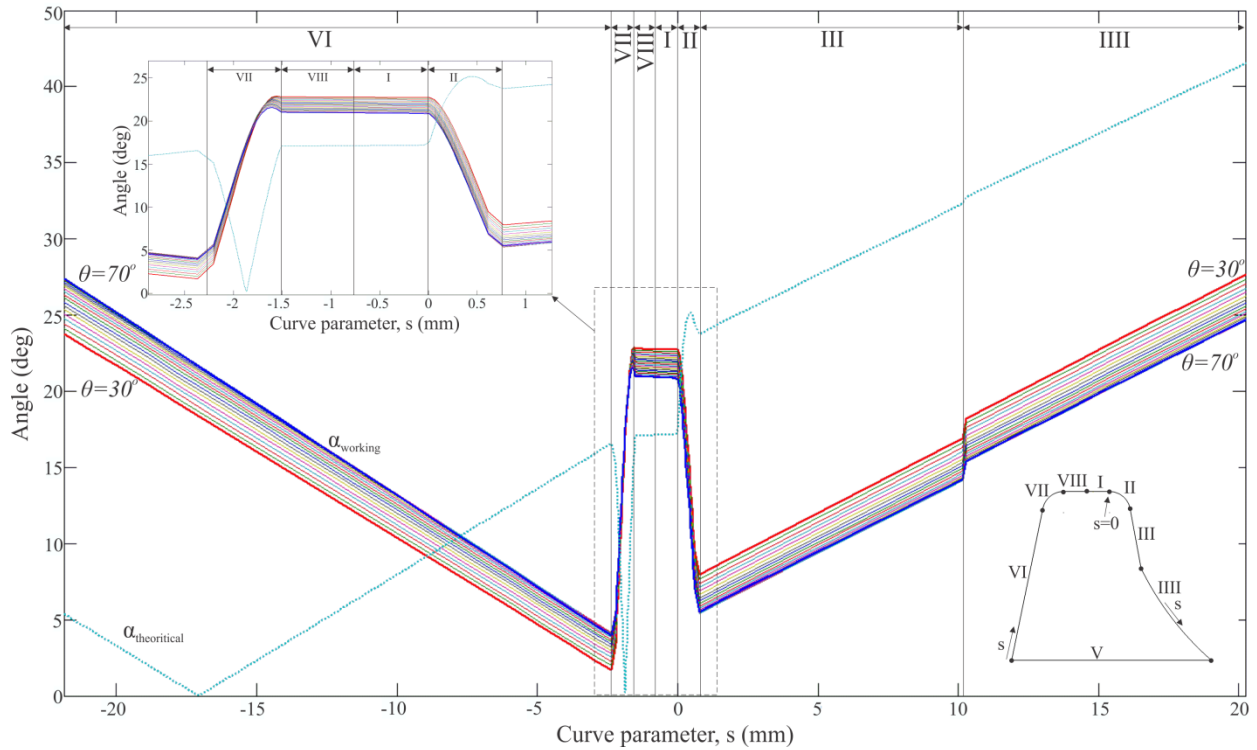


Fig. 4-5 The working and theoretical relief angles



As it can be seen in Fig. 4-4 and Fig. 4-5, sharp and large changes occur in the relief and rake angles in sections II and IV. These sharp changes are one of the main reasons of the tool wear at the corners of the blades based on Eq. (4-10) because  $K_G$  has higher value in comparison with other sections on the cutting edge.

#### 4.4 The proposed method to design the blades

The main idea of the proposed method is to decrease the gradients of the working rake and relief angles along the cutting edge as much as possible (theoretically to zero) by changing the geometry of the rake and relief surfaces of the blade. Using this new method, those sharp variations in Fig. 4-4 and Fig. 4-5 at the corners are prevented.

In order to have the blade model using the proposed method, the working rake and relief angles are assigned to the model directly. Fig. 4-6 shows the method.

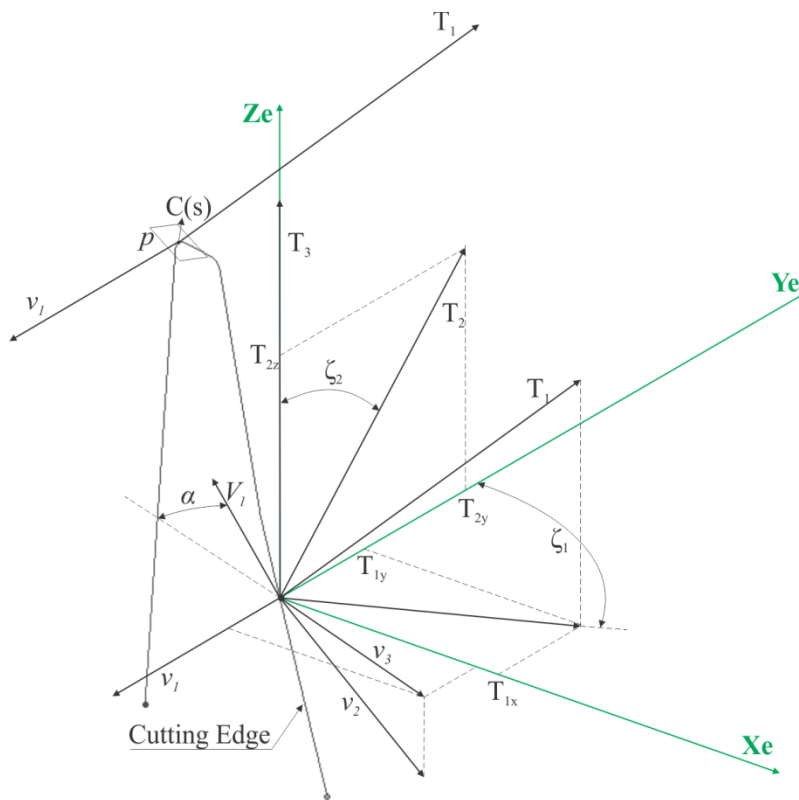


Fig. 4-6 The proposed method to design the rake and relief surfaces by assigning working rake ( $\gamma$ ) and relief ( $\alpha$ ) angles directly.

The purpose of the method is to define a vector ( $V_l$  in Fig. 3-5) with assigned working angle for the relief surfaces (for the rake surfaces the same method needs to be applied to derive  $V_l$  with a specified rake angle, in Fig. 4-6 the method for relief surfaces is shown, but for the rake surfaces the process is exactly the same).  $V_l$  is used as a tangent vector for the rake or relief surfaces at the specific point on the cutting edge where the cutting velocity ( $v_l$ ) is calculated. It is important to be noticed that  $V_l$  is equivalent to  $V_{int}$  in Fig. 4-2.  $V_l$  is on the plane perpendicular to the cutting edge and is created using the extension of the projection of the cutting velocity and a rotation by  $\alpha$ . Therefore, the followings describe how to derive the cutting velocity projection ( $v_3$ ) and finally creating  $V_l$  using a rotation by  $\alpha$ . For this purpose,  $T_1$  and  $v_l$  are moved to the origin of  $Se$ . Two rotations are applied to  $T_3$  to be coincident to  $Ze$  ( $T_3$  in Fig. 4-6) and then the same transformations need to be applied on  $v_l$  (result is  $v_2$  in Fig. 4-6).

The tangent vector on the cutting edge at the point  $P$  is  $T_l$  (Eq. (4-5)). The angle of the first rotation,  $\xi_1$ , is defined as

$$\xi_1 = \tan^{-1} \left( \frac{T_{1x}}{T_{1y}} \right). \quad (4-11)$$

Then,  $T_2$  can be calculated using a rotation about  $Ze$  as

$$T_2 = \begin{bmatrix} \cos(\xi_1) & -\sin(\xi_1) & 0 & 0 \\ \sin(\xi_1) & \cos(\xi_1) & 0 & 0 \\ 0 & 0 & 1 & 0 \\ 0 & 0 & 0 & 1 \end{bmatrix} T_1. \quad (4-12)$$

The angle for the second rotation,  $\xi_2$ , can be written as

$$\xi_2 = \tan^{-1} \left( \frac{T_{2y}}{T_{2z}} \right). \quad (4-13)$$

Then,  $T_3$  is derived by a rotation about  $Xe$  as follows:

$$T_3 = \begin{bmatrix} \cos(\xi_2) & 0 & \sin(\xi_2) & 0 \\ 0 & 1 & 0 & 0 \\ -\sin(\xi_2) & 0 & \cos(\xi_2) & 0 \\ 0 & 0 & 0 & 1 \end{bmatrix} T_2. \quad (4-14)$$

The transformation matrix from  $T_1$  to  $T_3$  is given by

$$M_{T_1-T_3} = \begin{bmatrix} \cos(\xi_2) \cdot \cos(\xi_1) & -\cos(\xi_2) \cdot \sin(\xi_1) & \sin(\xi_2) & 0 \\ \sin(\xi_1) & \cos(\xi_1) & 0 & 0 \\ -\sin(\xi_2) \cdot \cos(\xi_1) & \sin(\xi_2) \cdot \sin(\xi_1) & \cos(\xi_2) & 0 \\ 0 & 0 & 0 & 1 \end{bmatrix}. \quad (4-15)$$

By applying this matrix, the cutting velocity projection,  $v_3$ , is derived as

$$v_3 = \begin{bmatrix} 1 & 0 & 0 & 0 \\ 0 & 1 & 0 & 0 \\ 0 & 0 & 0 & 0 \\ 0 & 0 & 0 & 1 \end{bmatrix} M_{T_1-T_3} v_1. \quad (4-16)$$

Finally, the equation of  $V_l$  can be obtained as

$$V_l = \begin{bmatrix} \cos(-\alpha) & 0 & -\sin(-\alpha) & 0 \\ 0 & 1 & 0 & 0 \\ \sin(-\alpha) & 0 & \cos(-\alpha) & 0 \\ 0 & 0 & 0 & 1 \end{bmatrix} (-v_3). \quad (4-17)$$

The obtained  $V_l$  is transformed back to the point on the cutting edge by  $M_{T_3-T_1} = (M_{T_1-T_3})^{-1}$ .

It should be noted that the derived  $V_l$  in Eq. (4-17), for rake and relief surfaces, is equivalent to  $C_{int}$ , on rake and  $V_{int}$  on relief surfaces in Fig. 4-6. Therefore, working rake and relief angles are defined by  $V_l$ . Since, in the proposed method,  $V_l$  is assigned to all points on the cutting edge using Eqs. 44 to 50 and the rake and relief surfaces connecting to the cutting edge are modeled by  $V_l$ , hence, mathematically, normal rake and relief angles are kept constant with desired values.

If the cutting velocity,  $v_l$ , is assumed to be constant in the process (unlike the face-hobbing), the equation of  $v_3$  can be simplified as

$$v_3 = \begin{bmatrix} -\frac{T_{1y}}{\sqrt{T_{1x}^2 + T_{1y}^2 + T_{1z}^2} \cdot \sqrt{T_{1x}^2 + T_{1y}^2}} \cdot T_{1x} \\ 1 \\ -\frac{1}{\sqrt{T_{1x}^2 + T_{1y}^2}} \cdot T_{1x} \\ 0 \\ 1 \end{bmatrix}. \quad (4-18)$$

where  $v_l$  is assumed to be parallel to  $Y_e$  and the equation of  $V_l$  can be rewritten as

$$V_l = \begin{bmatrix} \frac{\cos(\alpha) \cdot T_{1z} \cdot T_{1y}}{\sqrt{T_{1x}^2 + T_{1y}^2 + T_{1z}^2} \cdot \sqrt{T_{1x}^2 + T_{1y}^2}} + \frac{\sin(\alpha) \cdot T_{1x}}{\sqrt{T_{1x}^2 + T_{1y}^2}} \\ -\frac{\sin(\alpha) \cdot T_{1z} \cdot T_{1y}}{\sqrt{T_{1x}^2 + T_{1y}^2 + T_{1z}^2} \cdot \sqrt{T_{1x}^2 + T_{1y}^2}} + \frac{\cos(\alpha) \cdot T_{1x}}{\sqrt{T_{1x}^2 + T_{1y}^2}} \\ 0 \\ 1 \end{bmatrix}. \quad (4-19)$$

Based on the discussion in section 5, if the gradients of the working rake and relief angles decrease, the tool wear characteristics are improved (less  $K_G$ ). In the proposed method, it is tried to make the gradients equal to zero by setting constant values to the working relief and relief angles along the cutting edge. It should be noted that the cutting edge kept unchanged in the proposed method. In this paper for the modeled blade, the working rake and relief angle are set to 5.01 and 31.2 degrees, respectively. Fig. 4-7 (Right) shows the modeled rake (green surface) and relief (purple surface) surfaces around the corner of the proposed blade. The generating red and yellow lines ( $V_l$ ) are derived using the cutting velocity at each point on the cutting edge ( $v_l$ ) and Eq. (4-19). Then the rake and relief surfaces are created in CATIA™.

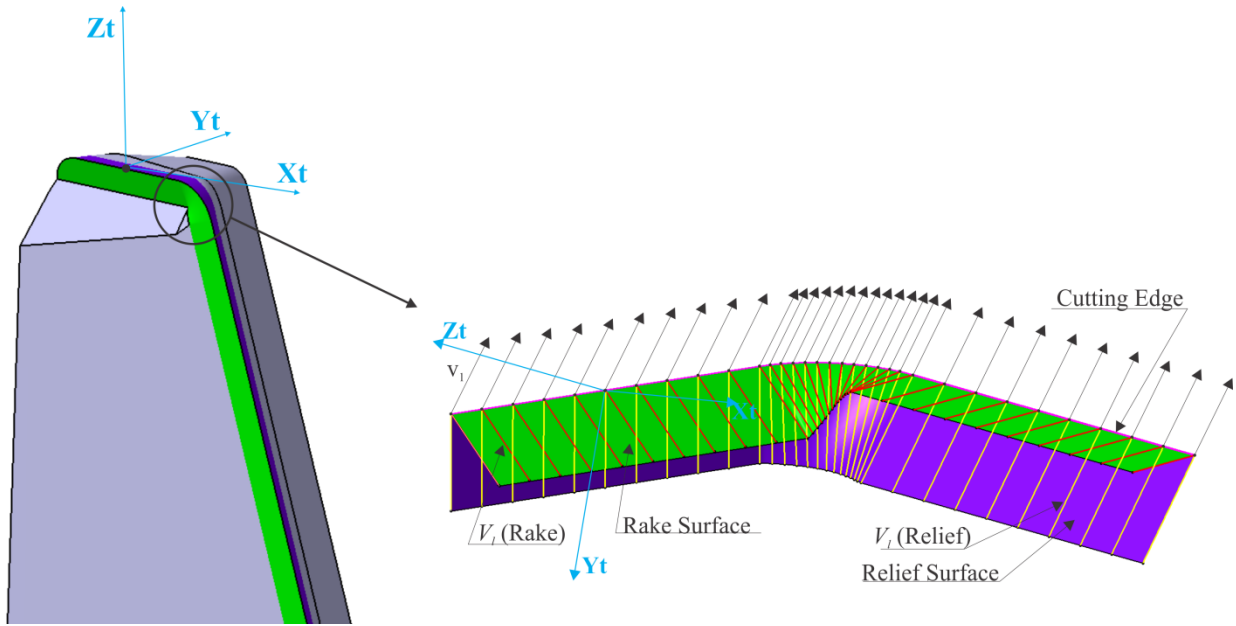


Fig. 4-7 The modeled blade using designed rake and relief surfaces, Left: The modeled rake and relief surfaces using generating line ( $V_t$ ).

In Fig. 4-7 (Left), using the designed rake and relief surfaces, a possible CAD model of the cutting blade is presented. It should be noted that except the designed rake and relief surfaces (green and purple surfaces), all other parts of the modeled blade is not unique and can be redesigned based on the manufacturing requirement. The designed blade in Fig. 4-7 (Right) can be manufactured and ground using 5-axis CNC grinding machine tools. The proposed method is applied on the main cutting edge for the case of half profile blade. In case of full profile blades, both sides of the cutting edge of the blade should be considered and redesigned because the both cutting edges engage with the workpiece. In addition, the relief surfaces are designed to follow the epicycloid and do not have any interference (gouging) with the cutting surface (the machined surface).

By setting the gradients equal to zero,  $K_G$  in Eq. (4-10) would be zero which is not logical because for sure the tool would be worn out even with  $K_G = 0$  in the real machining. Therefore, in case of the proposed blade model,  $\frac{\Delta\alpha}{\Delta l_s}$  and  $\frac{\Delta\gamma}{\Delta l_s}$  are replaced by two weighting coefficients in Eq. (4-10),  $w_\alpha$  and  $w_\gamma$ , respectively. Thus, Eq. (4-10) can be re-written as

$K_G = l_e \cdot w_\alpha \cdot w_\gamma \cdot w_h \cdot \frac{\Delta h_{cu}}{\Delta l_s}$ , where  $w_h$  is the weighting coefficient of the chip thickness variation along the cutting edge.

#### 4.5 Validation

In order to prove that the proposed rake and relief surfaces have constant working rake and relief angles along the cutting edge, the values of these angles are measured at 21 points (blue points in Fig. 4-8) around the corner of the proposed blade and compared with corresponding points on the conventional blade. The tool corner is selected because the working rake and relief angles have large variations at this location. Fig. 4-8.a and Fig. 4-8.b show the measured working and rake angles for one point in the middle of the corner of the conventional and proposed blade, respectively. The method of measuring the working rake and relief angles is discussed in section 4.

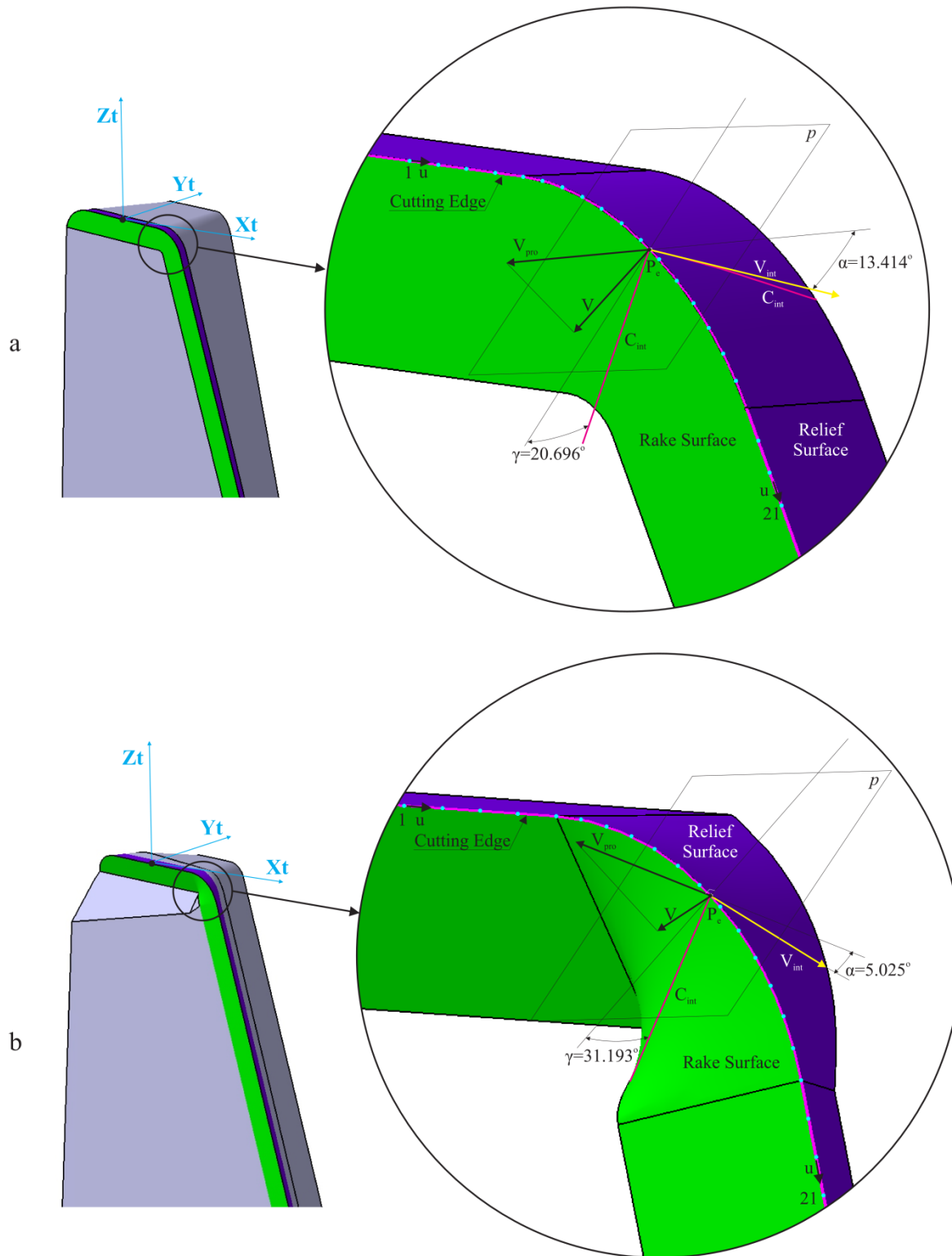


Fig. 4-8 Measuring the working rake ( $\gamma$ ) and relief ( $\alpha$ ) angles at the corner on (a) the conventional blade, (b) the proposed blade.

The measurements of the working rake and relief angles of the conventional blade and the proposed blade are summarized in Table 3. It is clear that variations in the working rake and relief angles along the cutting edge ( $\frac{\Delta\gamma}{\Delta u}$  and  $\frac{\Delta\alpha}{\Delta u}$ ) in the conventional blade are larger than the proposed blade. For instance, from point 5 to point 6 (entering area to the corner),  $\frac{\Delta\gamma}{\Delta u}$  and  $\frac{\Delta\alpha}{\Delta u}$  are 68.496 deg/mm and -10.037 deg/mm, respectively, for the conventional blade. While for the proposed blade,  $\frac{\Delta\gamma}{\Delta u}$  and  $\frac{\Delta\alpha}{\Delta u}$  are 0.06 deg/mm and -0.2 deg/mm, respectively. It shows 1141.6 and 50.186 times reduction in  $\frac{\Delta\gamma}{\Delta u}$  and  $\frac{\Delta\alpha}{\Delta u}$ , respectively, for the proposed blade in comparison with the conventional blade. This comparison shows a considerable reduction in the working rake and relief variations which improve the tool wear characteristics by reducing  $K_G$  (Eq. (4-10)).



Table 4-1 Measured working rake ( $\gamma$ ) and relief ( $\alpha$ ) angles for the conventional and proposed blades.

| Point No. | Distance on the cutting edge ,u (mm) | Conventional blade                   |   |  |   | Proposed blade                       |   |  |   |
|-----------|--------------------------------------|--------------------------------------|---|--|---|--------------------------------------|---|--|---|
|           |                                      | Working rake angle, $\gamma$ , (deg) | $\frac{\Delta\gamma}{\Delta u}$ (deg/m m) | Working relief angle, $\alpha$ , (deg) | $\frac{\Delta\alpha}{\Delta u}$ (deg/m m) | Working rake angle, $\gamma$ , (deg) | $\frac{\Delta\gamma}{\Delta u}$ (deg/m m) | Working relief angle, $\alpha$ , (deg) | $\frac{\Delta\alpha}{\Delta u}$ (deg/m m) |
| 1         | 0                                    | -0.237                               |   | 21.712                                 |   | 31.209                               |   | 5.010                                  |   |
| 2         | 0.077                                | -0.237                               | 0.000                                     | 21.717                                 | 0.075                                     | 31.209                               | 0.000                                     | 5.010                                  | 0.000                                     |
| 3         | 0.155                                | -0.237                               | 0.000                                     | 21.723                                 | 0.075                                     | 31.209                               | 0.000                                     | 5.010                                  | 0.000                                     |
| 4         | 0.232                                | -0.237                               | 0.000                                     | 21.729                                 | 0.076                                     | 31.209                               | 0.000                                     | 5.010                                  | 0.000                                     |
| 5         | 0.310                                | -0.237                               | 0.000                                     | 21.735                                 | 0.081                                     | 31.209                               | 0.000                                     | 5.010                                  | 0.000                                     |
| 6         | 0.361                                | 3.297                                | 68.496                                    | 21.217                                 | -10.037                                   | 31.212                               | 0.060                                     | 5.000                                  | -0.200                                    |
| 7         | 0.413                                | 6.795                                | 67.650                                    | 20.405                                 | -15.723                                   | 31.162                               | -0.963                                    | 4.899                                  | -1.961                                    |
| 8         | 0.465                                | 10.198                               | 65.965                                    | 19.3655                                | -20.140                                   | 31.199                               | 0.703                                     | 4.950                                  | 1.002                                     |
| 9         | 0.517                                | 13.456                               | 63.126                                    | 18.161                                 | -23.349                                   | 31.240                               | 0.804                                     | 5.004                                  | 1.047                                     |
| 10        | 0.568                                | 16.517                               | 59.322                                    | 16.826                                 | -25.860                                   | 31.226                               | -0.275                                    | 5.021                                  | 0.322                                     |
| 11        | 0.620                                | 19.359                               | 54.961                                    | 15.415                                 | -27.298                                   | 31.17                                | -1.075                                    | 5.028                                  | 0.149                                     |
| 12        | 0.671                                | 21.926                               | 49.760                                    | 13.96                                  | -28.198                                   | 31.151                               | -0.380                                    | 5.017                                  | -0.217                                    |
| 13        | 0.723                                | 24.218                               | 44.422                                    | 12.477                                 | -28.733                                   | 31.209                               | 1.140                                     | 5.005                                  | -0.240                                    |
| 14        | 0.774                                | 26.216                               | 38.725                                    | 10.987                                 | -28.890                                   | 31.24                                | 0.601                                     | 5.0299                                 | 0.488                                     |
| 15        | 0.826                                | 27.913                               | 32.888                                    | 9.497                                  | -28.862                                   | 31.194                               | -0.891                                    | 5.082                                  | 1.016                                     |
| 16        | 0.878                                | 29.307                               | 26.963                                    | 8.007                                  | -28.824                                   | 31.168                               | -0.516                                    | 5.059                                  | -0.458                                    |
| 17        | 0.929                                | 30.399                               | 21.169                                    | 6.512                                  | -28.973                                   | 31.229                               | 1.180                                     | 5.010                                  | -0.936                                    |
| 18        | 0.981                                | 31.193                               | 15.388                                    | 4.999                                  | -29.329                                   | 31.209                               | -0.384                                    | 5.010                                  | -0.006                                    |
| 19        | 1.041                                | 28.346                               | -47.465                                   | 7.903                                  | 48.403                                    | 31.209                               | 0.000                                     | 5.010                                  | 0.000                                     |
| 20        | 1.101                                | 28.343                               | -0.040                                    | 7.962                                  | 0.980                                     | 31.209                               | 0.000                                     | 5.010                                  | 0.000                                     |
| 21        | 1.161                                | 28.339                               | -0.075                                    | 8.019                                  | 0.937                                     | 31.209                               | 0.000                                     | 5.010                                  | 0.000                                     |

The working rake and relief angles along the cutting edge are plotted in Fig. 4-9 for the points in Table 3. As it can be seen in Fig. 4-9, these angles in the proposed blades are constant while for the conventional blade, they have large variations.

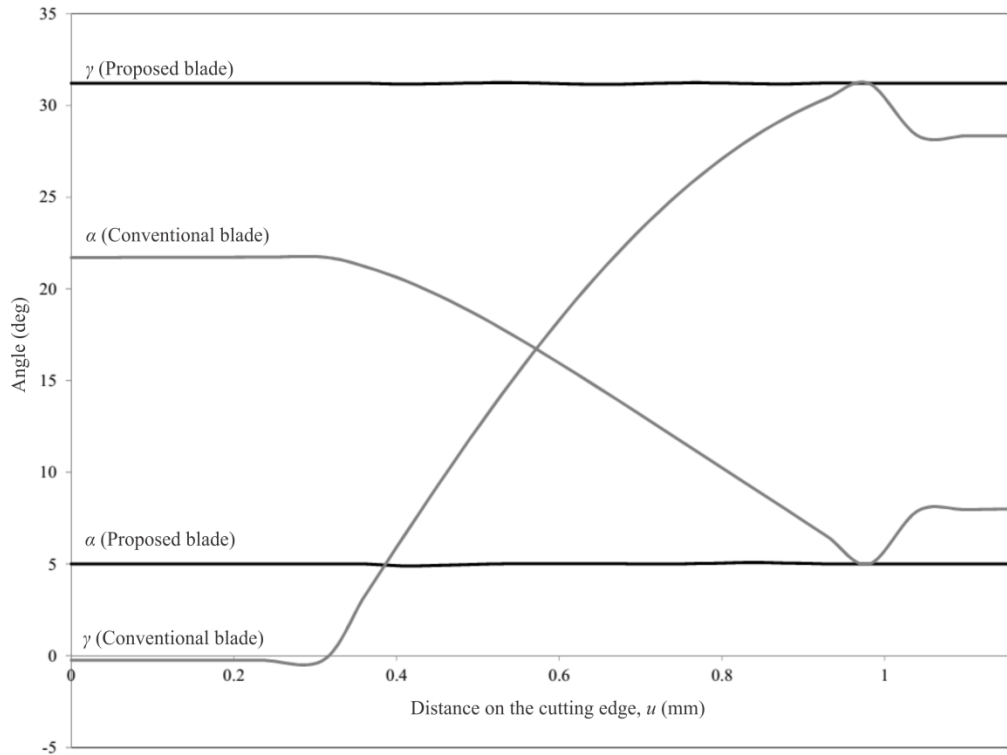


Fig. 4-9 The working rake ( $\gamma$ ) and relief ( $\alpha$ ) angles along the cutting edge for the conventional and proposed blade.

Therefore, based on the discussion in Section 4.3, the proposed blade has a better tool wear characteristic especially at the corner. In addition, in the followings, in order to demonstrate the improvement of the tool wear characteristics of the proposed blade, finite element simulations in Third Wave AdvantEdge® are carried out.

The tool wear is a result of thermal and mechanical loads on the tool during chip formation [9]. Therefore, in order to analyze the tool wear for both conventional and proposed blade, the tool load should be investigated and compared with each other. The tool load can be investigated as temperature, stress distribution along the cutting edge and cutting forces. Since temperature and stress distribution are difficult to be captured using metrological tools [9], finite element simulations in three dimensions are carried out in the present work.

In face-milling or face-hobbing, uneven load distribution along the cutting edge occurs because of uneven undeformed chip thickness and the shape of the cutting edge and rake and relief surfaces. The undeformed chip thickness in section I and II (Fig. 3-3) of the cutting edge (tool tip flanks) is larger than section III (side flank). In other words, the chip thickness decreases from

section I and II to section III continuously. Since in this chapter, only the gradients of the working rake and relief angles are considered, in order to nullify the effect of uneven chip thickness in the simulation results, the simulations are carried out with uniform undeformed chip thickness (.12 mm) to see only the influence of constant angles.

In order to simulate face-hobbing in Third Wave®, Grooving process is selected where the tool could be considered fixed and the workpiece is feed towards the cutter. Cutting speed is 300 m/min. Workpiece and tool materials are selected as Al6061-T6 and Carbide from the software's library. Maximum and minimum element sizes for the tool are assigned to 1mm and 0.02mm, respectively. Minimum element size is assigned to the cutting edge as well as rake and relief surfaces near to the cutting edge. Minimum chip element is set to 0.01mm and initial temperature is 20 °C. The workpiece and tool CAD models are modeled in CATIA™ and then, STEP models of them are imported in Third Wave®. When STEP models of the tool and workpiece are imported to the software, it requires assigning boundary conditions on both models. All nodes on the assigned boundary surfaces are fixed. In the simulations, back face of the cutter and peripheral surfaces of the workpiece which are not engaged in the cutting process are set as boundaries.

Fig. 4-10 shows the simulations. The left and the right side of Fig. 4-10 simulate the machining process using the conventional and proposed blade model, respectively. Since the corner of the blade is more prone to be worn out, the blade corner and small portions of the cutting edge connecting to the corner are considered in the simulation. The proposed blade produces chips with more curvature than conventional blade which means in terms of chip formation, the proposed model has better characteristics.

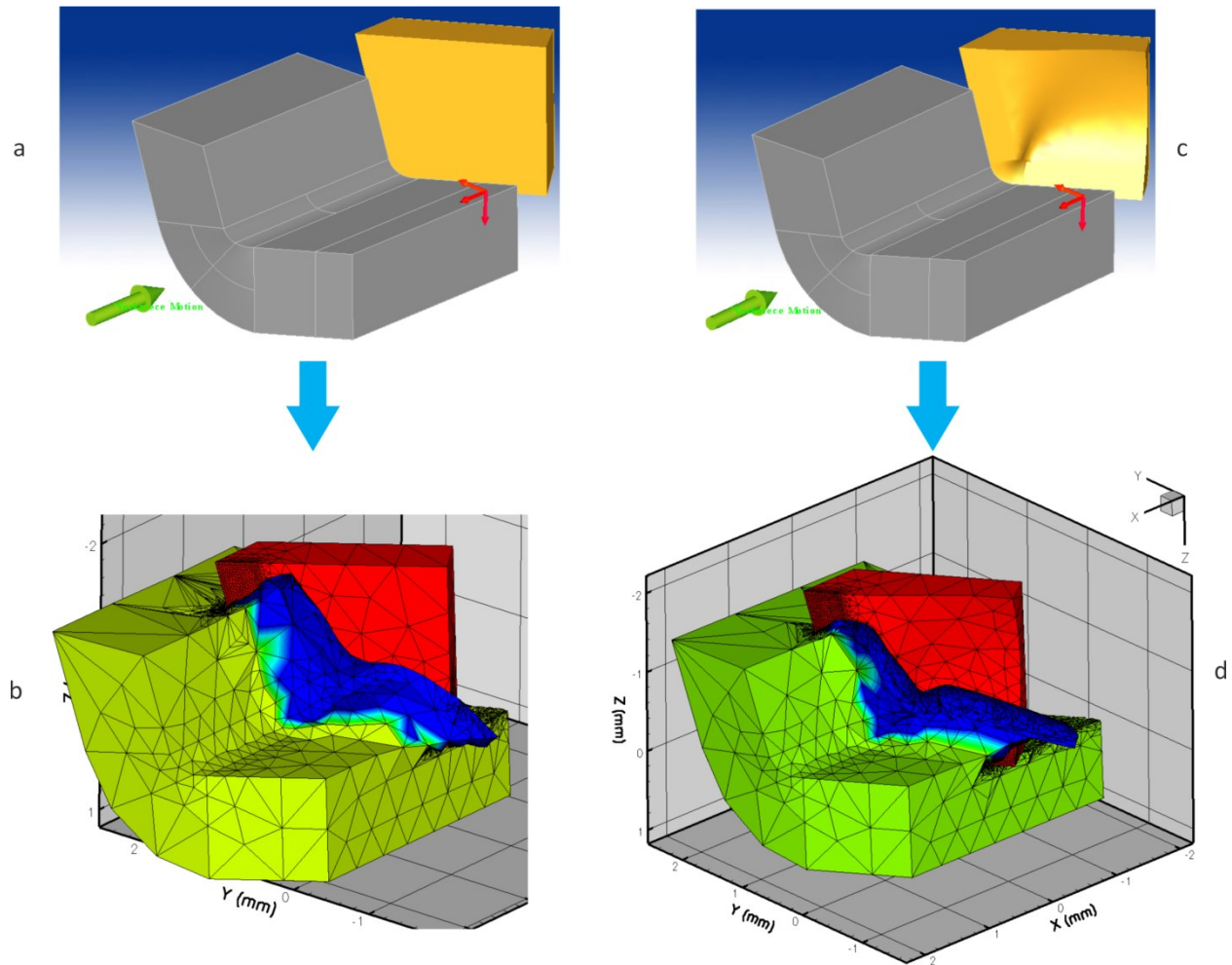


Fig. 4-10 FE machining simulations, a and b: Conventional and proposed blade tests modeled in Third Wave®, respectively. c and d: Conventional and proposed blade chip removal simulations in Third Wave®, respectively.

Temperature and stress distribution as well as cutting forces are investigated and compared between these two blades (the conventional and proposed blade) at a certain machining time ( $3.73 \times 10^{-4}$  s) to see the difference regarding the tool wear characteristics.

Temperature distribution is shown in Fig. 4-11. As it can be seen, temperature is concentrated at the corner of the conventional blade, but in the proposed blade, temperature concentration at the corner is prevented and moved to the flanks. Therefore, by eliminating the temperature concentration at the corner, the proposed blade has a better tool wear property at the corner.

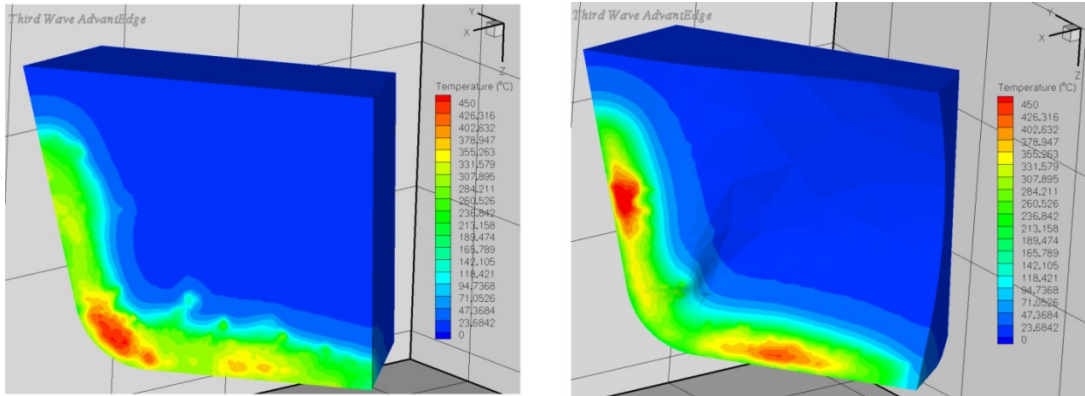


Fig. 4-11 Temperature distribution in the conventional (left) and proposed (right) blades.

Fig. 4-12 shows the Mises stress distribution. Stress has an even distribution along the cutting edge in the proposed blade while in the conventional tool stress is more concentrated at the corner.

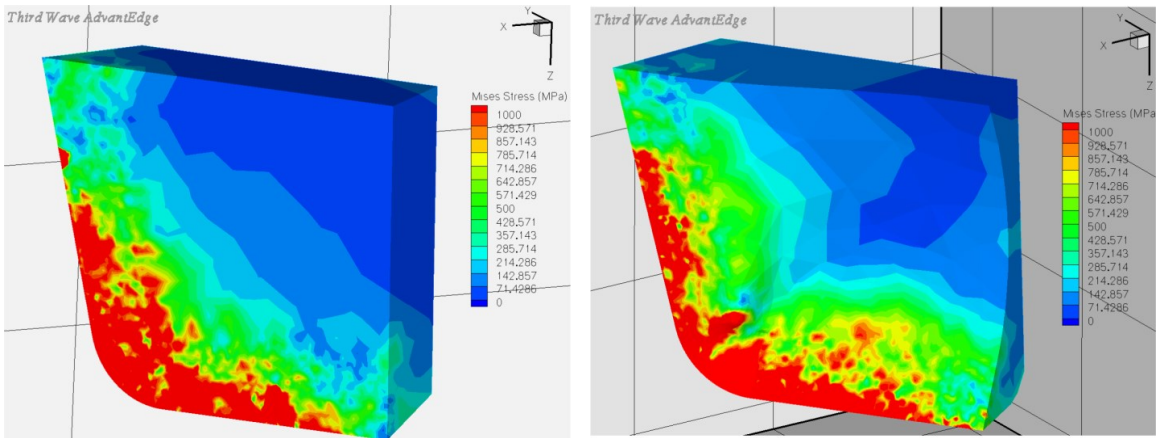


Fig. 4-12 Mises stress distribution in the conventional (left) and proposed (right) blades.

As mentioned earlier, the undeformed chip thickness is assumed uniform in the simulations while in the real face-hobbing the side flank experiences larger undeformed chip thickness than the tool tip flanks. Therefore, considering this fact, temperature and stress are less than the results shown in Fig. 4-11 and Fig. 4-12 at the side flank of the blade in the real face-hobbing. Maximum temperature and stresses (455°C and 3530 Mpa respectively) for both conventional and proposed blades are almost the same, but regions where they occur as well as stress and temperature distributions are different. As it can be seen, in the proposed blade, the corner, which is more prone to be worn out, is in a safer condition, in comparison with the conventional blade, by

moving stresses and temperature to the flanks. In the conventional blade stress and temperature are concentrated at the tool corner.

The conventional and proposed blade produce 350N and 280N cutting forces in the feed direction, respectively. It indicates that the proposed blade creates 70N less cutting force than the conventional blade. Thus, less cutting forces are applied on the proposed blade which causes an improvement in the tool wear characteristics.

In summary of FE machining simulation results, the comparison between the tool load (temperature, stress and cutting forces) of the conventional and proposed blades shows that the proposed blade performs better than the conventional blade in terms of the tool wear characteristics.

#### **4.6 Conclusion**

This paper presents a new method to design the cutting blades in face-hobbing of bevel and hypoid gears in order to decrease the gradients of the working rake and relief angles along the cutting edge. For this purpose, the working rake and relief angles are kept constant considering the complex nature of the face-hobbing process, varying cutting velocity along the cutting edge, the cutting system geometry (the blades and cutter head) and the machine tool kinematics. Since, large variations in the working rake and relief angles cause the local tool wear especially at the corners of the conventional blades, by reducing these variations (theoretically to zero), the tool wear characteristics are improved in the proposed blade. In addition, in this paper, complete mathematical representations of the cutting system including the cutter head and the blades are presented.

In order to verify the proposed method, the working rake and relief angles are measured on the proposed and conventional blade models at the corresponding points. The measurement shows that the working rake and relief angles along the cutting edge of the proposed blade are kept constant while these angles in the conventional blades have large variations along the cutting edge especially around the tool corner. In order to validate the performance of the proposed blade in machining, FE simulations are carried out on the conventional and proposed blades. The comparison between the tool load (temperature and stress distribution and cutting forces) shows the proposed blade model performs better than the conventional blade in terms of the tool wear characteristics. The temperature and stress are distributed along the cutting edge in the proposed

blade more even than the conventional one. Moreover, the produced cutting force in feed direction in the proposed blade is less than the conventional blade.

Another geometrical related factor in the tool wear phenomena is the gradient of the un-deformed chip thickness along the cutting edge. The largest gradient occurs at the tool corner. If the un-deformed chip thickness remains constant, the tool wear characteristics are improved especially at the corner. Because of the complexity of the face-hobbing process, derivation and controlling un-deformed chip thickness along the cutting edge is challenging. This is the subject of the future research of the authors.

The surfaces of the re-designed blade model have some complex geometries which may cause stress concentration especially at regions around the corner where the curvature change is considerable. Further studies and experimental tests are needed to investigate the effect of stress concentration on the tool life of the re-designed blade.

## Chapter 5

# Workpiece in-process model and un-deformed Chip Geometry in Face-hobbing of Bevel Gears

### Citations:

- 1- Habibi, M., Chen, Z.C., 2015, “An Accurate and Efficient Approach to Un-deformed Chip Geometry in Face-hobbing and its Application in Cutting Force Prediction”, *ASME Journal of Mechanical Design*, 138(2):023302-023302-11, doi: 10.1115/1.4032090.
- 2- Habibi, M., Chen, Z.C., 2016, “A Semi-analytical Approach to Un-deformed Chip Boundary Theory and Cutting Force Prediction in Face-hobbing”, *Computer Aided Design*, 73, pp. 53-65, doi: 10.1016/j.cad.2015.12.001.

### 5.1 Introduction

Face-hobbing is the most productive process to manufacture bevel gears. Due to the high productivity of the process, tool wear is a serious challenge in face-hobbing. The tool wear phenomenon is a result of excessive and varying cutting force distribution along the cutting edges of the blades in face-hobbing. Although face-hobbing is quite widespread, there is little research



on cutting force and un-deformed chip geometry in this process. The machining performance (tool wear, deflection, breakage chatter and etc.) are affected severely by machining settings and instantaneous un-deformed chip geometry.

The conventional method to derive the un-deformed chip geometry is to obtain instantaneous in-process model of the workpiece during machining. Nikolaos and Artomenis [34], Vasilis et al. [51], Dimitrou and Antoniadis [52] and Artomenis [53] implemented CSG (Constructive Solid Ground) method and Boolean operation to simulate hobbing of helical gears. They developed software called HOB3D® for hobbing simulation. Brecher et al. ([9], [10] and [11]) simulated face-milling of bevel gears using ray tracing and STL (triangular mesh) penetration calculation. They implemented their algorithm in face-milling simulation software called KegelSpan®. All the mentioned research works have implemented computationally expensive methods. Moreover, they have not worked on face-hobbing.

Face-hobbing is the most complicated bevel gear manufacturing process because of varying cutting velocity along the cutting edge of the cutting blades. This kind of varying velocity is created due to special geometry of the cutting system and multi-axes machine tool kinematic chains. Therefore, obtaining instantaneous un-deformed chip geometry is a challenging process. The only research work on un-deformed chip geometry in face-hobbing was conducted by Habibi and Chen [18]. They have proposed numerical methods to obtain the projection of un-deformed chip geometry on the rake face of the cutting blades,  $Ch_p$ , by discretizing the workpiece into two dimensional elements, disks, and intersecting the cutting edge of all blades with each disk. Although their methods are able to obtain the chip geometry and predict the cutting forces in non-generated face-hobbing, the computational cost of the methods is quite high (in scale of hours) and the accuracy of the derived chip geometry severely depends on how fine the workpiece is discretized. In addition, finer discretization means even higher computational cost. Moreover, the method fails to represent the accurate  $Ch_p$  on the rake especially near the tool tip where is a critical region because cutting force distribution is the highest in this area. The method is mainly inefficient due to fact that the approximate workpiece in-process model needs to be obtained numerically prior to derive the chip geometry. The method of [18] is discussed in details in Section 5.2.

In Section 5.3, a semi-analytical approach is introduced to define  $Ch_p$  mathematically in non-generated face-hobbing. Closed form formulations of boundaries and the area of  $Ch_p$  are

obtained. Since the boundaries are piecewise, the curve parameter range of each piece is derived numerically by solving constructed equations. Since the un-deformed chip geometry is defined semi-analytically, the computational cost is reduced drastically from hours (using numerical method presented in [18]) to scale of few seconds. In addition, the accuracy of the chip geometry is quite high in comparison with the results of [18]. Since the cutting velocity varies along the cutting edge, the differential undeformed chip geometry is defined locally at each point on the cutting edge considering the corresponding cutting velocity.

In the present chapter, two approaches, numerical and semi-analytical, to undeformed chip geometry in face-hobbing are introduced.

## 5.2 Numerical Approach

### 5.2.1 In-process Model

In order to derive the un-deformed chip geometry, the in-process model of the workpiece during machining simulation is needed to be obtained. In the previous section the gear workpiece is discretized into disks along z axis. In Fig. 5-1, these disks are shown. In order to create an in-process model of the workpiece, the envelop of the cutting edge on each disk is calculated when it passes through disks. This envelope consists of intersection points between cutting edge and the rake face, and each disk.

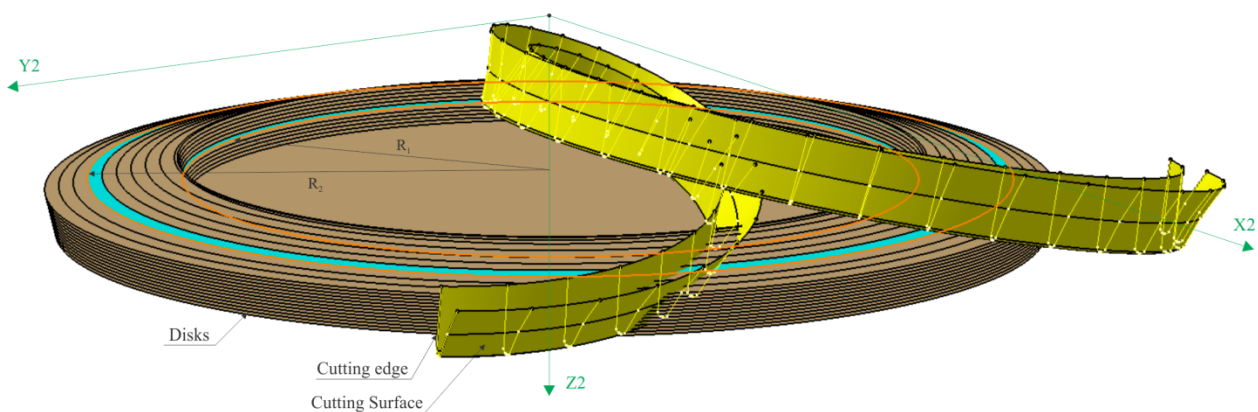


Fig. 5-1 The discretized workpiece and cutting surface

In Fig. 5-2.a four locations of the outside blade are shown schematically when the cutting edge moves from  $\theta_1$  to  $\theta_4$  ( $\theta_1 < \theta_2 < \theta_3 < \theta_4$ ). These four locations represent three main cases for the

cutting edge and disks intersection. In case I, there is no intersection point. In case II, there are two intersection points, one inside  $j^{th}$  disk and one on the outside circle ( $R_2$ ) of  $j^{th}$  disk. In case III, there are two intersection points, both in  $j^{th}$  disk.

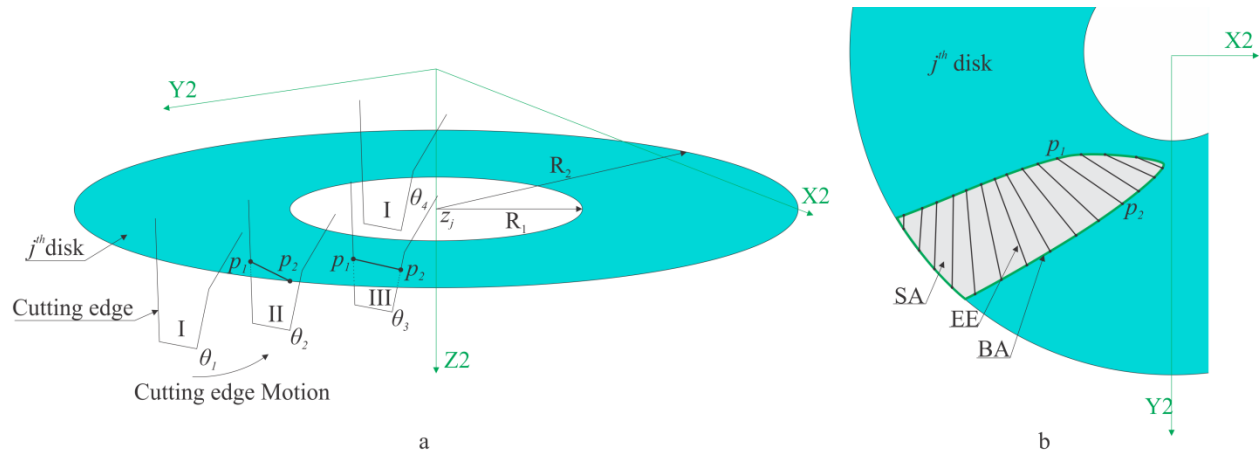


Fig. 5-2 Intersection between cutting edge and a disk

The line segment  $p_1p_2$  is called Effecting Cutting Edge, EE, on  $j^{th}$  disk. This line segment is swept on  $j^{th}$  disk while the cutting edge is passing through the disks. The result of this sweeping motion is a closed area called Cutter Swept Area, SA, on  $j^{th}$ , see Fig. 5-2.b. SA is confined by its boundary, BA, which consists of points  $p_1$  and  $p_2$  of each EE. In other words, SA on  $j^{th}$  disk represents the removed area by EE. It is important to mention that in face-hobbing, EEs of one blade when it passes through a disk, do not have intersection with each other which it means there is no pre-cut. At each position of the cutting edge, the curve parameter of intersection points,  $s_{int}$ , can be obtained by solving

$$(r_w)_z = z_j, \quad (5-1)$$

where  $z_j$  is the height of  $j^{th}$  disk. Two points are calculated by substituting  $s$  into  $r_w$ . Between those two points, one which is inside the disk is considered as the intersection point (like  $p_1$  in case II and  $p_1$  and  $p_2$  in case III in Fig. 5-2.a). If the point is outside of the disk, intersection between boundaries of  $j^{th}$  disk and the connecting line of those two points is considered as another intersection point (like  $p_2$  in case II in Fig. 5-2.a).

The cutting edge consists of seven sections. The form of the formulations for calculating  $s_{int}$  in Eq. (5-1) for sections I, III, VI and VIII of the cutting edge are similar because all of them are straight lines.  $s_{int}$  is a function of elements of  $M_{wh}, M_{ht}, P_t$  and  $n_b$  which eventually leads to the fact

that  $s_{int}$  is in terms of  $\theta$ . For other sections of the cutting edge (II, III and VII), a trigonometric equation should be solved to calculate  $s_{int}$ . This equation can be written as

$$A \cdot \cos(Q) + B \cdot \sin(Q) + C = 0, \quad (5-2)$$

where A, B and C are functions in terms of elements of  $M_{wh}, M_{ht}, n_b, \rho$  and  $r_e$ . The equation of Q for sections II, III and VII is as follows:

$$\begin{cases} Q = s_2 / r_e, & II \\ Q = (-\delta \cdot \rho - s_4 + L_1 + L_2) / \rho, & III \\ Q = -(v_7 - L_5 - L_6) / r_e + \gamma_2, & VII \end{cases} \quad (5-3)$$

Solving Eq. (5-3) for Q leads to two answers as

$$Q_1 = \arctan \left( \left( \frac{-\left(-A \cdot \left(C \cdot A - \sqrt{A^2 \cdot B^2 + B^4 - B^2 \cdot C^2}\right)\right)}{(A^2 + B^2) \cdot B} + \frac{C}{B} \right), \frac{-\left(C \cdot A - \sqrt{A^2 \cdot B^2 + B^4 - B^2 \cdot C^2}\right)}{(A^2 + B^2)} \right), \quad (5-4)$$

$$Q_2 = \arctan \left( \left( \frac{-\left(-A \cdot \left(C \cdot A + \sqrt{A^2 \cdot B^2 + B^4 - B^2 \cdot C^2}\right)\right)}{(A^2 + B^2) \cdot B} + \frac{C}{B} \right), \frac{-\left(C \cdot A + \sqrt{A^2 \cdot B^2 + B^4 - B^2 \cdot C^2}\right)}{(A^2 + B^2)} \right). \quad (5-5)$$

By substituting  $Q_1$  and  $Q_2$  into Eq. (5-1) and solving for  $s$ ,  $s_{int}$  is obtained. It should be noted that all intersection points must be inside the disks which means  $R_1 \leq d \leq R_2$  where  $d$  is the distance of each intersection point to the  $z$  axis of the workpiece,  $Z_w$ .

In face-hobbing, all blades contribute to remove material of each gear slot. Moreover, sometimes during machining more than one blade or even blade group are engaged with the workpiece. Therefore, all blades should be taken into account in order to obtain  $SA$  on all disks at each moment during machining. Fig. 5-3 shows the engagement of two blade groups at the same time ( $\theta = \theta_t$ ) with  $j^{th}$  disk. Grey areas have been already removed ( $SA_k$ ) when  $\theta \leq \theta_s$  ( $\theta_s$  is the cutter head angle when outside blade of  $n_b^{th}$  group engaged with the  $SA_k$  and  $\theta_s < \theta_t$ ).  $EE_{n_b}^{I/O}$  (subscript and superscript represent the blade group number and, inside or outside blade, respectively) is shown by bold lines in Fig. 5-3.  $SA_{n_b}$  and  $SA_{n_b+1}$  are swept areas by  $n_b^{th}$  (green areas in Fig. 5-3) and  $(n_b+1)^{th}$  (purple areas in Fig. 5-3) blade groups when the cutter head rotates from  $\theta_t$  to  $\theta_s$ .

Faded areas of  $SA_{n_b}$  and  $SA_{n_b+1}$  are inside  $SA_k$ s and do not contribute in machining since there is no material to be removed there. The projection of the un-deformed chip on the rake face,  $Ch_p$ , on disks is in shape of line segments which they are called Chip Line,  $CL$ .  $CL_{n_b}^{I/O}$ s are shown in Fig. 5-3 by red lines on  $EE_{n_b}^{I/O}$  at  $\theta_t$ . The geometry of  $Ch_p$  of inside or outside blade is obtained by stacking up  $CL_{n_b}^{I/O}$  of all disks.

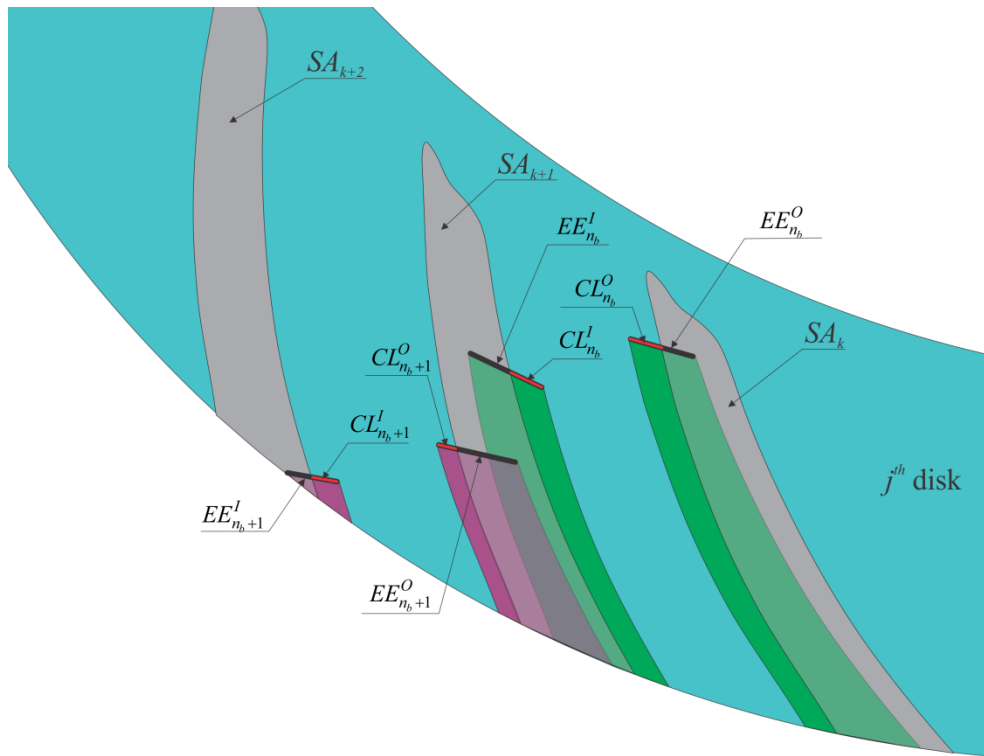


Fig. 5-3 The engagement of two blade groups with  $j^{th}$  disk.

Face-hobbing, in terms of contribution of each blade in creating the in-process workpiece, behaves as a linear system and follows the superposition principle. It means that the in-process model of the workpiece at a specific time can be obtained by simulating the machining for each individual blade and then combining the effect of all blades together.

### 5.2.2 Chip geometry

Since, in the previous section, the in-process model of the workpiece is obtained, finding the geometry of  $Ch_p$  is a straightforward process. Assume the in-process model is obtained until a specific rotation of the cutter head,  $\theta = \theta_f$ . Fig. 5-4 shows the schematic illustration of the process. The green contours are the cutting envelopes for a specific gear slot between two

successive teeth where  $\theta \leq \theta_f$ . At this location, the cutting edge is intersected with the boundary of the swept area,  $BA_j$ , which results few intersection points on  $j^{th}$  disk, points  $p_1, p_2, p'_1$  and  $p'_2$ , see Fig. 5-4. The number of intersection points on each disk varies based on the geometry of the cutting envelops and the position of the cutting edge on the disks. The geometry of  $Ch_p$  (Chip Lines, CL) on  $j^{th}$  disk is obtained by processing points  $p_1, p_2, p'_1$  and  $p'_2$  by the following algorithm:

```

If (the number of intersection points=2)
    CL=Line( $p_1, p_2$ ) (connecting line segment between  $p_1$  and  $p_2$ .
elseif (the number of intersection points=3)
    If ( $(p_1$  is inside of  $BA_j$ ) and ( $p_2$  is on  $BA_j$ ))
        CL=Line( $p'_1, p_2$ )
    elseif ( $(p_1$  is on  $BA_j$ ) and ( $p_2$  is inside of  $BA_j$ ))
        CL=Line( $p_1, p'_1$ )
    end
elseif (the number of intersection points=4)
    CL={Line( $p_1, p'_1$ ), Line( $p'_2, p_2$ )}
End.

```

Eventually, the un-deformed chip geometry on the rake face is constructed by connecting corresponding CL of  $j^{th}$  disk to  $(j+1)^{th}$  and  $(j-1)^{th}$ . CL on the first disk is connected to the second disk and CL on the last disk is extrapolated by  $\Delta Z$  (Fig. 5-4bottom). More accurate  $Ch_p$  can be obtained by finer discretization of the workpiece.

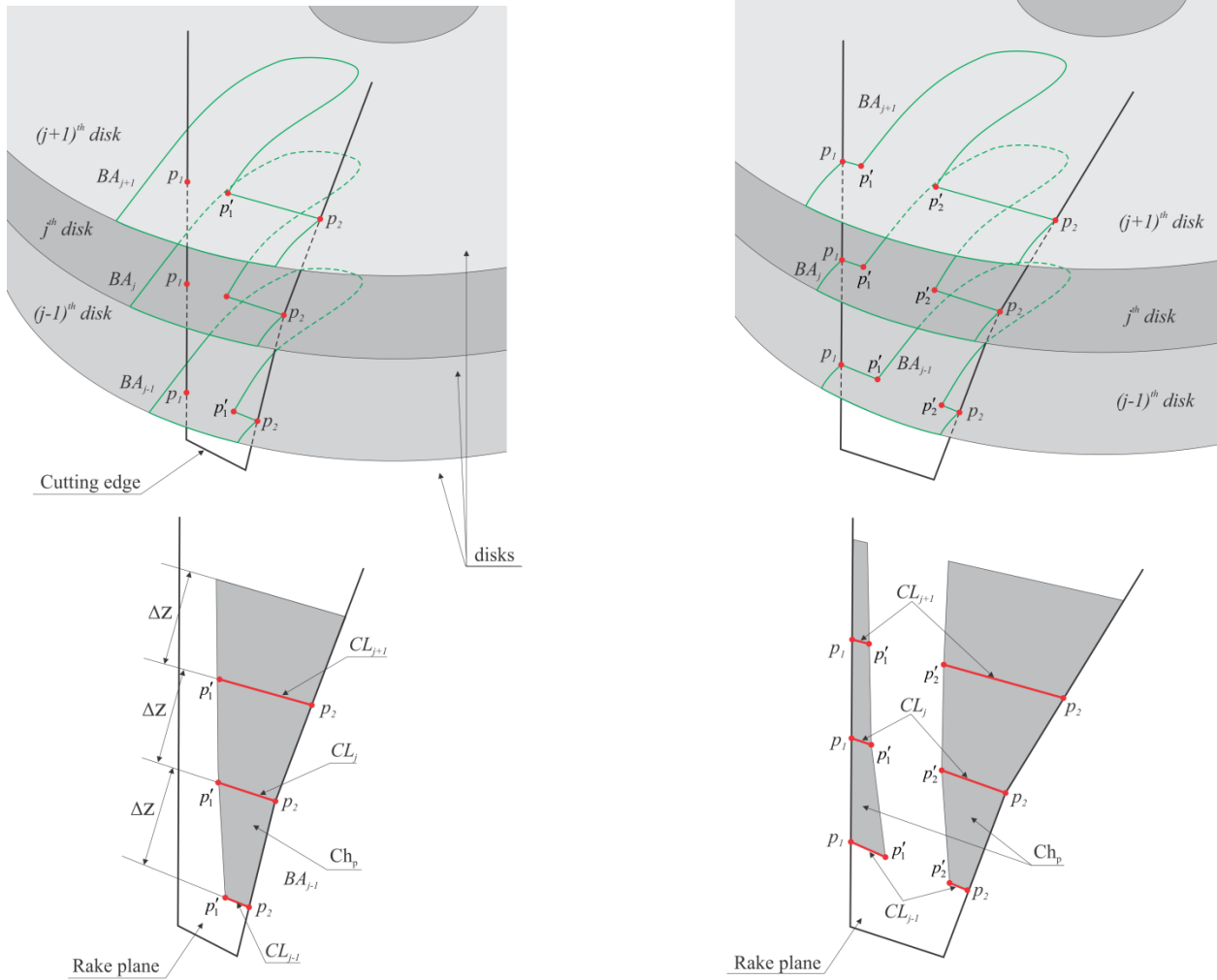


Fig. 5-4 Un-deformed chip geometry derivation

Fig. 5-5 shows an example of the derived un-deformed chip geometry on the inside and the outside blade for a specific moment during machining process. Since the cutter head rotates with a very high speed (like 1000RPM) and the process lasts for almost several minutes, the value of the rotation angle of the cutter head,  $\theta$ , can easily being very large (as in Fig. 5-5 this value is  $16234 \text{ deg}$ ).

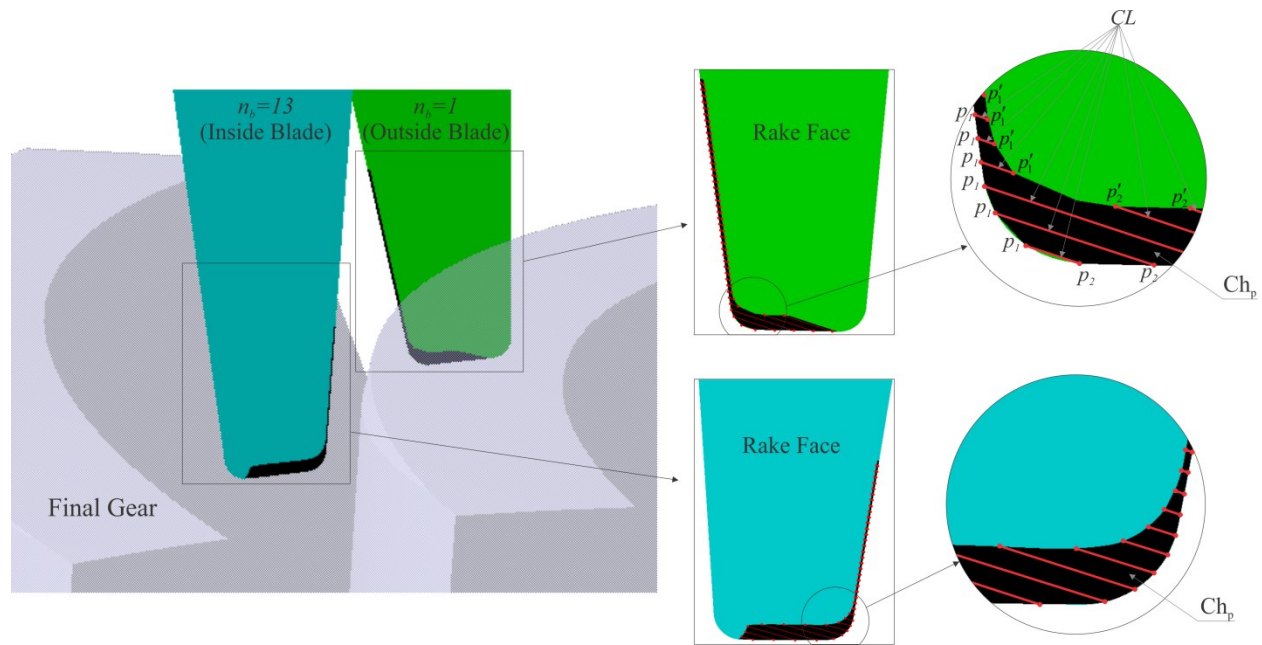


Fig. 5-5 An example of un-deformed chip geometry derived using the proposed methods at  $\theta=16234 \text{ deg}$  and  $BO=7.908 \text{ mm}$ .

### 5.2.3 Case study

The in-process model of the gear workpiece is derived using the method proposed in Section 5. In Fig. 5-6, the in-process model of a disk is shown in different cutter head rotation angle. The continues material removal behavior of the process is clearly illustrated in this figure. It is important to notice that all cutting blades, all 13 blade groups (26 blades), are considered to create the in-process model in Fig. 5-6.



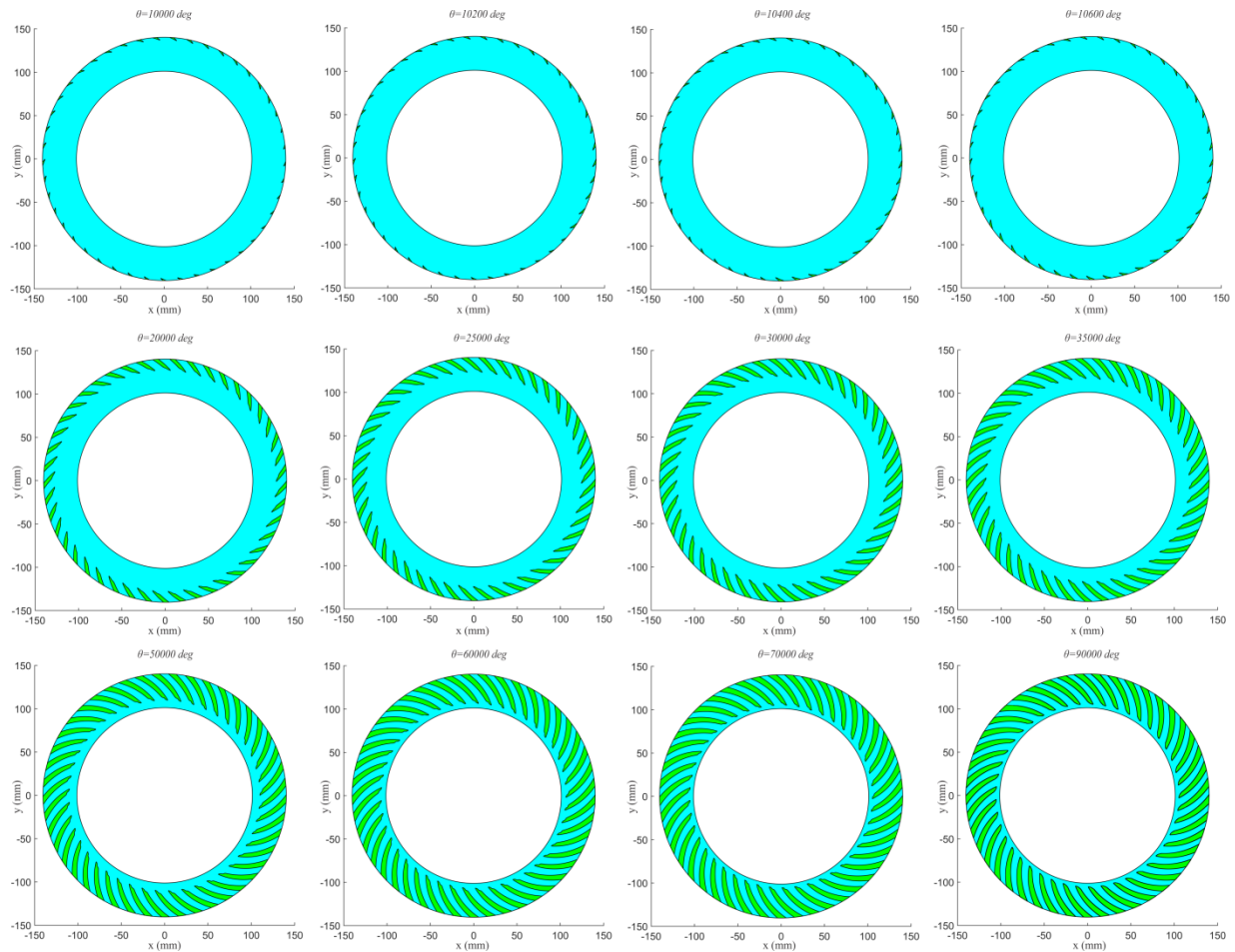


Fig. 5-6 The in-process model of 100<sup>th</sup> disk for different cutting system rotation angle,  $\theta$ , the green area is the removed area.

Although, in order to obtain the in-process model, all the cutting blades should be considered, but in order to study the material removal behavior of the cutting blades, it is not necessary to predict cutting forces for all the cutting blades, only one blade group is enough.

### 5.3 Analytical Approach

#### 5.3.1 Projection of un-deformed chip geometry on rake face, $Ch_p$

Fig. 5-7 shows the core idea of obtaining the projection of the un-deformed chip geometry,  $Ch_p$ , on the rake plane of the outside blade schematically. The geometry of  $Ch_p$  is derived at any rotation angle of the cutter head,  $\theta_c$ , on the rake face of the outside blade of blade group  $n_b$  during face-hobbing. The most important significance of the proposed method is that the workpiece in-

process model is integrated semi-analytically in the boundary theory of the chip provided in the present paper. In other words, the in-process model is implemented in the boundaries of the chip formulations. Boundaries of the chip are  $\mathbf{C}_1$ ,  $\mathbf{C}_2$ ,  $\mathbf{C}_3$  and  $\mathbf{C}_4$  (Fig. 5-7). Curve  $\mathbf{C}_1$  is the cutting edge of the blade (from group  $n_b$ ) that the cutting forces are predicted on it at any rotation angle of the cutter head,  $\theta_c$ . However, curves  $\mathbf{C}_2$ ,  $\mathbf{C}_3$  and  $\mathbf{C}_4$  represent the in-process model of the workpiece at  $\theta_c$ .  $\mathbf{C}_2$  and  $\mathbf{C}_3$  are derived from the cutting surfaces of the last outside and inside blades which have passed through the same gear slot and close to the blade from group  $n_b$  (the blade that the cutting forces are going to be predicted on). Curve  $\mathbf{C}_4$  is derived from the boundary surfaces of the workpiece. Therefore, using the proposed method, the need for updating in-process model is eliminated by integrating it into the boundary theory of the chip derivation. Obtaining the in-process model was the core of the conventional methods to derive chip geometry in such a way that at every time instant during machining this model must be updated (most of the times using computationally expensive numerical methods such as STL penetration, Boolean operation or Z-buffer representation).

Curve  $\mathbf{C}_1$  in Fig. 5-7 is the cutting edge of the outside blade of blade group  $n_b$  at  $\theta_c$ ,  $\mathbf{C}_1 = \mathbf{r}_w(s, \theta_c)$ . The workpiece in-process model right before  $\theta_c$ , the machined workpiece, is created by cutting surfaces of the last outside,  $\mathbf{S}_{EO}$ , and inside blades,  $\mathbf{S}_{EI}$ , which have passed through the same gear slot and close to the current location of the outside blade at  $\theta_c$ .  $\mathbf{S}_{EO}$  and  $\mathbf{S}_{EI}$  are called the effective cutting surfaces of the outside and inside blades, respectively. Curves  $\mathbf{C}_2$  and  $\mathbf{C}_3$  are the intersections between the cutting surfaces,  $\mathbf{S}_{EO}$  and  $\mathbf{S}_{EI}$ , and the rake face, respectively.

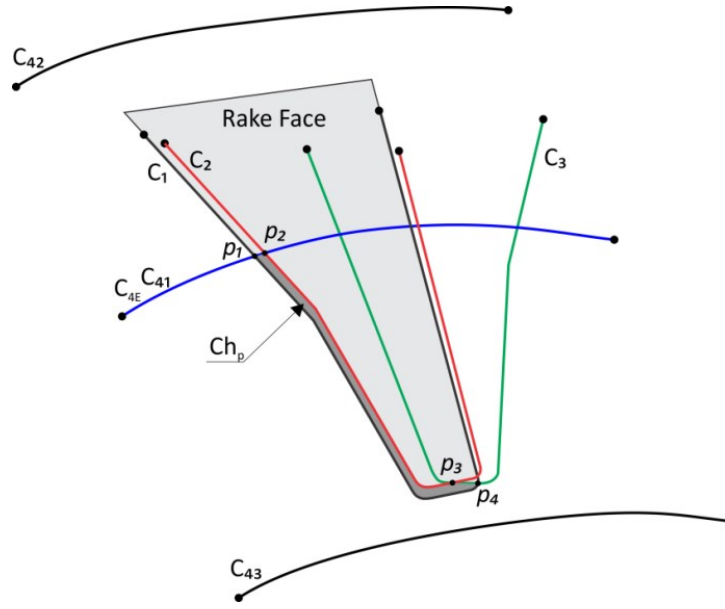


Fig. 5-7 The projection of the un-deformed chip geometry,  $Ch_p$ , on the rake plane of the outside blade.

In order to detect which blade groups creates  $S_{EO}$  and  $S_{EL}$ , a minimization problem is constructed and solved. The coordinates of the origin of coordinate system  $St$  of an outside blade of blade group  $n$  in  $Sw$ ,  $\mathbf{O}_{tw}$ , is obtained as

$$\mathbf{O}_{wt}(\theta, n) = \mathbf{M}_{wh} \begin{bmatrix} \cos\left(\frac{2 \cdot (n-1) \cdot \pi}{N_b}\right) \cdot X - \sin\left(\frac{2 \cdot (n-1) \cdot \pi}{N_b}\right) \cdot Y \\ \sin\left(\frac{2 \cdot (n-1) \cdot \pi}{N_b}\right) \cdot X + \cos\left(\frac{2 \cdot (n-1) \cdot \pi}{N_b}\right) \cdot Y \\ h_f \\ 1 \end{bmatrix}. \quad (5-6)$$

The goal is to determine the effective blade group number of an outside blade,  $n_{EO}$ , in such a way that the distance between  $\mathbf{O}_{wt}\left(\theta_c - \frac{2\pi}{R_b}, n_{EO}\right)$  and the origin of the coordinate system  $St$  of the outside blade of blade group  $n_b$ ,  $\mathbf{O}_{wt}(\theta_c, n_b)$ , is minimized. Hence, the objective function of the minimization problem can be written as

$$F_E = \left| \mathbf{O}_{wt}\left(\theta_c - \frac{2\pi}{R_b}, n_{EO}\right) \mathbf{O}_{wt}(\theta_c, n_b) \right|. \quad (5-7)$$

It should be noted that the last time that the blades of the cutter head were inside a gear slot where the outside blade of blade group  $n_b$  is machining at  $\theta_c$ , is  $\frac{2\pi}{R_b}$  before  $\theta_c$ . Therefore, the effective cutting blade can be found at  $\theta_c - \frac{2\pi}{R_b}$ . The group number of the effective inside blade,  $n_{EI}$  is one group less than  $n_{EO}$ , therefore,  $n_{EI}=n_{EO}-1$ . This rises from the fact that right before the effective outside blade of group  $n_{EO}$ , the effective inside blade from previous blade group,  $n_{EO}-1$ , is engaged with the workpiece.

$\mathbf{C}_1$ ,  $\mathbf{C}_2$  and  $\mathbf{C}_3$  are piecewise curves.  $\mathbf{C}_1$  is the cutting edge of the outside blade of group  $n_b$  and is represented analytically as  $\mathbf{C}_1 = \mathbf{r}_w(s, \theta_c)$ . However,  $\mathbf{C}_2$  and  $\mathbf{C}_3$  are intersections of the rake face of the outside blade of group  $n_b$  with effective cutting surfaces,  $\mathbf{S}_{EO}$  and  $\mathbf{S}_{EI}$ , respectively. The cutting surfaces are also piecewise surfaces. The formulations of all pieces of  $\mathbf{C}_2$  and  $\mathbf{C}_3$  are derived analytically in the following.

The mathematical representation of the rake plane of the outside blade of group  $n_b$  can be written as

$$\mathbf{V}_{bw} \cdot (\mathbf{P} - \mathbf{T}\mathbf{T}) = 0, \quad (5-8)$$

where  $\mathbf{P}$  is a point on the rake plane and

$$\mathbf{V}_{bw}(\theta) = \mathbf{M}_{wh}(\theta) \mathbf{V}_b. \quad (5-9)$$

In order to derive the equation of  $\mathbf{C}_2$ , the effective cutting surface,  $\mathbf{S}_{EO}$ , is substituted for  $\mathbf{P}$  into Eq. (5-8)

$$\mathbf{V}_{bw} \cdot (\mathbf{r}_{w,i}(\theta, s) - \mathbf{T}\mathbf{T}) = 0, \quad (5-10)$$

where  $i=I, II, III, IV, VI, VII$  and  $VIII$ .

The effective cutting surface of the outside blade,  $\mathbf{S}_{EO}$ , consists of six pieces corresponding to generating parts of the cutting edge. Part I of  $\mathbf{S}_{EO}$  is created by  $\mathbf{r}_{w,i}(s)$  which is a straight line in terms of  $s$ . Therefore, for part I, Eq. (5-10) can be solved directly for  $s$  in terms of  $\theta$  as  $s_1 = g_1(\theta)$ .

Since parts III, VI and VIII are also generated by the straight segments of the cutting edge therefore, like part I, solving Eq. (5-10) for  $s$  leads to  $s_{\text{III}} = g_{\text{III}}(\theta)$ ,  $s_{\text{VI}} = g_{\text{VI}}(\theta)$  and  $s_{\text{VIII}} = g_{\text{VIII}}(\theta)$ .

Parts II, IV and VII of the cutting edge are arcs. Therefore, Eq. (5-10) can't be solved directly for  $s$  by its current shape. By substituting  $\mathbf{r}_{\text{w,II}}(s)$ ,  $\mathbf{r}_{\text{w,IV}}(s)$  and  $\mathbf{r}_{\text{w,VII}}(s)$  into Eq. (5-10), this equation can be reformulated as

$$A(\theta) \cdot \cos(Q(s)) + B(\theta) \cdot \sin(Q(s)) + C(\theta) = 0, \quad (5-11)$$

where  $A$ ,  $B$  and  $C$  are functions in terms of  $\theta$ , however in order to construct it, elements of  $\mathbf{M}_{\text{wh}}$ ,  $\mathbf{M}_{\text{ht}}$ ,  $\mathbf{V}_b$  and geometric parameters of the cutting blade are used. The equation of  $Q$  for sections II, III and VII is as follows:

$$\begin{cases} Q = s / r_e, & \text{II} \\ Q = (-\delta \cdot \rho - s + L_1 + L_2) / \rho, & \text{IV} \\ Q = -(s - L_5 - L_6) / r_e + \gamma_2, & \text{VII} \end{cases} \quad (5-12)$$

Solving Eq. (5-12) for  $Q$  leads to the following equation

$$Q = \arctan \left( \left( \frac{-\left(-A \cdot \left(C \cdot A - \sqrt{A^2 \cdot B^2 + B^4 - B^2 \cdot C^2}\right)\right)}{(A^2 + B^2) \cdot B} + \frac{C}{B} \right), \frac{-\left(C \cdot A - \sqrt{A^2 \cdot B^2 + B^4 - B^2 \cdot C^2}\right)}{(A^2 + B^2)} \right). \quad (5-13)$$

By substituting Eq. (5-13) into Eq. (5-12), the equations for  $s$  can be obtained as  $s_{\text{II}} = g_{\text{II}}(\theta)$ ,  $s_{\text{IV}} = g_{\text{IV}}(\theta)$  and  $s_{\text{VII}} = g_{\text{VII}}(\theta)$ . Eventually, the mathematical representation of  $\mathbf{c}_2$  can be written as

$$\mathbf{c}_2(\theta) = \begin{cases} \mathbf{r}_{\text{w,I}}(g_{\text{I}}, \theta) & \theta_{\text{I,1}} \leq \theta \leq \theta_{\text{I,2}} & \text{I} \\ \mathbf{r}_{\text{w,II}}(g_{\text{II}}, \theta) & \theta_{\text{II,1}} < \theta \leq \theta_{\text{II,2}} & \text{II} \\ \mathbf{r}_{\text{w,III}}(g_{\text{III}}, \theta) & \theta_{\text{III,1}} < \theta \leq \theta_{\text{III,2}} & \text{III} \\ \mathbf{r}_{\text{w,IV}}(g_{\text{IV}}, \theta) & \theta_{\text{IV,1}} < \theta \leq \theta_{\text{IV,2}} & \text{IV} \\ \mathbf{r}_{\text{w,VI}}(g_{\text{VI}}, \theta) & \theta_{\text{VI,1}} < \theta \leq \theta_{\text{VI,2}} & \text{VI} \\ \mathbf{r}_{\text{w,VII}}(g_{\text{VII}}, \theta) & \theta_{\text{VII,1}} < \theta \leq \theta_{\text{VII,2}} & \text{VII} \\ \mathbf{r}_{\text{w,VIII}}(g_{\text{VIII}}, \theta) & \theta_{\text{VIII,1}} < \theta \leq \theta_{\text{VIII,2}} & \text{VIII} \end{cases}, \quad (5-14)$$

where  $\theta_{i,1}$  and  $\theta_{i,2}$ ,  $i=I, II, III, IV, VI, VII$  and  $VIII$ , are lower and upper boundaries of  $s$  for different pieces which are obtained numerically. For pieces I, III and VI and VIII of  $\mathbf{c}_2$ ,  $\theta_{i,1}$  and  $\theta_{i,2}$  are obtained by solving Eq. (5-10) when lower and upper limits of curve parameter  $s$  of the corresponding piece of the cutting edge,  $s_{i,\min}$  and  $s_{i,\max}$ , are plugged in it. Therefore,  $\theta_{i,1}$  and  $\theta_{i,2}$  can be obtained by solving the following equations numerically, respectively,

$$s_{i,\min} = g_i(\theta_{i,1}), \quad (5-15)$$

$$s_{i,\max} = g_i(\theta_{i,2}). \quad (5-16)$$

For pieces II, IV and VI of  $\mathbf{c}_2$ ,  $\theta_{i,1}$  and  $\theta_{i,2}$  are obtained by solving Eq. (5-11) when lower and upper limits of curve parameter  $s$ , are plugged in it. Hence,  $\theta_{i,1}$  and  $\theta_{i,2}$  can be obtained by solving the following equations numerically, respectively,

$$A(\theta_{i,1}) \cdot \cos(Q(s_{i,\min})) + B(\theta_{i,1}) \cdot \sin(Q(s_{i,\min})) + C(\theta_{i,1}) = 0, \quad (5-17)$$

$$A(\theta_{i,2}) \cdot \cos(Q(s_{i,\max})) + B(\theta_{i,2}) \cdot \sin(Q(s_{i,\max})) + C(\theta_{i,2}) = 0. \quad (5-18)$$

The representation of  $\mathbf{c}_3$  can be obtained in the similar way as Eq. (5-14) for effective cutting surface of the inside blade,  $\mathbf{S}_{EI}$ . The equation of  $\mathbf{c}_3$  can be written as

$$\mathbf{c}_3(\psi) = \begin{cases} \mathbf{q}_{w,I}(f_I, \psi) & \psi_{I,1} \leq \psi \leq \psi_{I,2} & I \\ \mathbf{q}_{w,II}(f_{II}, \psi) & \psi_{II,1} < \psi \leq \psi_{II,2} & II \\ \mathbf{q}_{w,III}(f_{III}, \psi) & \psi_{III,1} < \psi \leq \psi_{III,2} & III \\ \mathbf{q}_{w,IV}(f_{IV}, \psi) & \psi_{IV,1} < \psi \leq \psi_{IV,2} & IV \\ \mathbf{q}_{w,VI}(f_{VI}, \psi) & \psi_{VI,1} < \psi \leq \psi_{VI,2} & VI \\ \mathbf{q}_{w,VII}(f_{VII}, \psi) & \psi_{VII,1} < \psi \leq \psi_{VII,2} & VII \\ \mathbf{q}_{w,VIII}(f_{VIII}, \psi) & \psi_{VIII,1} < \psi \leq \psi_{VIII,2} & VIII \end{cases}, \quad (5-19)$$

where  $\psi$  is the curve parameter and  $\mathbf{q}_w$  and  $f_i$  are functions like  $\mathbf{r}_w$  and  $g_i$ , respectively.

As it is noticed in Eqs. (5-14) and (5-19), closed form equations for all pieces of  $\mathbf{c}_2$  and  $\mathbf{c}_3$  are derived analytically where the lower and upper limits of the curve parameter of  $\mathbf{c}_2$  and  $\mathbf{c}_3$ ,  $\theta$  and  $\psi$ , are obtained numerically.

The curves  $C_{41}$ ,  $C_{42}$  and  $C_{43}$  in Fig. 5-8 are results of intersection between the rake plane, Eq. (5-8), and the peripheral surfaces of the workpiece,  $W_1$ ,  $W_2$  and  $W_3$  (Fig. 5-8)

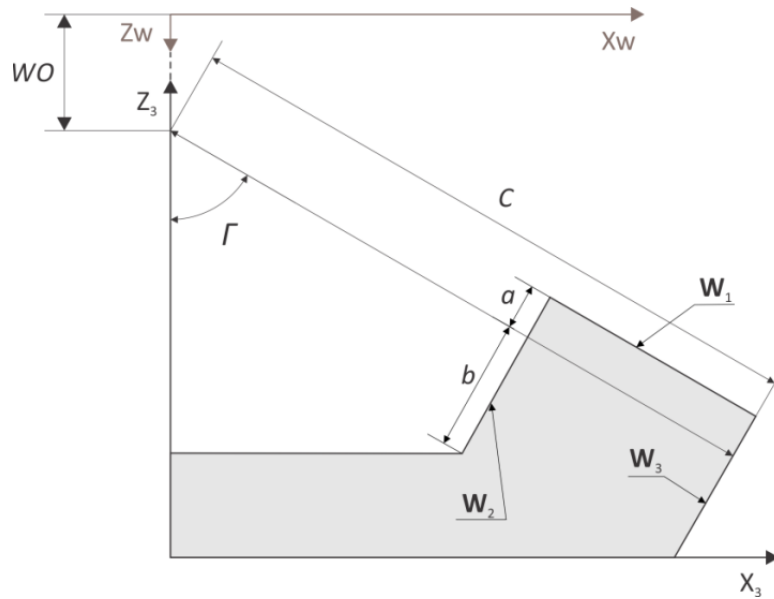


Fig. 5-8 Workpiece geometry.

Equations of the peripheral surfaces of the workpiece which are in contact with the cutting blades,  $W_1$ ,  $W_2$  and  $W_3$ , can be written as

$$\mathbf{W}_1(\varphi) = \begin{bmatrix} u \cdot \tan(\Gamma) \cdot \cos(\varphi) \\ u \cdot \tan(\Gamma) \cdot \sin(\varphi) \\ u + WO - \frac{a}{\sin(\Gamma)} \\ 1 \end{bmatrix}, \quad (5-20)$$

$$\mathbf{W}_2(\varphi) = \begin{bmatrix} u \cdot \cot(\Gamma) \cdot \cos(\varphi) \\ u \cdot \cot(\Gamma) \cdot \sin(\varphi) \\ C + \frac{a}{\tan(\Gamma)} \\ \frac{C + \frac{a}{\tan(\Gamma)}}{\cos(\Gamma)} + WO - \frac{a}{\sin(\Gamma)} - u \\ 1 \end{bmatrix}, \quad (5-21)$$

$$\mathbf{W}_3(\varphi) = \begin{bmatrix} u \cdot \cot(\Gamma) \cdot \cos(\varphi) \\ u \cdot \cot(\Gamma) \cdot \sin(\varphi) \\ \frac{C + \frac{a}{\tan(\Gamma)} - F}{\cos(\Gamma)} + WO - \frac{a}{\sin(\Gamma)} - u \\ 1 \end{bmatrix}, \quad (5-22)$$

respectively. By substituting the equations of  $\mathbf{W}_1$ ,  $\mathbf{W}_2$  and  $\mathbf{W}_3$  for  $\mathbf{P}$  in Eq. (5-8) and solving for  $u_1$ ,  $u_2$  and  $u_3$ , following equations are obtained

$$u_1 = \frac{\mathbf{V}_{bw} \cdot \mathbf{TT} \cdot [\sin(\Gamma), \sin(\Gamma), (-WO \cdot \sin(\Gamma) + a) / \pi z + \sin(\Gamma)]}{\sin(\Gamma) \cdot \mathbf{V}_{bw} \cdot [\tan(\Gamma) \cdot \cos(\varphi), \tan(\Gamma) \cdot \sin(\varphi), 1]}, \quad (5-23)$$

$$u_2 = \frac{\tan(\Gamma) \cdot \mathbf{V}_{bw} \cdot \mathbf{TT} \cdot [\cos(\Gamma), \cos(\Gamma), (-C - WO \cdot \cos(\Gamma)) / \pi z + \cos(\Gamma)]}{\mathbf{V}_{bw} \cdot [\cos(\Gamma) \cdot \cos(\varphi), \cos(\Gamma) \cdot \sin(\varphi), -\sin(\Gamma)]}, \quad (5-24)$$

$$u_3 = \frac{\tan(\Gamma) \cdot \mathbf{V}_{bw} \cdot \mathbf{TT} \cdot [\cos(\Gamma), \cos(\Gamma), (-C + F - WO \cdot \cos(\Gamma)) / \pi z + \cos(\Gamma)]}{\mathbf{V}_{bw} \cdot [\cos(\Gamma) \cdot \cos(\varphi), \cos(\Gamma) \cdot \sin(\varphi), -\sin(\Gamma)]}, \quad (5-25)$$


where  $\pi z$  is z-coordinate of the origin  $\mathbf{TT}$ . Equations of  $\mathbf{c}_{41}(\varphi)$ ,  $\mathbf{c}_{42}(\varphi)$  and  $\mathbf{c}_{43}(\varphi)$  are found by substituting  $u_1$ ,  $u_2$  and  $u_3$  for  $u$  in the equations of  $\mathbf{W}_1$ ,  $\mathbf{W}_2$  and  $\mathbf{W}_3$ , respectively. Based on the location of the outside blade of group  $n_b$ , or in other words the location of the rake face inside the workpiece, one or two peripheral surfaces are in contact with the rake face. Fig. 5-7 shows the dominant situation in face-hobbing when only the surface  $\mathbf{W}_1$  is crossed the rake plane. In this case,  $\mathbf{W}_1$  is the effective peripheral surface,  $\mathbf{W}_E$ , and  $\mathbf{C}_{41}$  is the effective peripheral intersection curve,  $\mathbf{C}_{4E}$ . However, two peripheral surfaces are engaged with the rake plane when the cutting blade begins penetrating the workpiece or leaving the workpiece. The intersection points between boundaries,  $\mathbf{p}_1$ ,  $\mathbf{p}_2$ ,  $\mathbf{p}_3$  and  $\mathbf{p}_4$  are obtained numerically. The surface area of  $Ch_p$  can be obtained easily using Green's Theorem. However, in order to find the area of the un-deformed chip, the varying cutting velocity along the cutting edge must be taken into consideration. In addition, the mechanistic model of cutting forces needs the differential area of undeformed chip geometry at any point on the engaging cutting edge. This concept is discussed in the following section.



### 5.3.2 Case study

In this section, the presented semi-analytical method is applied on one case study of non-generated face-hobbing of bevel gears. Table 5-1 The process parameters for case studies. lists the process parameters.

Table 5-1 The process parameters for case studies.

|                         | Case Study*   |
|-------------------------|---|
| Process Parameters      |  |
| $N_g$                   | 45  |
| <b>Gear Blank</b>       |   |
| $A$                     | 2.44 mm   |
| $D$                     | 9.952 mm  |
| $F$                     | 38 mm   |
| $C$                     | 144.57 mm   |
| $\Gamma$                | 76.05 deg   |
| <b>Cutting System</b>   |   |
| $h_f$                   | 12 mm   |
| $r_e$                   | 0.5 mm  |
| $L_t$                   | 10 mm   |
| $\rho$                  | 762 mm  |
| $\tau$                  | 10 deg  |
| $k_e$                   | 12 deg  |
| $\alpha_e$              | 20 deg  |
| $\eta_b$                | 4.42 deg  |
| $\gamma_2$              | 87 deg  |
| $\alpha_c$              | 3 deg   |
| $N_b$                   | 13  |
| $r_b$                   | 76 mm   |
| <b>Machine Settings</b> |   |
| $H$                     | 63.5206 mm  |
| $V_p$                   | 101.2954 mm   |
| $\Delta X_p$            | 1.07 mm   |
| $\gamma_m$              | 67.1114 deg   |
| $\omega_H$              | 400 rpm   |
| $A_x$                   | $-0.0184 \text{ mm} / \text{s}^2$   |
| $V_0$                   | $0.667 \text{ mm} / \text{s}$   |

\*Geometric parameters are computed using HYGEAR® software.

The maximum un-deformed chip area reaches  $0.8 \text{ mm}^2$  on the outside blade. Fig. 5-9 shows several examples of derived  $Ch_p$  during machining for different cutter head rotation angle,  $\theta$ , and corresponding un-deformed chip area,  $A_c$ .

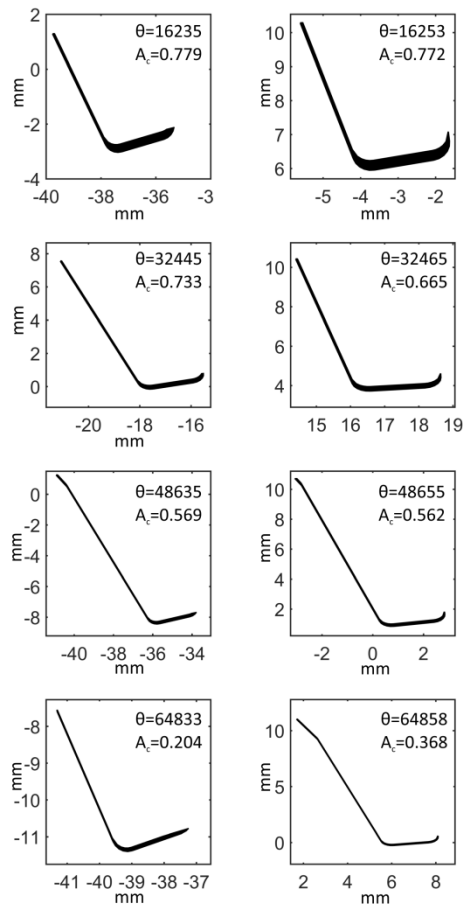


Fig. 5-9 Examples of obtained  $Ch_p$  for different  $\theta$  (deg) and corresponding un-deformed chip area,  $A_c$  ( $\text{mm}^2$ ).

# Chapter 6

## Cutting Force Prediction

### Citations:

- 1- Habibi, M., Chen, Z.C., 2016, “A Semi-analytical Approach to Un-deformed Chip Boundary Theory and Cutting Force Prediction in Face-hobbing”, *Computer Aided Design*, 73, pp. 53-65, doi: 10.1016/j.cad.2015.12.001.
- 2- Habibi, M., Chen, Z.C., 2015, “An Accurate and Efficient Approach to Un-deformed Chip Geometry in Face-hobbing and its Application in Cutting Force Prediction”, *ASME Journal of Mechanical Design*, 138(2):023302-023302-11, doi: 10.1115/1.4032090.

### 6.1 Cutting force calculation

In order to predict the cutting forces, un-deformed chip geometry should be obtained first. As it was mentioned,  $Ch_p$  is the projection of the undeformed chip geometry on the rake face of the cutting blade. The un-deformed chip geometry could be obtained by reverse projection of  $Ch_p$  on a plane perpendicular to the cutting velocity. However, since in face-hobbing, cutting velocity is changing along the cutting edge, the accurate un-deformed chip geometry could be obtained using the varying cutting velocity at each point along the cutting edge. To do so, the differential un-deformed chip area,  $dA$ , corresponding to  $P_e$  is derived, see Fig. 6-1.

The cutting velocity,  $V$ , at  $P_e$  is calculated. Plane  $p_v$  is created perpendicular to  $V$ . The differential un-deformed chip area is constructed on  $p_v$ . Curves  $C_{ip}(s)$  and  $C_{hp}(u)$  are projections of the cutting

edge curves,  $C_i(s)$ , and inside boundary of  $Ch_p$ ,  $C_h(u)$ , on  $p_v$  along  $V$ , respectively. Curve  $C_h(u)$  is created by passing a spline through points  $p'_1$  and  $p'_2$  (see Fig. 5-4). If the cutting velocity,  $V$ , was constant along the cutting edge, the area bounded by  $C_{ip}(s)$  and  $C_{hp}(u)$  would be the undeformed chip geometry. However, since  $V$  is changing, only in an infinitesimal vicinity of  $P_e$  ( $P_e = (P_{ex}, P_{ey}, P_{ez})$ ), the bounded area by  $C_{ip}(s)$  and  $C_{hp}(u)$ ,  $dA$ , represents the un-deformed chip area at  $P_e$ .

Based on the oblique cutting theory, the total differential cutting force at each point of the cutting edge can be decomposed to three force components. Directions of these three cutting force components can be written as

$$n_{tw} = -V/|V|, \quad (6-1)$$

$$n_{rw} = (M_M)^{-1} \begin{bmatrix} 1 & 0 & 0 & 0 \\ 0 & 1 & 0 & 0 \\ 0 & 0 & 0 & 0 \\ 0 & 0 & 0 & 1 \end{bmatrix} M_M (T_1/|T_1|), \quad (6-2)$$

$$n_{fw} = (n_{rw} \times n_{tw}) / |n_{rw} \times n_{tw}|, \quad (6-3)$$

where  $n_{tw}$ ,  $n_{rw}$  and  $n_{fw}$  are unit vectors in directions of the cutting velocity, normal and thrust at  $P_e$ , see Fig. 6-1.  $M_M$  is a transformation matrix used for the projection operation on  $p_v$ . Therefore,  $n_{rw}$  is the projection of  $T_1/|T_1|$  on  $p_v$ . In order to derive  $M_M$ , two rotation angles,  $\xi_1$  and  $\xi_2$ , are obtained using the cutting velocity,  $V = [V_x, V_y, V_z]^T$  as follows:

$$\xi_1 = \tan^{-1}(V_x/V_y), \quad (6-4)$$

$$T_2 = \begin{bmatrix} \cos(\xi_1) & -\sin(\xi_1) & 0 & 0 \\ \sin(\xi_1) & \cos(\xi_1) & 0 & 0 \\ 0 & 0 & 1 & 0 \\ 0 & 0 & 0 & 1 \end{bmatrix} V, \quad (6-5)$$

$$\xi_2 = \tan^{-1}(T_{2y}/T_{2z}), \quad (6-6)$$

where  $T_{2y}$  and  $T_{2z}$  are y and z components of vector  $T_2$ , respectively. Then, the equation of  $M_M$  can be written as

$$M_M = \begin{bmatrix} \cos(\xi_2) \cdot \cos(\xi_1) & -\cos(\xi_2) \cdot \sin(\xi_1) & \sin(\xi_2) & 0 \\ \sin(\xi_1) & \cos(\xi_1) & 0 & 0 \\ -\sin(\xi_2) \cdot \cos(\xi_1) & \sin(\xi_2) \cdot \sin(\xi_1) & \cos(\xi_2) & 0 \\ 0 & 0 & 0 & 1 \end{bmatrix}. \quad (6-7)$$

The formulation of un-deformed chip area,  $dA$ , can be written as

$$dA = t_h(s, u) \cdot ds_p(s), \quad (6-8)$$

where  $t_h$  and  $ds_p$  are the un-deformed chip thickness and the length of differential cutting edge element, respectively. As it can be seen in Fig. 6-1, one end of  $t_h$ ,  $P_{ep}$ , lies on the projection of the cutting edge,  $C_{ip}(s)$ , and the other end,  $P_h$ , lies on the projection of the inside boundary,  $C_{hp}(u)$ . The equation of  $C_{hp}(u)$  can be derived as

$$C_{hp}(u) = (M_M)^{-1} \begin{bmatrix} 1 & 0 & 0 & 0 \\ 0 & 1 & 0 & 0 \\ 0 & 0 & 0 & 0 \\ 0 & 0 & 0 & 1 \end{bmatrix} M_M C_h(u). \quad (6-9)$$

The intersection between  $C_{hp}(u)$  and a line with directional vector  $n_{fw}$  and passing through  $P_{ep}$ , is  $P_{hp}$ . The distance between  $P_{ep}$  and  $P_{hp}$  is the un-deformed chip thickness,  $t_h$ , at point  $P_e$  on the cutting edge.

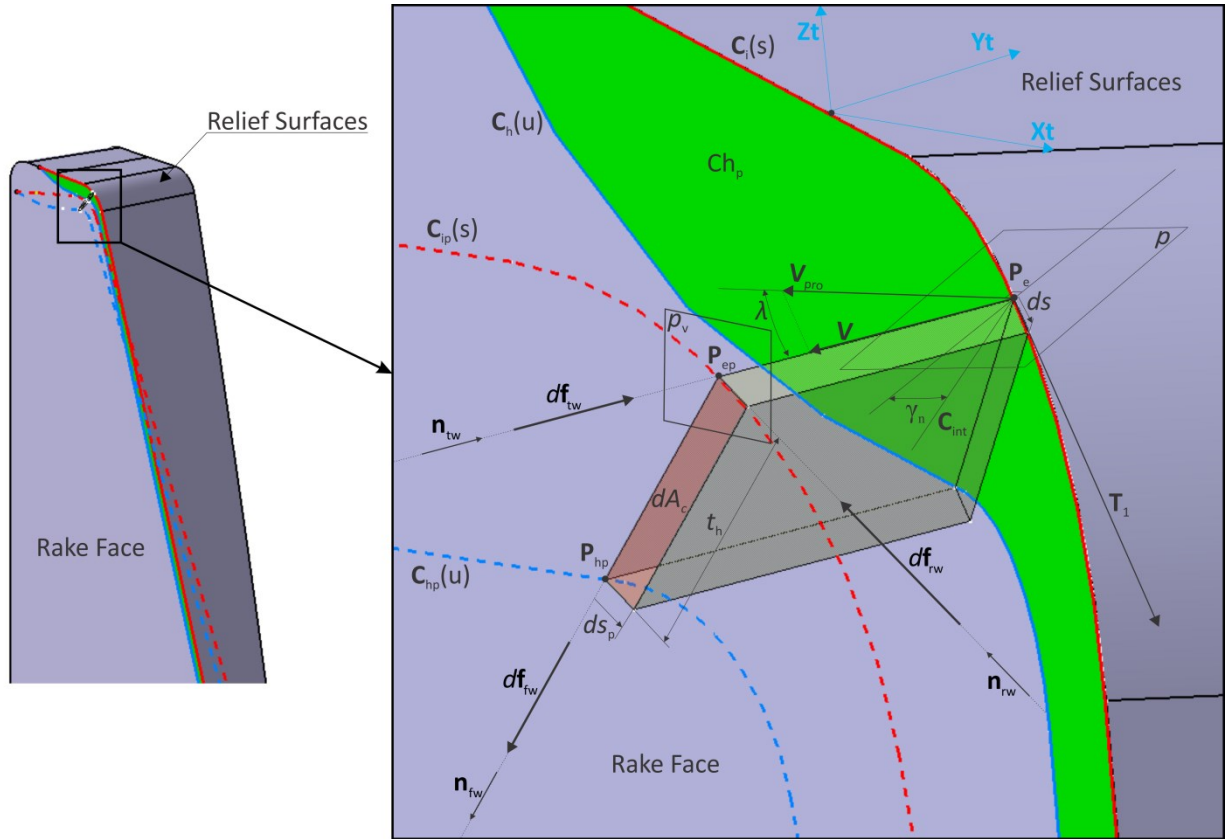


Fig. 6-1 Differential cutting force components.

Eventually, the three cutting force components,  $df_{tw}$ ,  $df_{rw}$  and  $df_{fw}$ , are estimated on  $dA$  (w in the subscripts shows that forces are formulated in the workpiece coordinate system,  $S_w$ ).

The cutting force components can be formulated as

$$df_{tw} = (K_{tc}(s) \cdot dA + K_{te}(s) \cdot ds) \cdot n_{tw}, \quad (6-10)$$

$$df_{rw} = (K_{rc}(s) \cdot dA + K_{re}(s) \cdot ds) \cdot n_{rw}, \quad (6-11)$$

$$df_{fw} = (K_{fc}(s) \cdot dA + K_{fe}(s) \cdot ds) \cdot n_{fw}, \quad (6-12)$$

where  $K_{tc}$ ,  $K_{rc}$  and  $K_{fc}$  are cutting force coefficients and  $K_{te}$ ,  $K_{re}$  and  $K_{fe}$  are edge cutting coefficients. The cutting force coefficients can be formulated as follows [15]:

$$K_{tc} = \frac{\tau_s}{\sin(\varphi_n)} \frac{\cos(\beta_n - \gamma_n) + \tan^2(\lambda) \cdot \sin(\beta_n)}{\sqrt{\cos^2(\varphi_n + \beta_n - \gamma_n) + \tan^2(\lambda) \cdot \sin^2(\beta_n)}}, \quad (6-13)$$

$$K_{rc} = \frac{\tau_s}{\sin(\varphi_n)} \frac{\cos(\beta_n - \gamma_n) \cdot \tan(\lambda) - \tan(\lambda) \cdot \sin(\beta_n)}{\sqrt{\cos^2(\varphi_n + \beta_n - \gamma_n) + \tan^2(\lambda) \cdot \sin^2(\beta_n)}}, \quad (6-14)$$

$$K_{fc} = \frac{\tau_s}{\sin(\varphi_n) \cdot \cos(\lambda)} \frac{\sin(\beta_n - \gamma_n)}{\sqrt{\cos^2(\varphi_n + \beta_n - \gamma_n) + \tan^2(\lambda) \cdot \sin^2(\beta_n)}}, \quad (6-15)$$

where  $\gamma_n$ ,  $\lambda$ ,  $\varphi_n$ ,  $\beta_n$ , and  $\tau_s$  are normal rake angle, inclination angle, normal shear angle, normal friction coefficient and shear yield stress, respectively. Eqs. (6-16) to (6-17) are formulated by taking some assumptions as: the orthogonal shear angle is equal to the normal shear angle, the normal rake angle is equal to orthogonal cutting rake angle, the chip flow angle is equal to the inclination angle and the friction coefficient and shear stress are the same in orthogonal and oblique cutting for a given machining condition. The functions of  $\varphi_n$ ,  $\beta_n$  and  $\tau_s$  are estimated in terms of  $\gamma_n$ ,  $\lambda$ , by set of orthogonal turning cutting tests. Then, the cutting force coefficients for oblique cutting is estimated by transforming orthogonal cutting parameters using Eq. (6-13) to Eq. (6-15). In face-hobbing,  $\gamma_n$  and  $\lambda$  vary along the cutting edge as it is shown in Fig. 4-4 and Fig. 4-5. Therefore, all the cutting force coefficients vary along the cutting edge too. Since,  $\gamma_n$  and  $\lambda$  depends on the geometry of the face-hobbing process (the geometry of cutting edge, cutter head and machine tool kinematic chains), the cutting force coefficients are process-dependent parameters. It means for each specific face-hobbing process which includes specific cutting system geometry, machine tool kinematics and machine settings, the cutting force coefficients are needed to be estimated using Eq. (6-13) to Eq. (6-15) by substituting values of  $\gamma_n$ ,  $\lambda$ .

The total cutting force,  $F_w$ , in the workpiece coordinate system,  $S_w$ , is derived by integrating the differential cutting forces along the cutting edge as follows:

$$F_w = \int_{s_1}^{s_2} (df_{tw} + df_{rw} + df_{fw}). \quad (6-18)$$

The upper and lower limits of the integration in Eq. (6-18),  $s_1$  and  $s_2$ , lie on the cutting edge and are chosen by comparing the corresponding cutting edge parameter,  $s$ , of the  $p_1$  and  $p_2$  points of the derived un-deformed chip geometry. The minimum and maximum of  $s$  are selected as  $s_1$  and  $s_2$ , respectively. In the present work, the total cutting forces are calculated by summing numerically the differential force components along the engaged cutting edge.

## **6.2 Case Studies using numerical un-deformed chip**

In this section, the proposed methods are applied on two case studies of non-generated face-hobbing of gears to obtain the workpiece in-process model, instantaneous un-deformed chip geometry and cutting forces during machining. The process parameters are listed in Table. 1.



Table 6-1 The process parameters for case studies.

| Process Parameters      | Case Studies |             |
|-------------------------|--------------|-------------|
|                         | I            | II*         |
| $N_g$                   | 45           | 52          |
| <b>Gear Blank</b>       |              |             |
| $A$                     | 2.44 mm      | 3.227 mm    |
| $D$                     | 9.952 mm     | 12.743 mm   |
| $F$                     | 38 mm        | 77 mm       |
| $C$                     | 144.57 mm    | 257.071 mm  |
| $\Gamma$                | 76.05 deg    | 73.9092 deg |
| <b>Cutting System</b>   |              |             |
| $h_f$                   | 12 mm        | 10.1 mm     |
| $r_e$                   | 0.5 mm       | 0.698 mm    |
| $L_t$                   | 10 mm        | 9 mm        |
| $\rho$                  | 762 mm       | 762 mm      |
| $\tau$                  | 10 deg       | 8 deg       |
| $k_e$                   | 12 deg       | 12 deg      |
| $\alpha_e$              | 20 deg       | 20 deg      |
| $\eta_b$                | 4.42 deg     | 4.42 deg    |
| $\gamma_2$              | 87 deg       | 87 deg      |
| $\alpha_c$              | 3 deg        | 3 deg       |
| $N_b$                   | 13           | 20          |
| $r_b$                   | 76 mm        | 190.5 mm    |
| <b>Machine settings</b> |              |             |
| $H$                     | 63.5206 mm   | 107.3771 mm |
| $V_p$                   | 101.2954 mm  | 156.0484 mm |
| $\Delta X_p$            | 1.07 mm      | -13.1208 mm |
| $\gamma_m$              | 67.1114 deg  | 73.9092 deg |
| $W_h$                   | 400 rpm      | 400 rpm     |

\*Parameters are computed using HYGEAR® software

The workpiece and cutting blade materials are selected as Ti<sub>6</sub>Al<sub>4</sub>V and tungsten carbide (WC), respectively. The orthogonal cutting parameters for the material combination of the workpiece and blade are given in [37] as

$$\left\{ \begin{array}{l} \tau_s = 613 \text{ Mpa} \\ \beta_n = 19.1 + 0.29\gamma_n \\ r_c = (1.755 - 0.028\gamma_n) \cdot L^{0.331 - 0.0082\gamma_n} \\ \varphi_n = \arctan\left(\frac{r_c \cdot \cos(\gamma_n)}{1 - r_c \cdot \sin(\gamma_n)}\right) \\ K_{te} = 24 \text{ N/mm} \\ K_{fe} = 43 \text{ N/mm} \\ K_{re} = 0 \end{array} \right. , \quad (6-19)$$

where  $r_c$  is the chip compression ratio.

### 6.2.1 Case study I

The in-process model of the gear workpiece is derived using the method proposed in Chapter 5. In Fig. 5-6, the in-process model of a disk is shown in different cutter head rotation angle. The continuous material removal behavior of the process is clearly illustrated in this figure. It is important to notice that all cutting blades, all 13 blade groups (26 blades), are considered to create the in-process model in Fig. 5-6.

Although, in order to obtain the in-process model, all the cutting blades should be considered, but in order to study the material removal behavior of the cutting blades, it is not necessary to predict cutting forces for all the cutting blades, only one blade group is enough. Therefore, the cutting forces for one blade group, one outside blade and one inside blade, are predicted. In addition, if the cutting forces are predicted while the specific blade group passes through a specific slot of the gear blank, the behavior and magnitude of cutting forces in machining other gear slots can be represented as well. Hence, the cutting forces are predicted for one specific blade group while passes through a specific gear slot.

The chosen blade group only 4 times (cycles a, b, c and d in Fig. 6-2. top left) passes through the same slot. The maximum chip area reaches  $0.9 \text{ mm}^2$  on the outside blade in the first cycle (cycle a). It is important to mention that in case I, the outside blade is mounted 2mm higher than inside blade on the cutter head. Therefore, having larger chip area on the outside blade is predictable. In case study II, the stick out of the cutting blades on the cutter head are equal.

The predicted total cutting forces are shown in Fig. 6-2. In order to validate the predicted cutting forces, the corresponding cutting forces are obtained using the commercial finite element machining software, Third Wave AdvantEdge®, for several sample locations of the outside and inside blades at different cutter head rotation angle,  $\theta$ . The workpiece and blade material are selected from the software library as Ti<sub>6</sub>Al<sub>4</sub>V and Carbide-Grade-P, respectively. The tool-workpiece material pair is the same as the material pair used to derive orthogonal cutting parameters (Eq. (6-19)). The selected blade locations, or cutter head rotation angles, are chosen in such a way that represents the shape of the cutting force diagrams properly in Fig. 6-2. Since, the complex blade path in space with respect to the workpiece coordinate system cannot be modeled in Third Wave®, therefore, at each selected location, the machining is assumed to be a straight cut. Hence, the workpiece is modeled using the geometry of derived  $Ch_p$  at each chosen location and the blade is mounted with respect to the workpiece using the corresponding average cutting velocity vector along the cutting edge.

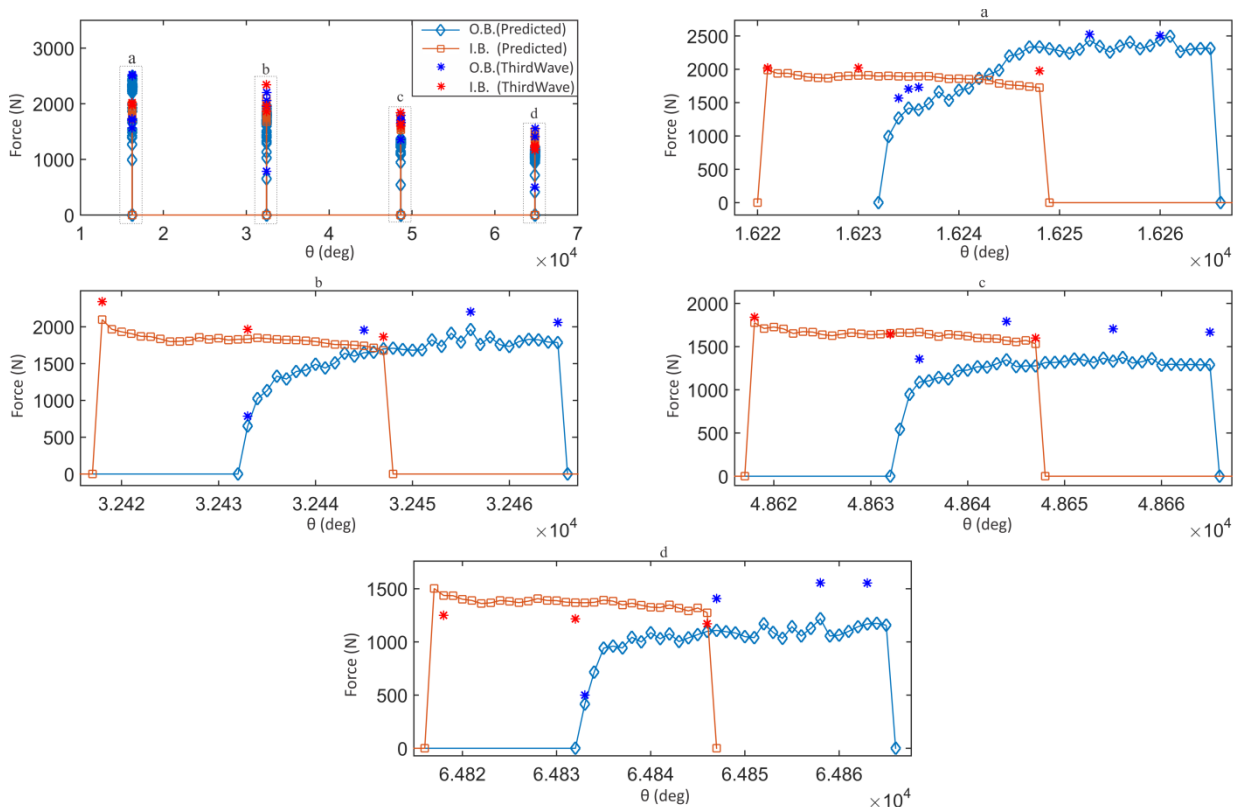


Fig. 6-2 Total cutting force estimated in the workpiece coordinate system in face-hobbing of case I for the outside, O.B. ( $n_b=1$ ) and inside, I.B. ( $n_b=13$ ) blades.

The predicted total cutting forces for the inside and outside blade has less than 11% and 30% error with respect to Third Wave® results, respectively. In feed direction, predicted cutting forces show less than 6% and 18% error for inside and outside blades, respectively. As it can be seen from Fig. 6-2, the predicted cutting forces for the outside blade has always more error in comparison with the inside blade. This can be explained as follows. First, the orthogonal cutting parameters in Eq. (6-19) were estimated for normal rake angles between 0 to 15 deg. However, in face-hobbing large negative normal rake angles happen especially at the tool tip and tool corner. Since, in the case study I for the outside blade  $\gamma_n \in (-35^\circ, 40^\circ)$ , the experimentally derived parameters in Eq. (6-19) do not cover completely the range of normal rake angle, therefore, the difference between the predicted and simulated forces in Fig. 6-2 could be explained. In addition, negative rake angle for the outside blade occur at the tool tip where the un-deformed chip thickness is larger than other region of the cutting edge. Hence, the cutting force generated at the tool tip is high enough to affect the total cutting forces due to the large negative rake angles.

### 6.2.2 Case study II

Fig. 6-3 shows the predicted total cutting forces for case study II. As it can be seen in this figure, the cutting forces of the inside blade is generally higher than the forces of the outside blade. In this case,  $\gamma_n \in (0^\circ, 30^\circ)$  and  $\gamma_n \in (-15^\circ, 15^\circ)$  for the outside and inside blades, respectively. Therefore, higher forces on the inside blade is predictable due to the negative rake angles along the cutting edge. Hence, the inside blade is more prone to be worn out due to the high generated cutting forces in comparison with the outside blade. This also confirms industrial reports which state the inside blade is worn out faster than the outside blade in Formate™ process.

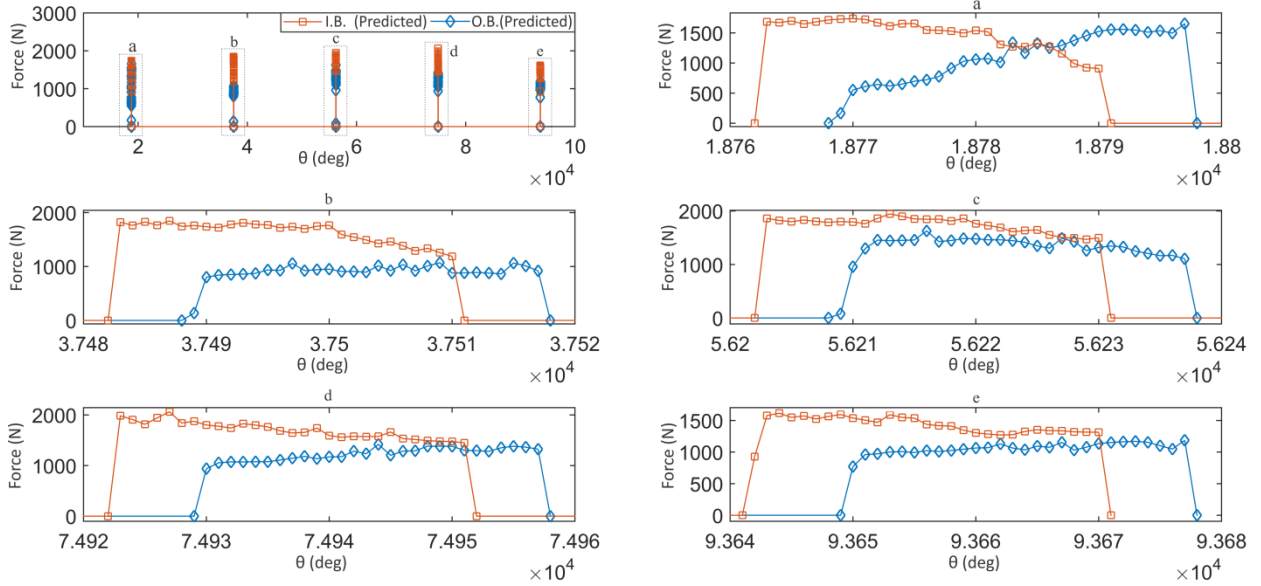


Fig. 6-3 Total cutting force estimated in the workpiece coordinate system in face-hobbing of case I for the outside, O.B. ( $n_b=1$ ) and inside, I.B. ( $n_b=20$ ) blades.

The un-deformed chip thickness and cutting force distributions along the cutting edge are shown in Fig. 6-4 at  $\theta=18784$  deg. The highlighted regions show the tool corner. These diagrams show that the un-deformed chip thickness and cutting force distribution (along  $x$  axis,  $W_x$ , along  $y$ ,  $W_y$ , along  $z$ ,  $W_z$  and total distribution,  $W$ ) along the cutting edge have very large gradients at the tool corner. These large gradients cause the local tool wear at the tool corner faster than other regions of the cutting edge.

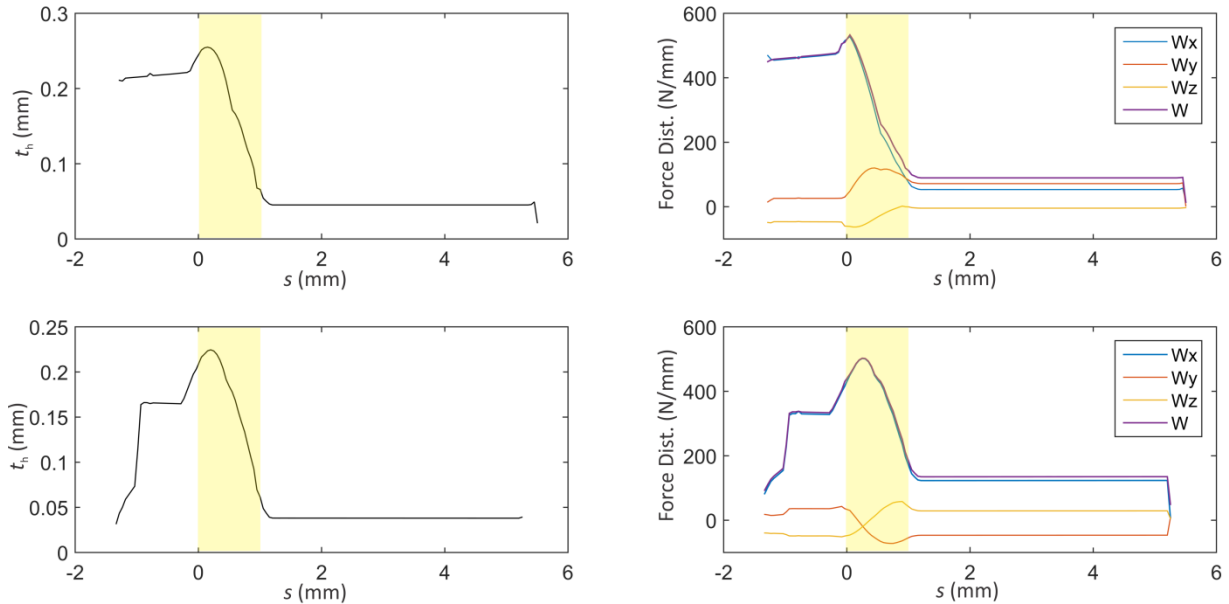


Fig. 6-4 The un-deformed chip thickness,  $t_h$ , and cutting force distribution along the cutting edge, Top (left and right): Outside blade and Bottom (left and right): Inside Blade.

### 6.3 Case Studies using semi-analytical un-deformed chip

In this section, the presented semi-analytical method is applied on two case studies of non-generated face-hobbing of bevel gears and the results are compared with numerical results of Section 6.2 (Habibi and Chen [18]). Table 6-1 lists the process parameters. The workpiece and cutting tool materials are chosen as  $Ti_6Al_4V$  and tungsten carbide (WC), respectively.

#### 6.3.1 Case study I

Fig. 6-5 shows the predicted total cutting forces for case study I by semi-analytical method (present work), numerical method from Section 6.3.1 (Habibi and Chen [18]) and finite element analysis. The chosen outside blade passes through the same slot only four times (cycles a, b, c and d in Fig. 6-5. top).

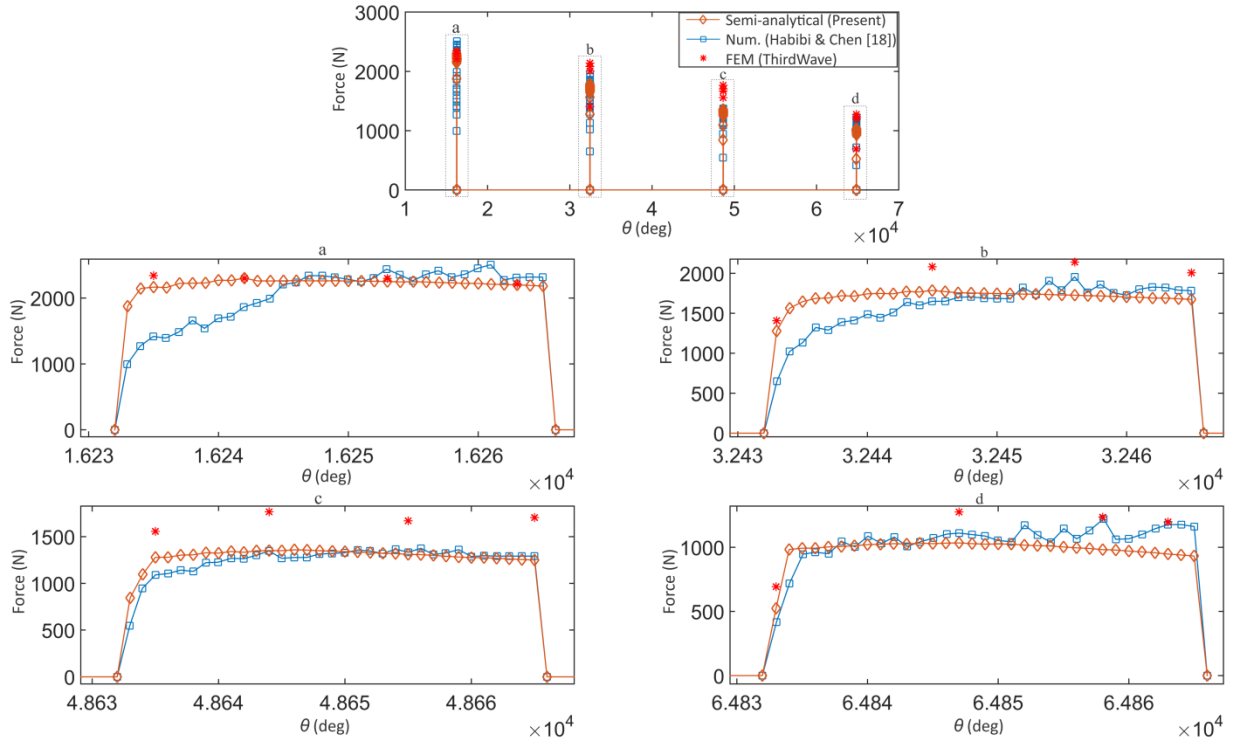


Fig. 6-5 Total cutting force estimated in the workpiece coordinate system in face-hobbing of case I for the outside blade ( $n_b=1$ ).

In order to validate the predicted cutting forces, the corresponding cutting forces are obtained using the commercial finite element machining software, Third Wave AdvantEdge®, for several sample locations of the blade at different cutter head rotation angles,  $\theta$ . The workpiece and blade material are selected from the software library as  $Ti_6Al_4V$  and Carbide-Grade-P, respectively. Maximum and minimum element sizes for the tool are assigned to 1mm and 0.03mm, respectively. Minimum element size is assigned to the cutting edge. Minimum chip element is set to 0.01mm and initial temperature is 20 °C. The workpiece and tool CAD models are modeled in CATIA™ and then, STEP models of them are imported in Third Wave®. When STEP models of the tool and workpiece are imported to the software, it requires assigning boundary conditions on both models. All nodes on the assigned boundary surfaces are fixed. In the simulations, the back face of the cutter and peripheral surfaces of the workpiece which are not engaged in the cutting process are set as boundaries.

The tool-workpiece material pair is the same as the material pair used to derive orthogonal cutting parameters (Eq. (6-19)). The selected blade locations, or cutter head rotation angles, are

chosen in such a way that represents the shape of the cutting force diagrams properly in Fig. 6-5. Since the complex blade path in space with respect to the workpiece coordinate system cannot be modeled in ThirdWave®, therefore, the machining is assumed to be a straight cut at each selected location. Thus, the workpiece is modeled using the geometry of derived  $Ch_p$  at each chosen location, and the blade is mounted with respect to the workpiece using the corresponding average cutting velocity vector along the cutting edge. Fig. 6-6 shows an example of conducted FE analysis at  $\theta=16235$  deg.

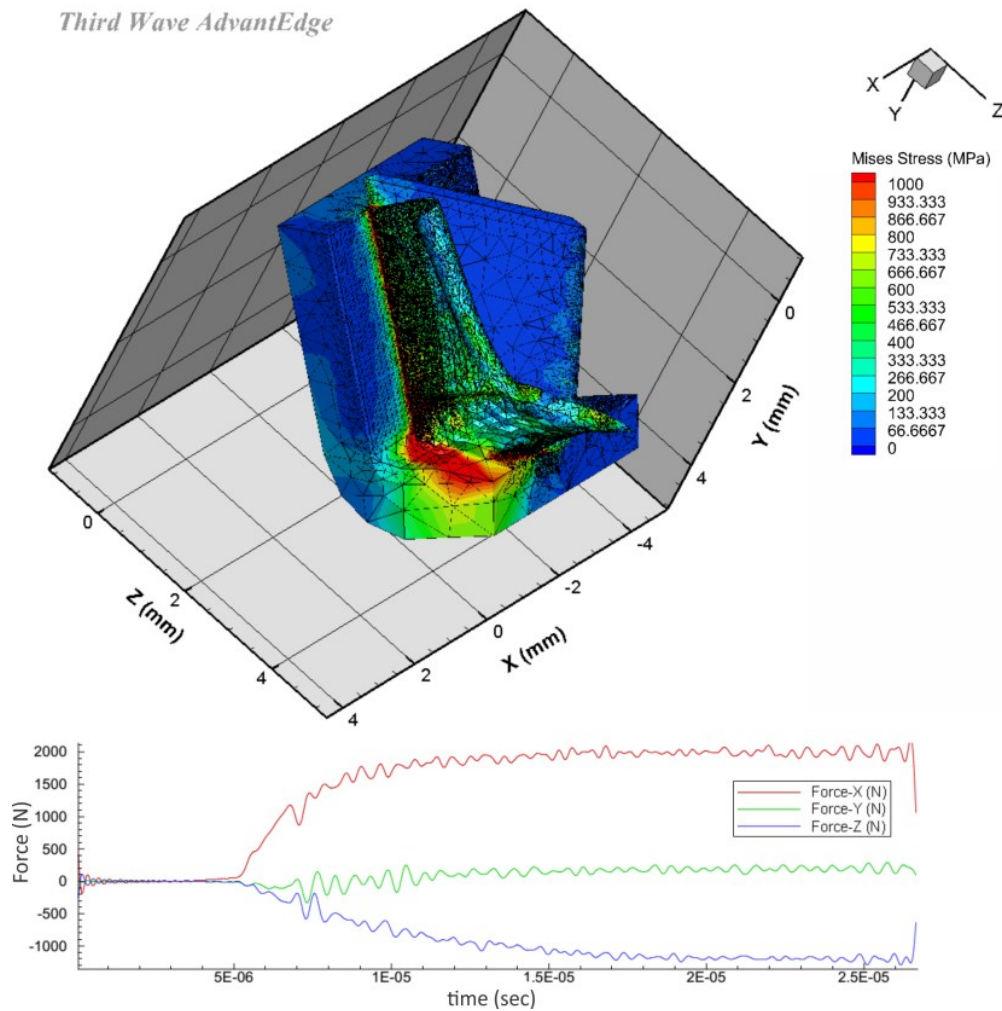


Fig. 6-6 An example of FE analysis (top) and obtained cutting forces (bottom).

The predicted total cutting forces and Third Wave® results have less than 21% difference. The predicted cutting forces, in feed direction, show less than 11% difference. The semi-analytical



cutting force results are in good agreement with numerical results from Habibi and Chen [18]. However, the obtained chip is more accurate in the semi-analytical approach than the numerical method. In some locations, the numerical method overestimate, as in  $\theta=64858$  deg (Fig. 6-5. d), or underestimate, as in  $\theta=16240$  deg (Fig. 6-5. a). If the workpiece is discretized by a finer step size, the numerical results converge to semi-analytic results theoretically.

### 6.3.2 Case study II

Fig. 6-7 shows the predicted total cutting forces for case study II. The semi-analytical results are in good agreement with numerical results in Section 6.2.2 (Habibi and Chen [18]).

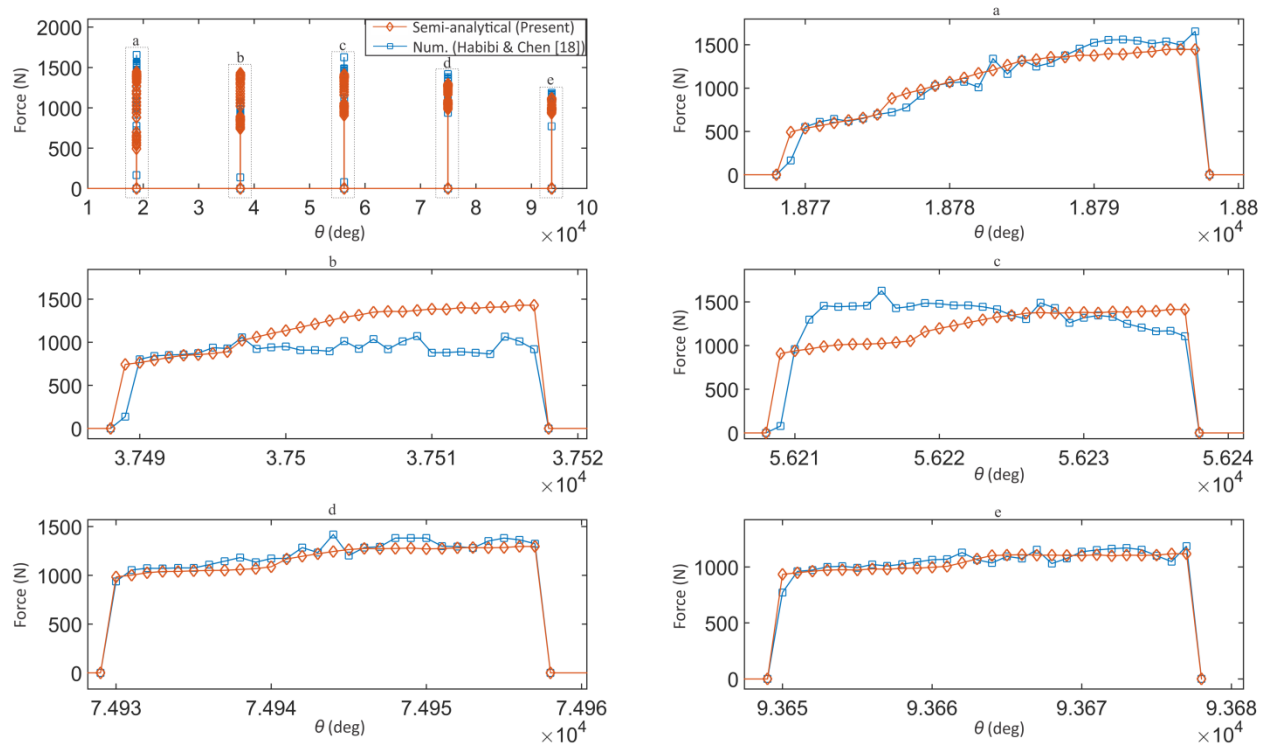


Fig. 6-7 Total cutting force estimated in the workpiece coordinate system in face-hobbing of case II for the outside blade ( $n_b=1$ ).

The un-deformed chip thickness and cutting force distributions are shown in Fig. 6-8 at  $\theta=18784$  deg along the cutting edge. The highlighted areas show the regions that the tool is going to be worn out faster than the other regions. The values of cutting force distributions along  $x, y, z$  ( $W_x,$

$W_y$  and  $W_z$ , respectively) and total distribution,  $W$ , as well as the chip thickness vary sharply in these regions. These results are in agreement with practical wear cases happened in gear manufacturing industries that the tool corner wears faster than other regions of the cutting edge.

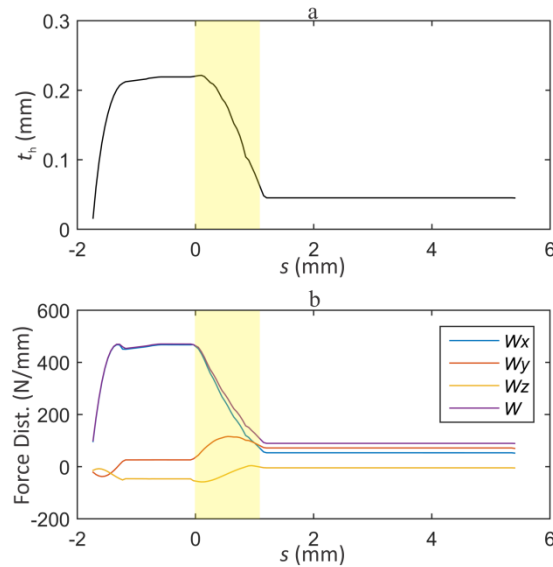


Fig. 6-8 (a) Un-deformed chip thickness,  $t_h$ , (b) Cutting force distribution along the cutting edge.

## 6.4 Conclusion

In the present work, using the proposed methods, the workpiece in-process model and the instantaneous un-deformed chip geometry are derived and the cutting forces are predicted in face-hobbing of bevel gear for the first time in the state of art of bevel gear manufacturing. In order to derive the un-deformed chip geometry, first, the workpiece in-process model is obtained by discretizing the workpiece into disks and intersecting the blades with the disks. Then, the projection of the un-deformed chip geometry is obtained on the rake face of the blades. At each point on the cutting edge, the un-deformed chip geometry at an infinitesimal vicinity of the point is obtained using the obtained projection and the cutting velocity vector along the cutting edge. Face-hobbing is converted geometrically along the cutting edge of the blades into many small oblique cuts. The differential cutting forces, for each cut, are formulated at each point on the cutting edge using oblique cutting theory. Normal rake, inclination angles and the un-deformed chip thickness are derived at each point on the cutting edge at each moment of face-hobbing

machining and plugged into cutting force formulations. The chosen orthogonal cutting parameters are assumed to be in terms of normal rake angle and un-deformed chip thickness.

Gleason TRI-AC® cutting system is chosen and the methods are applied on two case studies on non-generated (Formate®) process. For the first case study, the predicted cutting forces are compared with the obtained cutting forces using a commercial finite element machining software, Third Wave AdvantEdge®. The comparison shows less than 30% difference between the predicted total cutting forces and the results of Third Wave®. In addition, using the obtained cutting force distribution along the cutting edge, regions of the local tool wear can be predicted.

The present work opens new doors for future studies on the cutting system design for face-hobbing of bevel gears based on cutting force prediction methods, in order to predict and prevent the tool wear. In addition, the machining settings such as feed rates and cutter head rotary speed can be estimated and optimized prior real machining based on the predicted cutting forces. Moreover, the simulation of generated face-hobbing could be the topic for further studies since the present work was conducted on non-generated process. The basics are the same but the cutting surfaces are more complicated than the non-generated process.

## Chapter 7

# Machining Parameters Optimization based on Cutting Force and Tool Wear Constraints

**Citation:** Habibi, M., Chen, Z.C., 2016, “Machining Setting Optimization for Formate® Face-hobbing of Bevel Gears with the Tool Wear Constraint”, *ASME Journal of Mechanical Design*, Submitted.

### 7.1 Introduction

Trial and error experiments and computationally expensive FEM analysis are the main trends in cutting tool design and machining setting selection in face-hobbing of bevel gear in industries. The present paper introduces a new approach to machining setting selection based on a computationally inexpensive semi-analytical method considering cutting forces and tool wear in non-generated face-hobbing.

In the present chapter, in order to find appropriate values for machining settings in non-generated face-hobbing (cutter head rotary speed, plunge function and time), an optimization problem is constructed to minimize the machining time subject to some constraints originated in the tool wear model. There are suggested values for crater or flank wear depth which indicate the tool life [16]. In this paper crater, wear is studied. Therefore, the constraint restricts the maximum crater

wear in all face-hobbing scenarios. Among all scenarios, one which gives the minimum machining time with the allowable tool wear is the solution for the optimization problem.

Tool wear has been always one of the main concerns of machining industries. From classic Taylor's tool life equation to much more advanced formulation such as Usui's wear rate model [16], tool wear or wear rate models have been always one of the hottest topics for researcher ([54], [55], [56], [57], [58], [59] and [60]) in machining areas. Tool wear is a complex phenomenon involving abrasive, adhesive and chemical mechanisms. However, by developing cutting material and coating techniques, most researchers focused on adhesion and abrasion oriented wear models [60]. Among wear rate models, Usui's model has been taken a lot of attentions in recent years due to its comprehensive formulation of the wear phenomenon on the rake and relief surfaces of the tools ([55], [56] and [60]). In the present paper, this model is implemented in face-hobbing and the tool wear rate is calculated along the cutting edge at any time instant during face-hobbing. Most researchers used Usui's model by FEM methods to predict the tool wear on rake or relief faces of the tools on turning operations. However, FEM methods are computationally expensive and specially are not practical in order to solve the optimization problem for the present work, since many machining scenarios must be simulated to reach to a feasible and optimum solution. Therefore, a semi-analytical approach to the tool wear rate model is taken into consideration in the present chapter.

In the proposed semi-analytical method, the cutting edge of the cutting blade in Formate® face-hobbing is converted into many small oblique cuts along the cutting edge of the blades. For each infinitesimal oblique cutting element, cutting forces, average interface temperature, average normal stress and chip sliding velocity are calculated semi-analytically. Since average values of the interface temperature and normal stress are calculated, the wear rate model gives the average wear rate values along the cutting edge. The average values of the wear rate does not affect the solution of the optimization problem since the behavior of the maximum wear rate with respect to machining setting changes is similar to behavior of the average wear rate. This concept will be discussed in Sec. 3 with experimental results retrieved from research papers.

In order to simulate each face-hobbing scenario in the optimization problem, methods developed Chapters 5 and 6 are implemented to simulate kinematic chains of the non-generated face-hobbing, obtained the un-deformed chip geometry semi-analytically and predict cutting forces. The term "face hobbing scenario" means each set of machining settings that creates a face-

hobbing scenario in which the tool wear should be predicted for. For example, if machining settings of a Formate® face-hobbing process are: plunge time,  $t_p=10s$ , cutter head rotary velocity,  $\omega=400RPM$ , cutter head velocity function= linear, then , these parameters represent a machining scenario in face-hobbing. The tool wear is predicted for this face-hobbing scenario and is compared with other machining scenarios to reach to an optimal scenario which has minimum plunge time and allowable wear.

In the present chapter, kinematics of face-hobbing, un-deformed chip geometry and cutting forces are discussed briefly in Section. 7.2. In Section 7.3, Usui' wear rate model is described and validated and all the contributing parameters in the wear rate model formula are derived analytically or semi-analytically for face-hobbing. In Section 7.4, the optimization problem for face-hobbing is constructed to estimate appropriate machining settings. Two practical case studies are examined in Section 7.5 to show the capability of the proposed method to select appropriate machining settings.

## **7.2 Face-hobbing simulation**

In order to implement optimization problems to derive appropriate machining settings, face-hobbing needs to be simulated computationally efficiently. One of the most important characteristics of face-hobbing simulation is predicted cutting forces. To estimate cutting forces, un-deformed chip geometry should be obtained. In order to do so, kinematic chain of the process should be defined. In the following, each procedure is described briefly.

### **7.2.1 Kinematic chains**

Face-hobbing cutting system consists of a cutter head and a specific number ( $N_b$ ) of cutting blades mounted in cutter head slots. In case of half profile cutting blades, one outside and one inside blade create a blade group. The cutter head and the workpiece rotate proportionally and cutter head approached the workpiece (plunge motion) as shown in Fig. 7-1. During the plunge motion, the cutting blades are engaged with the workpiece and removes material from it. When the offset of the cutter head to  $XmYm$  plane,  $BO$ , reaches zero, the plunge motion stops and the cutter head rotates  $N_g$  times to finish the gear teeth surfaces.

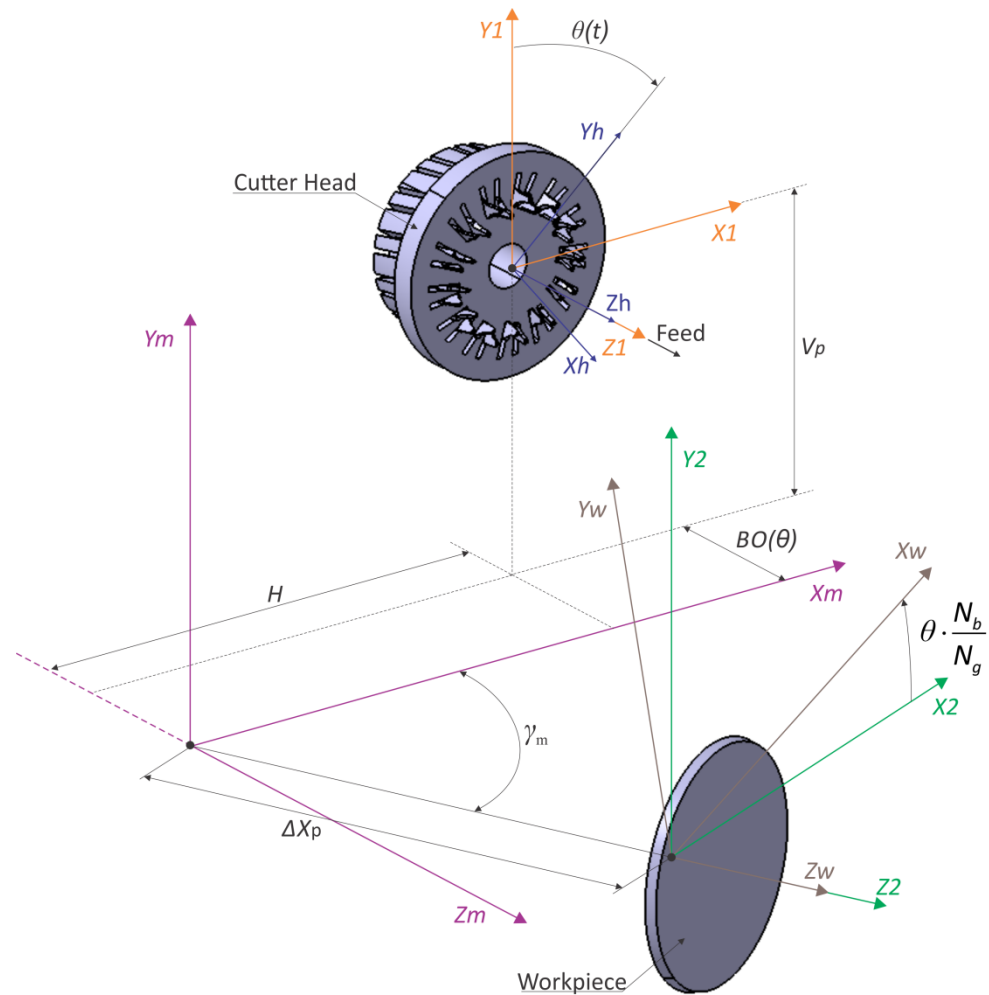


Fig. 7-1 Non-generated (Formate®) face-hobbing kinematics.

### 7.2.2 Un-deformed chip geometry and cutting force prediction

The projection of the un-deformed chip geometry on the rake face,  $Ch_p$ , can be obtained using the semi-analytic boundary theory provided in Chapter 5. The cutting edge and derived  $Ch_p$  is discretized into many small cutting elements which each of them represents an oblique cut. In other words, face-hobbing is converted into many infinitesimal oblique cuts. The cutting forces for each differential element are calculated and the summed together to obtain the total cutting forces as described in Chapter 6. The cutting forces play an important role in tool wear rate calculation since the normal stress along the cutting edge is obtained using the differential cutting forces.

### 7.3 Wear rate model

In the present paper, in order to predict calculate the wear rate, Usui' wear rate model [16] is implemented in the optimization problems. The Usui's model is formulated as

$$\dot{w} = \frac{dw}{dt} = A \cdot \sigma_n \cdot V_s \cdot e^{\left(\frac{-B}{T_{int}}\right)}, \quad (7-1)$$

Where  $w$  volume loss per unit area,  $\dot{w}$  is volume loss per unit area per unit time,  $\sigma_n$  is normal stress,  $V_s$  is the chip sliding velocity relative to the workpiece,  $T_{int}$  is the interface temperature and,  $A$  and  $B$  are constants for given workpiece and cutting tool materials. In order to have a good prediction of wear rate,  $\dot{w}$ , on the rake or relief faces of the tool,  $V_s$ ,  $\sigma_n$  and  $T_{int}$  should be estimated accurately. In the present paper, for each differential oblique cut element, average wear rate,  $\dot{w}$ , is calculated by substituting average normal stress,  $\bar{\sigma}_n$ , and interface temperature,  $\bar{T}_{int}$  ( $\dot{w} = A \cdot \bar{\sigma}_n \cdot V_s \cdot e^{\left(\frac{-B}{\bar{T}_{int}}\right)}$ ). In the following,  $V_s$ ,  $\bar{\sigma}_n$  and  $\bar{T}_{int}$  are derived in face-hobbing along the cutting edge.

#### 7.3.1 Chip sliding velocity, $V_s$

In order to calculate the chip sliding velocity, first, the cutting velocity,  $\mathbf{V}$ , for any point along the cutting edge with respect to the workpiece coordinate system need to be derived in face-hobbing. Therefore, the cutting velocity,  $\mathbf{V}$ , can be written as

$$\mathbf{V} = \frac{\partial \mathbf{r}_w(s, \theta)}{\partial \theta} \cdot \frac{d\theta}{dt}, \quad (7-2)$$

where  $\mathbf{r}_w$  is the equation of the cutting surfaces in the workpiece coordinate system and  $\frac{d\theta}{dt}$  represents the angular velocity of the cutting system. In oblique cutting theory, the chip velocity is derived by



$$V_c = \frac{V \cdot \cos(\lambda_s) \cdot \sin(\varphi_n)}{\cos(\eta_c) \cdot \cos(\varphi_n - \gamma_n)}, \quad (7-3)$$

where  $\eta_c$  and  $\lambda_s$  are chip flow angle and inclination angle, respectively. In face-hobbing  $V_s=V_c$ . In order to use Eq. (7-3) a few assumptions are made as follows: chip flow angle is equal to inclination angle ( $\eta_c = \lambda_s$ ); normal shear angle is equal to orthogonal shear angle ( $\varphi_n = \varphi_c$ ); normal rake angle is equal to orthogonal rake angle ( $\gamma_n = \gamma_c$ ) and finally, chip flow angle is equal to inclination ( $\eta_c = \lambda_s$ ). The equation of  $\varphi_n$  are estimated experimentally by conducting several orthogonal turning test and measuring cutting forces and using orthogonal cutting theory for a specific material pair of workpiece and cutting tool.

### 7.3.2 Average normal stress, $\bar{\sigma}_n$

Average normal stress on the rake face,  $\bar{\sigma}_n$ , for each oblique cut element along the cutting edge is calculated as

$$\bar{\sigma}_n = \frac{F \cdot \cos(\beta_o)}{A_t}, \quad (7-4)$$

where  $F$ ,  $\beta_o$  and  $A_t$  are total cutting force, average friction angle, and chip contact area with the rake face, respectively. The total force,  $F$ , for each individual oblique cutting element is calculated in Chapter 6. The equation of  $\beta_o$  is estimated by orthogonal cutting experiments. The equation of  $A_t$  in oblique cutting can be written as

$$A_t = ds \cdot l_t, \quad (7-5)$$

where  $l_t$  can be written as [61]

$$l_t = \frac{t_h}{\sin(\varphi_n) \cdot \cos(\eta_c)} \left( \sin(\varphi_n - \gamma_n) + \tan(\lambda_s) \cdot \cos(\varphi_n - \gamma_n) \cdot \cos(\eta_c) \right), \quad (7-6)$$

where  $t_h$  is un-deformed chip thickness.

### 7.3.3 Average interface temperature, $\bar{T}_{int}$

The equation for average interface temperature,  $\bar{T}_{int}$ , from orthogonal cutting theory can be written as [37]

$$\bar{T}_{int} = T_s + \lambda_{int} \cdot \Delta T_m, \quad (7-7)$$

Where  $T_s$  is the average shear plane temperature,  $\lambda_{int}$  is an empirical correction factor ( $\lambda_{int} = 0.7$ ) and  $\Delta T_m$  is the maximum temperature rise at the interface between deformed chip and the rake face which can be written as the following empirical equation [37]

$$\Delta T_m = \Delta T_c \cdot 10^{\left(0.06 - 0.195 \cdot \delta \cdot \sqrt{\frac{R_T \cdot t_c}{l_t}} + 0.5 \cdot \log\left(\frac{R_T \cdot t_c}{l_t}\right)\right)}, \quad (7-8)$$

where  $\Delta T_c$  is the average temperature rise in the chip and  $\delta = 0.1 t_c$ .  $t_c$  is the deformed chip thickness and its equations can be written as

$$t_n = t_c / r_c, \quad (7-9)$$

where

$$r_c = \frac{\tan(\varphi_n)}{\left(\frac{\cos(\eta_c)}{\cos(\lambda)}\right) \cdot (\cos(\gamma_n) + \tan(\varphi_n) \sin(\gamma_n))}. \quad (7-10)$$

$R_T$  is a nondimensional thermal value and can be written as

$$R_T(\bar{T}_{int}) = \frac{\rho(\bar{T}_{int}) \cdot c_s(\bar{T}_{int}) \cdot V \cdot t_h}{c_t(\bar{T}_{int})}, \quad (7-11)$$

where  $\rho$ ,  $c_s$  and  $c_t$  are density, specific heat coefficient and thermal conductivity of the workpiece material. The temperature dependent material properties of AISI 1045 [62] are listed in Table 7-1 AISI 1045 material properties..

Table 7-1 AISI 1045 material properties.

| Property                                  | Temperature Range      | Functions [62]   |
|---|------------------------|--|
| Density, $\rho$ (kg/m <sup>3</sup> )      | T > 1041K<br>T < 985 K | $\rho = 8190 - 0.49T$<br>$\rho = 7919.7 - 0.2149T - 0.000102T^2$ |
| specific heat coefficient, $c_s$ (J/kg·K) | T > 1041K<br>T < 873 K | $c_s = 439 - 0.1142T$<br>$c_s = 447 + 0.081T + 0.000495T^2$      |
| thermal conductivity, $c_t$ (W/m·K)       | T > 1073K<br>T < 973 K | $c_t = 295.36 - 0.4382T + 0.0002T^2$<br>$c_t = 51.638 - 0.0228T$ |

The equation of  $\Delta T_c$  is obtained from friction power consumed at the tool-chip interface.

Therefore, the formula of  $\Delta T_c$  can be written as

$$\Delta T_c = \frac{P_u}{m_c \cdot c_s}, \quad (7-12)$$

where  $P_u$  is the friction power on the tool-chip interface,  $m_c$  is metal removal rate ( $m_c = dA_c \cdot V \cdot \rho(\bar{T}_{int})$ ). The Friction power at the tool-chip interface,  $P_u$ , is calculated as

$$P_u = F_u \cdot V_c, \quad (7-13)$$

where  $F_u$  is the friction force component on the rake face and can be written as

$$F_u = F \cdot \sin(\beta_o). \quad (7-14)$$

The average shear plane temperature,  $T_s$ , is formulated using and an empirical equation [37] as

$$T_s = T_r + 0.7 \cdot (1 - \varepsilon_s) \cdot \frac{P_s}{m_c \cdot c_s}, \quad (7-15)$$

where

$$\begin{aligned} \varepsilon_s &= 0.5 - 0.35 \cdot \log(R_r \cdot \tan(\varphi_c)), & 0.04 \leq R_r \cdot \tan(\varphi_c) \leq 10 \\ \varepsilon_s &= 0.3 - 0.15 \cdot \log(R_r \cdot \tan(\varphi_c)), & R_r \cdot \tan(\varphi_c) > 10 \end{aligned} \quad (7-16)$$

$$P_s = F_s \cdot V_s, \quad (7-17)$$

$$V_s = \frac{V \cdot \cos(\gamma_n)}{\cos(\phi_n - \gamma_n)}, \quad (7-18)$$

where  $P_s$  is the shear power in the shear plane,  $V_s$  is the shear velocity and  $T_r$  is ambient temperature. After substituting the required parameters in Eq. (7-7), this equation is converted to a non-linear equation with one variable as

$$\bar{T}_{int} = g(\bar{T}_{int}), \quad (7-19)$$

where  $g$  is a non-linear function. Solving Eq. (7-19) gives the average tool-chip interface temperature,  $\bar{T}_{int}$ .

### 7.1.1 Validation

In order to validate the interface temperature prediction formulation, for several orthogonal cutting test the predicted results are compared with experimental test and measured temperatures as listed in Table 7-2. It can be seen in Table 7-2 that the predicted average interface temperature,  $\bar{T}_{int}$ , is in good agreement with experimental and finite element results ( $T_{int}^{max}$ ). Since the predicted temperature is the average value,  $\bar{T}_{int}$  is always lower than the measured values,  $T_{int}^{max}$  which is the maximum interface temperature. However,  $\bar{T}_{int}$  shows the behavior of the interface temperature change accurately with respect to machining settings.

Table 7-2 Comparison of analytical predicted temperature with finite element and experimental results.

| Test | V<br>(m/min) | t <sub>h</sub><br>(mm) | γ <sub>n</sub><br>(deg) | ds <sub>p</sub><br>(mm) | T <sub>int</sub> <sup>max</sup> (°C)<br>(measured [63], [64], [65] and [66]) | T <sub>int</sub> <sup>max</sup> (°C)<br>(FEM [62]) | T̄ <sub>int</sub> (°C)<br>(present work) |
|------|--------------|------------------------|-------------------------|-------------------------|--|--|--|
| 1    | 200          | 0.15                   | 5                       | 1.6                     | 1250   | 1080   | 947                                      |
| 2    | 300          | 0.15                   | 5                       | 1.6                     | 1300   | 1198   | 1010                                     |
| 3    | 200          | 0.15                   | -7                      | 1.6                     | 1120   | 1109   | 1016                                     |
| 4    | 300          | 0.15                   | -7                      | 1.6                     | 1310   | 1250   | 1032                                     |
| 5    | 200          | 0.3                    | 5                       | 1.6                     | 1220   | 1171   | 1133                                     |
| 6    | 300          | 0.3                    | 5                       | 1.6                     | 1300   | 1281   | 1177                                     |
| 7    | 200          | 0.3                    | -7                      | 1.6                     | 1100   | 1192   | 1179                                     |
| 8    | 300          | 0.3                    | -7                      | 1.6                     | 1305   | 1326   | 1205                                     |
| 9    | 198          | 0.1                    | 0                       | 2.5                     | -  | 1037   | 979                                      |
| 10   | 399          | 0.1                    | 0                       | 2.5                     | -  | 1307   | 1117                                     |
| 11   | 628          | 0.1                    | 0                       | 2.5                     | -  | 1351   | 1218                                     |
| 12   | 879          | 0.1                    | 0                       | 2.5                     | -  | 1396   | 1316                                     |

In order to validate the wear rate model, two sets of experimental tests are considered, crater depth and wear volume measurements. In the first set of experiments, in order to measure crater wear at different machining time, a set of turning operations are conducted and the crater depth is measured. The results of the experiments are shown in Fig. 7-2. Left. Corresponding average crater depth,  $\overline{KT}$ , is predicted as

$$\overline{KT} = t_m \cdot \dot{w}, \quad (7-20)$$

where t<sub>m</sub> is machining time. In Eq. (7-20), it is assumed that the wear rate is constant during machining which approximately linear slopes of experimental results in Fig. 7-2. Left confirms this assumption. The results of Eq. (7-20) are plotted in Fig. 7-2. Right. As it can be seen in Fig. 7-2, although predicted values are lower than the measurements, the predicted average crater

depth simulates the behavior of the actual crater wear depth accurately with respect to machining settings.

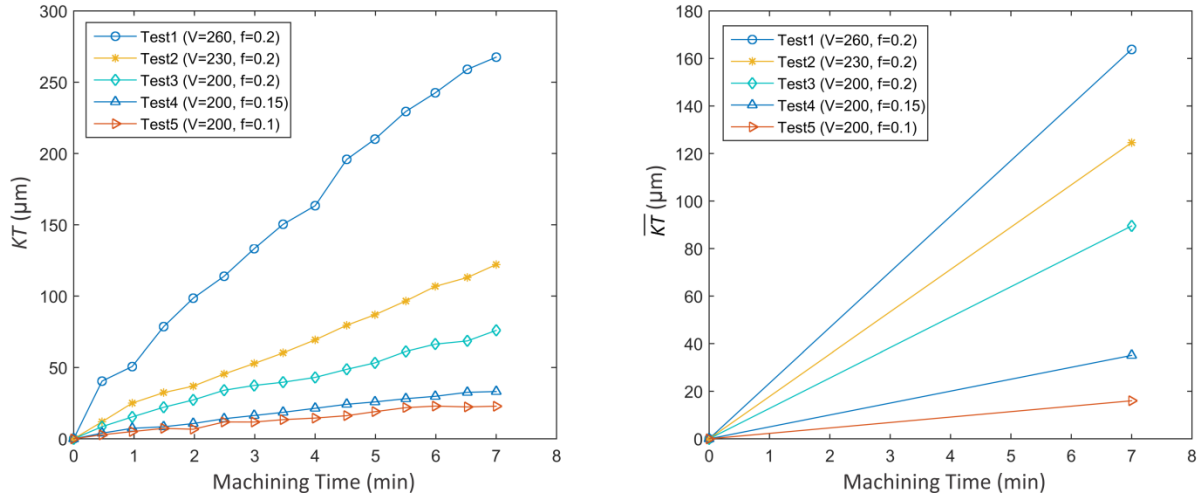


Fig. 7-2 Crater depth, Left: Measured crater depth,  $KT$ , in oblique turning [56] (machining settings:  $a_p=1.5\text{mm}$ ,  $\gamma_n = +1\text{deg}$ ,  $\lambda_s = +7\text{deg}$  and  $\kappa_r = +75\text{deg}$ ), Right: Predicted average crater depth,  $\bar{KT}$  (present work).

The second set of experiments is conducted by measuring the worn volume on a turning tool in orthogonal cutting tests. Fig. 7-3. Left shows the experimental results. The average crater volume can be predicted using the following equation

$$\bar{w}_{KT} = \dot{w} A_t t_m \quad (7-21)$$

In Eq. (7-21), it is assumed that the average wear rate is constant during machining which is confirmed by constant increase rates of measured wear volumes in Fig. 7-3. Left. The predicted average volume loss is plotted using Eq. (7-21) in Fig. 7-3. Right for corresponding machining conditions in Fig. 7-3. Right. As it can be seen in Fig. 7-3, the predicted average wear volume loss can simulate the behavior of the crater volume loss accurately.

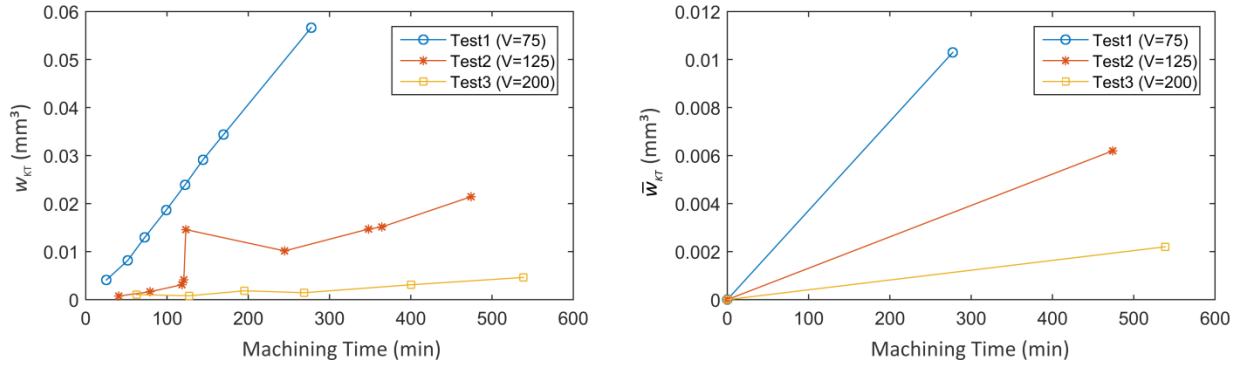


Fig. 7-3 Crater worn volume, Left: measured worn volume,  $w_{KT}$  [60] (machining settings:  $a_p=3\text{mm}$ ,  $\gamma_n=-6\text{deg}$ ,  $\lambda_s=0\text{deg}$ ,  $\kappa_r=+90\text{deg}$  and  $f=0.1\text{mm/rev}$ ), Right: Predicted average worn volume,  $\bar{w}_{KT}$  (present work).

The left and right plots in Fig. 7-2 and Fig. 7-3 are in different scale, which means the quantitative correlation is with discrepancy. However, the trendwise/qualitative correlation is promising. Table 7-2 and Fig. 7-2 and Fig. 7-3 confirm that the behavior of average interface temperature, crater depth, crater worn volume resemble well the trend of maximum interface temperature, crater depth, crater worn volume, respectively. These average values are then used to calculate average tool wear rate at each point along the cutting edge.

#### 7.4 Constructing optimization problems

In face-hobbing, it is desired that the cutting forces increase smoothly and gradually and then slowly fade down at the end of the process. Using constant deceleration for plunge feed of the cutting, the cutting forces suddenly reach to their maximum values in the first cutting cycle and then in third and fourth cycles decrease. This cutting force behavior exerts a sudden force shock on the cutting blades which results tool wear or breakage. In addition to this sudden force shock, discontinuous machining nature of face hobbing results in cutting force fluctuation applied on the blades.

In order to prevent the force shock and create smooth increase of the cutting forces, a modification in cutter head motion toward workpiece is applied. Instead of constant deceleration of the cutter head, deceleration is assumed linear. Therefore, the cutter head motion can be represented by a polynomial of third order as

$$BO(t) = BO_0 - (a_3 \cdot t^3 + a_2 \cdot t^2), \quad (7-22)$$

where  $t$  is the machining time and  $a_2$  and  $a_3$  are coefficients which are derived in the following. The cutter head axial velocity toward the workpiece in the beginning and end of the cutting stroke is assumed to be zero. Therefore, this assumption leads to

$$3 \cdot a_3 \cdot t_p^2 + 2 \cdot a_2 \cdot t_p = 0, \quad (7-23)$$

where  $t_p$  is the final machining time of the face-hobbing (plunge time). In addition,  $BO=0$  at  $t_p$ , therefore,

$$a_3 \cdot t_p^3 + a_2 \cdot t_p^2 = BO_0. \quad (7-24)$$

Eventually, solving Eqs. 23 and 24 leads to  $a_3 = \frac{-2BO_0}{t_p^3}$  and  $a_2 = \frac{3BO_0}{t_p^2}$ . Total machining time can be written as

$$t_m = t_p + t_i, \quad (7-25)$$

where  $t_i$  is the time duration that cutter head takes to finish all the gear slots at the end of plunge time. In this period, there is no plunge feed and the cutting blades finish the gear convex and concave teeth surfaces.  $t_i$  is considerably smaller than  $t_p$  and can be neglected in optimization procedure when the total machining time,  $t_m$ , is going to be minimized.

The goal of the optimization problems in face-hobbing is to find an appropriate plunge time,  $t_p$ ,

and cutter head angular velocity,  $\omega = \frac{d\theta}{dt}$ , so that the total machining time,  $t_m$ , is minimized and

tool life,  $t_L$ , is maximized. Minimizing  $t_m$  means minimizing, the plunge time,  $t_p$ . Therefore, any combination of values of  $t_p$  and  $\omega$ , creates an individual face-hobbing scenario.

Using the method presented in this paper, the average wear rate at any time instance during machining at any point on the cutting edge can be estimated. Therefore, maximum average wear



rate,  $\dot{w}$ , in any face-hobbing process can be obtained. Using obtained  $\dot{w}$ , the tool life,  $t_L$ , can be estimated as

$$t_L = \frac{\bar{w}_{all}}{\dot{w}_{max}} \quad (7-26)$$

where  $\bar{w}_{all}$  is the allowable crater wear after machining time,  $t_m=t_L$ . Since in Eq. (7-26) maximum wear rate is considered, predicted tool life,  $t_L$ , is underestimated. However, since the purpose of the present work is to find the appropriate machining settings, considering maximum wear rate for all face-hobbing scenarios will give us the optimum scenario.

Assuming a face-hobbing scenario is given ( $t_p$  and  $\omega$ ), then the total cutter head rotation angle for this scenario is calculated as  $\theta_p = \omega \cdot t_p$ . The number of gear slots that a specific blade is going to machine,  $n_{gs}$ , is calculated as  $n_{gs} = \frac{\theta_p}{2\pi}$ . The blade is engaged with each slot for  $\Delta\theta$  rotation of the cutting system. Therefore, the number of gears,  $n_G$ , that can be machined by the blade before the end of its life ( $t_L$ ), can be estimated as

$$n_G = \frac{\omega \cdot t_L}{n_{gs} \cdot \Delta\theta} \quad (7-27)$$

By substituting the equations of  $\theta_p$  and  $n_{gs}$  in Eq. (7-27), the formulation of  $n_G$  can be re-written as

$$n_G = \frac{2\pi t_L}{\Delta\theta \cdot t_p} \quad (7-28)$$

In other words, Eq. (7-28) gives the underestimated number of possible produced gears before regrading or changing the cutting blades. Therefore, in the optimization procedure,  $n_G$  is desired to be maximum which is equivalent to minimizing the maximum wear rate,  $\dot{w}$ , or maximizing the tool life,  $t_L$ . Eq. (7-28) is a simple looking formula that conveys complicated concept. In the optimization problem,  $t_p$  and  $\omega$  are treated as design variables. The tool life,  $t_L$ , is a function of  $t_p$  and  $\omega$  implicitly. Therefore,  $n_G$  is in terms of the design variables implicitly as well (

$n_g = n_g(t_p, \omega)$ ). Therefore, in order to estimate  $n_G$  for each face-hobbing scenario, cutting velocity, cutting forces, normal stress, interface temperature and wear rate must be calculated one after another. The semi-analytical methods presented in Chapters 5 and 6. This procedure can be done computationally efficiently in comparison with costly finite element method which makes the optimization practically impossible. Since in the optimization problem, many possible solutions are searched to finally reach to the optimum feasible solution, using the presented computationally efficient method is essential.

In order to make the whole optimization process automatic (finding the undeformed chip geometry, calculating cutting forces, normal stress, interface temperature and finally wear rate), the optimization process is implemented in MATLAB using “fmincon” optimization function. Since the objective function and constraints are in implicit forms, several “.m” files are prepared to input to “fmincon” function using the optimization algorithm as “interior-point”. Therefore, the search algorithm tries different face-hobbing scenarios and then using the calculated wear rate, it finds its search direction to minimize the objective function (plunge time) and satisfying the constraints (the wear rate or cutting force limit).

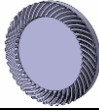
## 7.5 Case studies

In this section, two case studies are investigated to show the capability of the proposed methods in this paper in machining setting adjustment. Case I is conducted to control the produced cutting forces by changing the machining settings. The workpiece and cutting tool materials are selected as Ti<sub>6</sub>Al<sub>4</sub>V and tungsten carbide, respectively (Eq. (6-19)). The orthogonal cutting parameters are not velocity dependent since in Case I, the cutting velocity does not have large changes.

In Case II, machining settings are adjusted to reach maximum possible tool life and minimum machining time. The proposed methods to predict cutting forces normal stresses and interface temperature in the wear rate model, are applied in this case study. The workpiece material is AISI 1045 241HB. The orthogonal cutting parameters for this material, which are velocity dependent, are retrieved from CUTPRO® software [67].

Both case studies are conducted using the process settings listed in Table 7-3.

Table 7-3 The process parameters for case studies.

| Cutting System |          | Gear Blank       |  |
|----------------|----------|------------------|--|
| $h_f$          | 12 mm    | A                | 2.44 mm  |
| $r_e$          | 0.5 mm   | D                | 9.952 mm   |
| $L_t$          | 10 mm    | F                | 38 mm  |
| $\rho$         | 762 mm   | C                | 144.57 mm  |
| $\tau$         | 10 deg   | $\Gamma$         | 76.05 deg  |
| $k_e$          | 12 deg   | $N_g$            | 45   |
| $\alpha_c$     | 20 deg   | Machine Settings |  |
| $\eta_b$       | 4.42 deg | H                | 63.5206 mm   |
| $\gamma_2$     | 87 deg   | $V_p$            | 101.2954 mm  |
| $\alpha_c$     | 3 deg    | $\Delta X_p$     | 1.07 mm  |
| $N_b$          | 13       | $\gamma_m$       | 67.1114 deg  |
| $r_b$          | 76 mm    |                  |  |

\*Geometric parameters are computed using HYGEAR® software [68].

Table 7-4 summarizes machining settings for the case studies before and after optimization.

Table 7-4 Machining settings for case-studies, without and with optimization

| Machining settings      | Polynomial function of cutter head displacement ( $BO_0 - BO(t)$ ), mm | Plunge Time, $t_p$ , s | Cutter head angular velocity, $\omega$ RPM |
|-------------------------|--|------------------------|--|
| Without optimization    | Second order   | 32.71                  | 400  |
| Optimized Case Study I  | Third order  | 72.68                  | 400  |
| Optimized Case Study II | Third order  | >29                    | 900  |

### 7.5.1 Case I: Optimization considering cutting force limit

The purpose of this case study is to demonstrate the cutting force regulation in face-hobbing. In this problem, the process without optimization has a constant acceleration. Fig. 7-4 shows the displacement of the cutter head vs. time. The blue curve is the case without optimization. For the black curve, the cutter head acceleration is assumed linear but with the same plunge time as

constant acceleration scenario. Since the cutter head rotary speed for all cases are kept the same, cutting cycles happen at the same time for all cases. At each cutting cycle, an example of undeformed chip is shown in Fig. 7-4 along each displacement curve. Fig. 7-5 shows the predicted cutting forces for constant and linear accelerations. As it can be seen, with linear acceleration (black line) the cutting forces smoothly and gradually increase (this gradual increase is also reflected in undeformed chip geometry area ( $A_c$ ) in Fig. 7-4). However, the maximum cutting force (3.4 kN), which happens at the last cutting cycle (cutting cycle d), is 1 kN even higher than the maximum cutting force for the constant acceleration case.

In order to decrease the cutting forces for linear acceleration case, the optimization problem is solved to minimize the plunge time while keeping the maximum cutting forces less than a threshold value ( $F_{max} < F_{all} = 1.8$  kN). The solution is the red curve of displacement vs time in Fig. 4. The minimized machining time is about 73 sec. The predicted cutting forces for this solution are shown in Fig. 7-5. As it can be seen, the cutting forces increases very slowly and smoothly during 11 cutting cycle where the maximum force (1.8 kN) happens at the last cycle ( $k$ ).

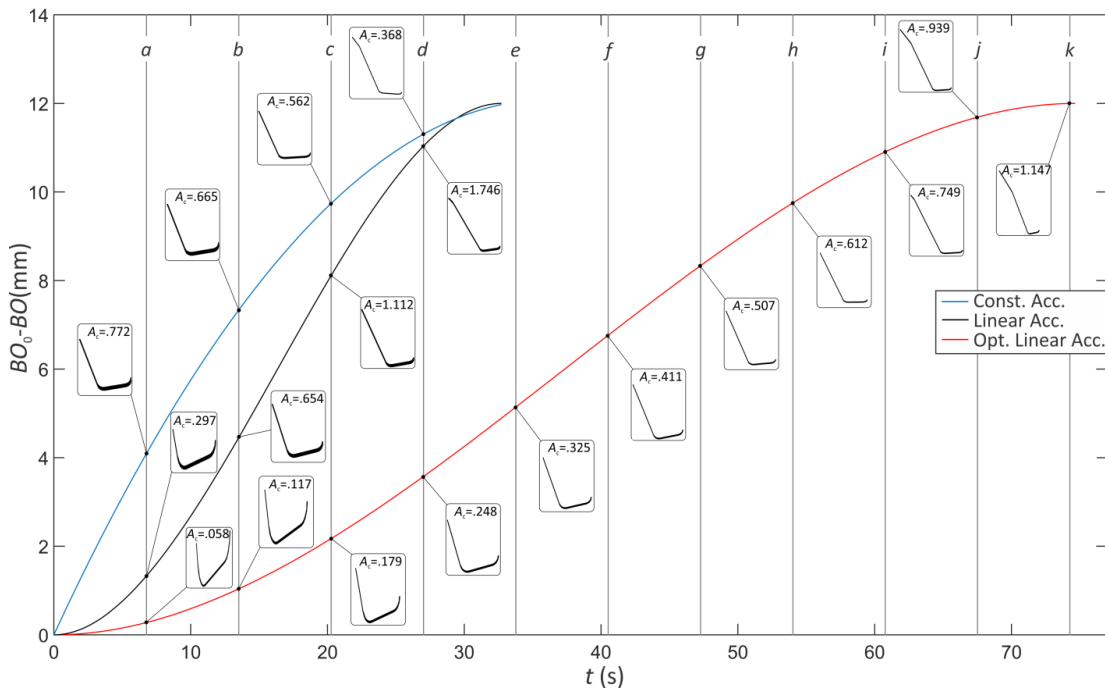


Fig. 7-4 Displacement of the cutter head towards the workpiece ( $BO_0 - BO$ ) with constant (Const. Acc.), linear (Linear Acc.) and optimized linear (Opt. Linear Acc.) acceleration, respectively.

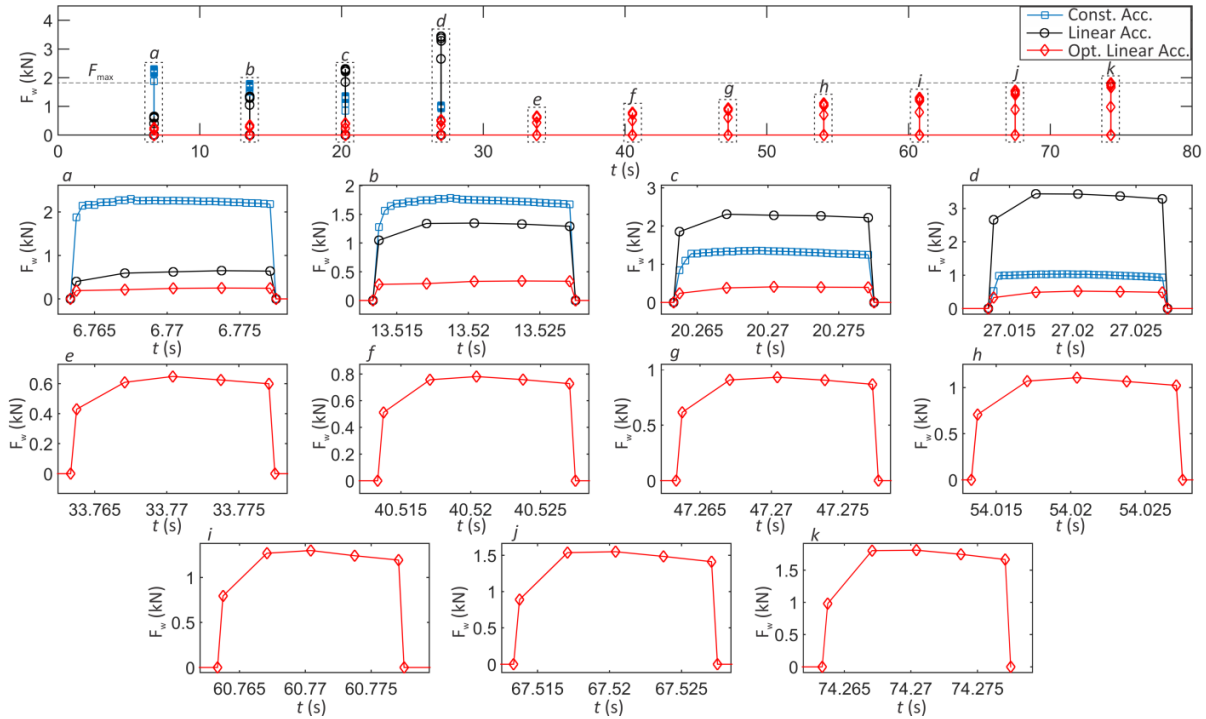


Fig. 7-5 Predicted cutting forces for constant (Const. Acc.), linear (Linear Acc.) and optimized linear (Opt. Linear Acc.) acceleration, respectively.

The value of  $F_{all}$  can be defined by experiments and measuring cutting forces and observing tool failure or by converting maximum allowable produced machining torque of the machine tool to the allowable produced cutting force.

### 7.5.2 Case II: Optimization considering tool wear

The maximum crater wear depth was suggested to be less than 0.1mm in literature [16]. This value is considered as the optimization constraint in such a way that crater depth must be less than this amount. Angular velocity of the cutter head and plunge time ranges are set as  $\omega \in [400, 900]$  RPM,  $t_p \in [0, 40]$  sec, respectively. Now the optimization process begins (an outside blade is considered for optimization of face-hobbing of a sample gear). Each combination of cutter head angular velocity and plunge time creates a single machining scenario. For different scenarios, a MATLAB® code obtain the maximum average tool wear rate ( $\dot{w}$ ) along the cutting edge (usually  $\dot{w}$  occurs at the tool tip and corner). Fig. 7-6 shows maximum wear rate vs. plunge time for different scenarios (each point represents a face-hobbing machining scenario).

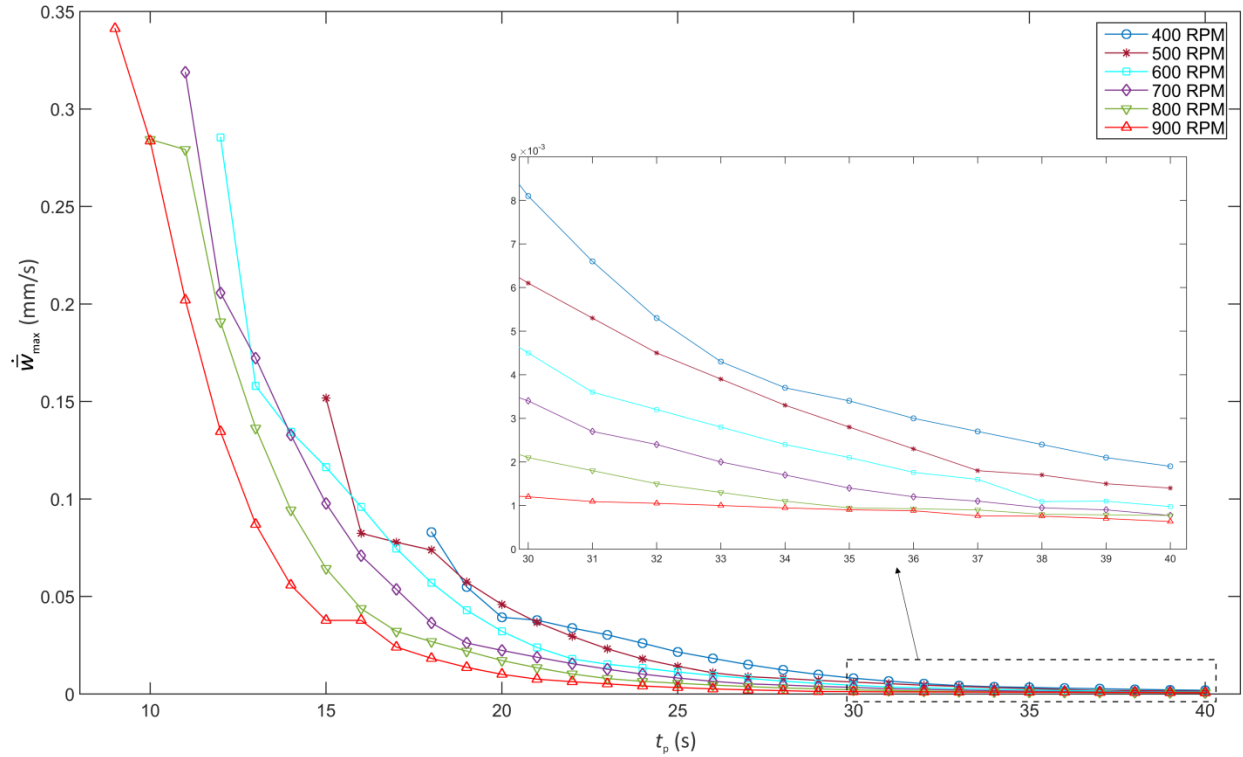


Fig. 7-6 Maximum average tool wear rate,  $\dot{W}$  .

For each cutter head angular velocity, the maximum wear rate behavior is quite predictable, increasing plunge time results in decreasing wear rate. Increasing angular velocity (increasing cutting speed) causes increasing in cutting forces and consequently the normal stress increases (assuming un-deformed chip geometry does not change). However, by increasing angular velocity, chip thickness decreases and consequently cutting forces and normal stress decrease. The effect of chip thickness reduction is more dominant than cutting velocity increase.

As it can be seen in Fig. 7-6, the minimum wear rate happens at 900 RPM, upper bound of the cutter head angular velocity,  $\omega$ . This phenomena shows that even at high cutting speeds, which generally expected to have higher cutting velocity, due to less un-deformed chip thickness (less un-deformed chip area), the wear rate decreases in comparison with lower cutter head angular velocities.

Tool life,  $t_L$ , and number of machined gears,  $n_G$ , for each face-hobbing scenario can be estimated using Eqs. (7-26) and (7-28). Fig. 7-7. Left and Right show  $t_L$  and  $n_G$  for different scenarios, respectively.

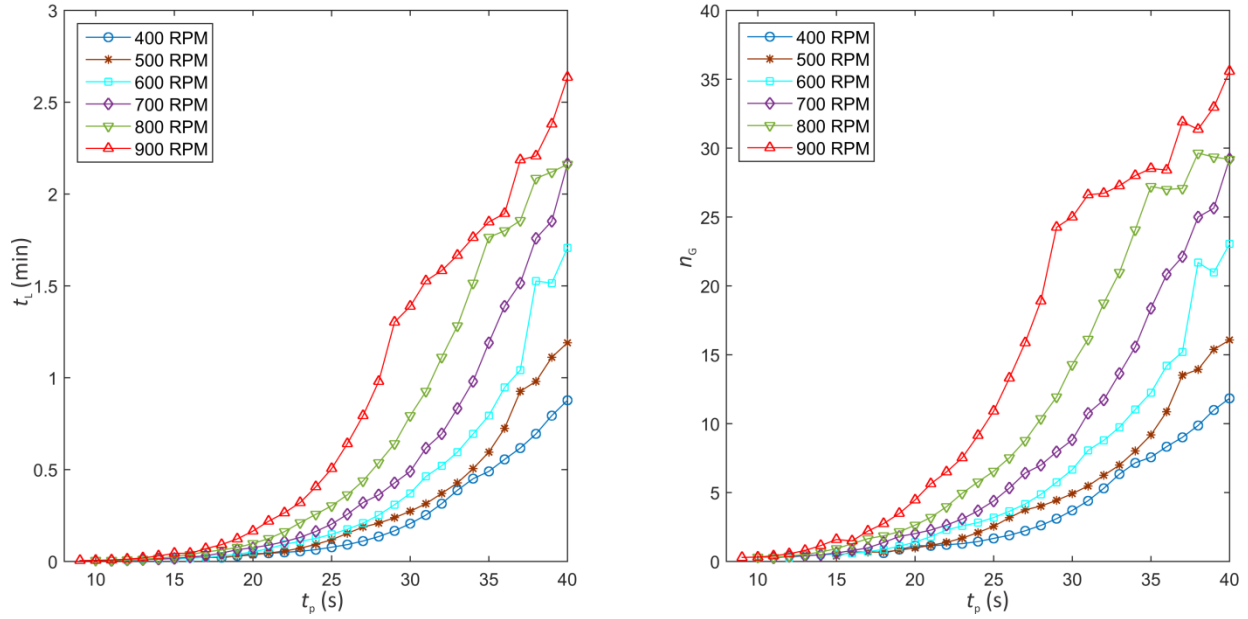


Fig. 7-7 Left: Tool life,  $t_L$ , Right: Number of machined gears,  $n_G$ .

At the upper bound of  $\omega$ ,  $t_L$  and  $n_G$  have the largest values in whole plunge time range. It means that in Case II, it is recommended to select the upper bound of  $\omega$ , 900 RPM in order to have longer tool life. In  $t_p \in [0, 29]$  sec, both  $t_L$  and  $n_G$  have parabolic curves. However, after 29 sec of plunge time ( $t_p \in [29, 40]$ ), they have approximately linear behavior. The solution of the optimization problem for Case II gives the upper bound for the cutter head angular velocity to satisfy the requirement to minimize the plunge time,  $t_p$ . Then, based on the production requirement (the number of machined gears,  $n_G$ ), the corresponding plunge time,  $t_p$ , with the upper bound of the angular velocity is chosen.

## 7.6 Conclusion

In the present paper, a semi-analytical approach is presented to predict the tool wear and select appropriate machining setting based on the constructed optimization problem. The objective functions and a constraint of the optimization problem are formulated semi-analytically. The plunge time is considered as the objective function to be minimized and the predicted total cutting force or average tool wear rate is treated as an inequality constraint.

In face-hobbing, the head cutter angular velocity increase results in un-deformed chip area decrease. This phenomenon causes decreases in total cutting force and also tool wear in the specific investigated case studies in this paper. In face-hobbing, when the cutter head angular velocity increases, it always causes un-deformed chip area to decrease (considering the same plunge time). However, the tool wear might sometimes increase by increasing cutting velocity and decreasing un-deformed chip area. Increasing cutting velocity causes an increase in cutting temperature generally which is making the tool wear worse. However, since the un-deformed chip area decreases as well, cutting forces and consequently normal stresses also decrease. Accumulating these two phenomena (rising cutting temperature and decreasing normal stress), results less tool wear for the specific range of cutter head angular velocity  $\omega \in [400, 900]$  RPM. It should also be noticed that, decreasing un-deformed chip area would not always cause the tool wear to decrease. In machining theory, it is well known that un-deformed chip thickness should be larger than cutter tool nose radius in order to have a cutting process instead of only so-called “ploughing” or “rubbing” process. Therefore, the tool wear is a complex phenomenon and for each face-hobbing scenario, the trend of the wear rate should be investigated separately.

Since the face-hobbing process mainly is conducted in dry-cut, the cutting force coefficients which have been retrieved from CUTPRO® software are for the dry-cut condition. These cutting force coefficients are actually obtained from simple turning experiments with different cutting speeds, feeds and rake angles. In these turning tests, cutting forces are measured and then the cutting force coefficients are estimated using curve fitting approaches like the least square method. The turning operations were conducted in dry condition and consequently the cutting force coefficients are valid only for dry-cut. These cutting force coefficients are used then to predict cutting forces, normal stress, interface temperature and tool wear rate.

In order to apply the method presented in this paper for the wet-cut condition, it is needed to obtain the cutting force coefficients using the specific cutting fluid which is going to be used. It means that simple turning operations are conducted under the wet condition and the cutting force coefficients are estimated using the measured cutting forces. Then, using the new set of cutting force coefficients, cutting forces, normal stress, interface temperature and finally tool wear rate can be predicted for wet-cut as well.

In the present work, the crater wear is considered; however, the flank wear can be also simulated using the proposed methods and machining settings can be optimized based on flank wear



constraint. However, the temperature on flank face should be derived using numerical methods and then plug in Usui's wear model.

The proposed method in the present work also can be implemented in cutting system design in face-hobbing. Optimum rake and relief angles can be suggested using the constructed optimization problem seeking longer tool life of the cutting blades. In addition, the present work is developed for the non-generated face-hobbing which is used for machining gears. The generated face-hobbing is widely used in machining pinions. The present study can be applied on the generated process as well. However, since the cutting surfaces in generated face-hobbing are more complicated than non-generated, new methods should be proposed to obtain the undeformed chip geometry in this process and then calculate cutting forces. When the cutting forces are predicted in generated face-hobbing, the tool wear also can be predicted and optimum machining settings can be selected. Despite the non-generated face-hobbing in which only two machining settings are found (plunge time and cutter head angular velocity), more machining settings and their functions should be found in generated process because of multi-axis machining of generated process.

# Chapter 8

## Summary, Contributions and Recommendations

### 8.1 Summary

In the present thesis, two main challenges, the tool wear and machining setting optimization, in industries using face-hobbing of bevel gears have been investigated. These two challenges impose excessive costs in related manufacturing industries for re-grinding and changing the cutting blades (tool wear related costs) and trial and error experiments (machining setting selection costs).

In order to improve the tool wear characteristics of the cutting blades, a new method for re-designing rake and relief surfaces of the cutting blades is proposed to reduce the gradients of the working rake and relief angles along the cutting edge of the blades, theoretically to zero. Based on the well-developed and experimentally approved mathematical characterization equation, the invented geometry of the cutting blades show better tool wear characteristics in comparison with the conventional blades, especially at the tool corner regions. At the tool corners, due to large variations in working rake and relief angles, the tool wear takes place faster for the conventional blades. However, in the invented blades, the gradients of these two angles remain zero along the cutting edge including the tool corner.

In addition, FEM machining analysis is conducted on the both conventional and re-designed blades. The results show that the cutting temperature is concentrated at the tool corner in the conventional blades while in the re-designed blades the temperature concentration is shifted away for the tool corner to the flanks. Moreover, the von mises stress distribution is concentrated at the tool corner for the conventional blade, however, for the re-designed blade, results show a more even stress distribution along the cutting edge.

In order to optimize the machining parameters in face-hobbing of bevel gears, a through and novel method is proposed based on minimizing the plunge time subject to the tool wear or cutting force constraints. Usui's wear rate model is selected to predict the crater depth for different face-hobbing scenarios. In order to implement the wear model in face-hobbing, cutting forces, normal stresses, interface temperature and sliding chip velocity are calculated along the cutting edge for each face-hobbing scenarios.

Cutting forces are predicted using a semi-analytical cutting force model which uses the un-deformed chip geometry, cutting force coefficients and machining parameters. In order to obtain the un-deformed chip geometry, two novel approaches are proposed, numerical and semi-analytical. In the numerical approach, first the instantaneous in-process model of the workpiece during face-hobbing is obtained and then using the in-process model, the un-deformed chip geometry is approximated. To do so, the workpiece is discretized into many disks and each disk is intersected with all the cutting blades moving around the workpiece and removing material from it. In the semi-analytical approach, a boundary theory of the un-deformed chip geometry in Formate® face-hobbing is proposed in such a way that the closed form formulations of the piecewise boundary curves of the un-deformed chip geometry are derived. Only the ranges of the curve parameters of the boundaries need to be calculated numerically. The semi-analytical method is computationally more efficient than the previous proposed numerical considerably.

The interface cutting temperature along the cutting edge is calculated based energy method which has been adopted in the case of face-hobbing. The sliding cutting velocity of the chip is calculated using the kinematics of the process and also the fundamental of the oblique cutting theory. In order to calculate the tool wear rate along the cutting edge of the blades in face-hobbing, the cutting edge and the un-deformed chip geometry are discretized into many differential oblique cuts. Then, for each small oblique cutting element, the tool wear rate along the cutting edge is estimated using calculated cutting forces, normal stresses, interface temperature and chip sliding velocity.

The optimization problem is constructed in such a way that the face-hobbing processing time (objective function) is minimized while the tool wear or the cutting forces are kept under specified limits (constraints). The methods are applied on two case studies to show the capability of the proposed optimization process. The plunge time, plunge function and angular velocity of

the cutter head are obtained for Formate® (non-generated face-hobbing) as the optimum solution of the constructed optimization problem.

## **8.2 Contributions**

The main contributions of the present research are:

- 1- A new method to design cutting blades in face-hobbing is introduced to improve the tool wear characteristics of the cutting blades. Based on the proposed method, a blade is invented based on the conventional design.
- 2- The instantaneous in-process model of the workpiece is obtained using a proposed numerical method in face-hobbing.
- 3- The boundary theory of the un-deformed chip geometry is constructed based on two proposed methods, numerical and semi-analytical.
- 4- Cutting forces are predicted in face-hobbing of bevel gears.
- 5- Machining parameters are optimized semi-analytically based on minimizing the processing time subject to the tool wear or cutting force constraints.

## **8.3 Future works**

The present research opens new horizons for further investigations in face-hobbing of bevel gears and also other machining processes. The projected future trends are described as follows:

- 1- Another geometrical related factor in the tool wear phenomena is the gradient of the un-deformed chip thickness along the cutting edge. The largest gradient occurs at the tool corner. If the un-deformed chip thickness remains constant, the tool wear characteristics are improved especially at the corner. Because of the complexity of the face-hobbing process, derivation and controlling un-deformed chip thickness along the cutting edge is challenging. This is the subject of the future research of the authors.
- 2- The proposed method to re-design cutting blades in face-hobbing can be applied to other cutting tools such as end mills or turning tools. The core concept the method which is keeping the working rake and relief angle constant can be extended to other cutting tool

in other machining processes and rake and the relief surfaces can be re-designed based on desired working rake or relief angle.

- 3- The present research is concentrated on non-generated (Formate®) face-hobbing. All the proposed methods are capable to be applied on the generated face-hobbing as well. In generated face-hobbing, the cutting surfaces have implicit mathematical representation while the cutting surfaces in non-generated processes have closed form equations. Although, more active machine tool axes are involved, the core ideas of the proposed methods can be applied for this process as well.
- 4- In the present work, the crater wear is considered; however, the flank wear can be also simulated using the proposed methods and machining settings can be optimized based on flank wear constraint. However, the temperature on flank face should be derived using numerical methods and then plug in Usui's wear model.
- 5- The proposed method in the present work also can be implemented in cutting system design in face-hobbing. Optimum rake and relief angles can be suggested using the constructed optimization problem seeking longer tool life of the cutting blades.

# References

- [1] Stadtfeld, H. J., Nov. 2001, Cutting tool for producing gears by Face hobbing, US Patent, Patent No.: US 6,311,590 B1.
- [2] CNN Tech Heroes: <http://advertisementfeature.cnn.com/tech-heroes/archive/hermann-stadtfeld/>
- [3] Fan, Q., 2005 Computerized Modeling and Simulation of Spiral Bevel and Hypoid Gears Manufactured by Gleason Face Hobbing Process, ASME J. Mech. Des., v 128, n 6, p 1315-1327 , DOI: 10.1115/1.2337316..
- [4] Shih, Y., Fong, Z. and Lin,G.C.Y., 2007, Mathematical model for a universal face hobbing hypoid gear generator, ASME J. Mech. Des., 129(1), pp. 38-47. DOI: 10.1016/j.cja.2013.05.005.
- [5] Vimercati, M., 2007 ,Mathematical Model for Tooth Surfaces Representation of Face-Hobbed Hypoid Gears and Its Application to Contact Analysis and Stress Calculation, Mechanism and Machine Theory, 42(6), pp. 668–690. DOI: 10.1016/j.mechmachtheory.20.
- [6] <http://www.thirdwavesys.com/research-and-development/>.
- [7] Radzevich, S. P., 2010, Gear Cutting Tools: Fundamentals of Design and Computation, CRC Press.
- [8] <http://www.gleason.com/products/148/119/pentac>, [Online].
- [9] Brecher, C., Klocke, F., Brumm, M. and Hardjosuwito A., 2013, Simulation Based Model for Tool Life Prediction in Bevel Gear Cutting, Computer Aided Engineering, DOI 10.1007/s11740-012-0439-x.
- [10] Brecher, C., Klocke, F., Brumm, M. and Hardjosuwito A., 2013, Analysis and Optimization of Bevel Gear Cutting Processes by Means of Manufacturing Simulation Simulation & Modeling Methodologies, Technologies & Appl., AISC 197, pp. 271–284. DOI: 10.1.

- [11] Brecher, C., Klocke, F., Schröder, T. and Rütjes, U., 2008, Analysis and Simulation of Different Manufacturing Processes for Bevel Gear Cutting, *Journal of Advanced Mechanical Design Systems and Manufacturing*, DOI: 10.1299/jamdsm.2.165..
- [12] Klein, A., 2007, A Spiral Bevel and Hypoid Gear Tooth Cutting with Coated Carbide Tools, Dissertation RWTH Aachen. ISBN 978-3-8322-6192-4..
- [13] Klocke, F., Schröder and T. and Klein, A., 2006, Tool Life and Productivity Improvement through Cutting Parameter Setting and Tool Design in High-Speed Bevel Gear Tooth Cutting, *Gear Technology*, pp. 40-49..
- [14] Klocke, F., Brumm, M. and Herzhoff, S., 2012, Influence of Gear Design on Tool Load in Bevel Gear Cutting, 5th CIRP Conference on High Performance Cutting. DOI: 10.1016/j.procir.2012.04.010.
- [15] Stadtfeld, H. J., 2014, Gleason Bevel Gear Technology: The Science of Gear Engineering and Modern Manufacturing Methods for Angular Transmissions, Chap. 2, 7 and 10, The Gleason Works, Rochester, NY. ISBN: 978-0-615-96492-8.
- [16] Usui, E, Shirakashi, S., Kitagawa, T., Analytical Prediction of Tool Wear, *Wear*, 100, 1984, 129–151. doi: 10.1016/0043-1648(84)90010-3..
- [17] Habibi, M., Chen, Z.C., 2016, A Semi-analytical Approach to Un-deformed Chip Boundary Theory and Cutting Force Prediction in Face-hobbing, *Computer Aided Design*, 73, pp. 53-65, doi: 10.1016/j.cad.2015.12.001..
- [18] Habibi, M., Chen, Z.C., 2015, An Accurate and Efficient Approach to Un-deformed Chip Geometry in Face-hobbing and its Application in Cutting Force Prediction, *ASME Journal of Mechanical Design*, 138(2):023302-023302-11, doi: 10.1115/1.4032090..
- [19] Habibi, M., Chen, Z.C., 2015, A New Approach to Blade Design with Constant Rake and Relief Angles for Face-hobbing of Bevel Gears, *ASME Journal of Manufacturing Science and Engineering*, 138(3):031005-031005-16, doi: 10.1115/1.4030936..
- [20] Habibi, M., Chen, Z.C., 2016, Machining Setting Optimization for Formate® Face-hobbing of Bevel Gears with the Tool Wear Constraint, *ASME Journal of Mechanical Design*, Submitted..

- [21] Fan, Q., 2007, Enhanced algorithms of contact simulation for hypoid gear drives produced by face-milling and face-hobbing processes, *ASME J. Mech. Des.*, 129(1), pp. 31-37. DOI: 10.1115/1.2359475.
- [22] Shih, Y., 2012, Mathematical Model for Face-Hobbed Straight Bevel Gears, *ASME J. Mech. Des.*, 134(9), pp. 1-11. DOI: 10.1115/1.4007151.
- [23] Habibi, M., Arezoo, B., Vahebinojedeh\*, M., 2011, Tool Deflection and Geometrical Error Compensation by Tool Path Modification, *International Journal of Machine Tools and Manufacture*, 51 (6), pp. 439-449, doi:10.1016/j.ijmachtools.2011.01.009..
- [24] Vahebinojedeh\*, M., Habibi, M., Arezoo, B., 2011, Tool Path Accuracy Enhancement through Geometrical Error Compensation, *International Journal of Machine Tools and Manufacture*, 51 (6), pp. 471-482, doi:10.1016/j.ijmachtools.2011.02.005..
- [25] Karunakaran, K.P., Shringi, R., 2008, A solid –based off-line adaptive controller for feed rate scheduling for milling process , *Journal of Materials Processing Technology*, 204(1-3), pp 384-396.
- [26] Oliver, J.H., Goodman, E.D., 1990, Direct dimensional NC verification, *Computer Aided Design*, 22( 1), pp 3–9.
- [27] Park, J. W., Shin, Y. H., Chung, Y. C., 2005, Hybrid cutting simulation via discrete vector model, *Computer-Aided Design*, 37( 4), pp 419–430.
- [28] Maeng, S.R., Baek, N., Shin, S.Y., Choi, B.K., 2003, A z-map update method for linearly moving tools, *Computer Aided Design*, 35( 11), pp 995–1009.
- [29] Spence, A., Altintas, Y., 1994, A solid modeler based milling process simulation and planning system, *ASME Journal of Engineering for Industry*, 116(1), pp 61–69.
- [30] Roth, D., Ismail, F., Bedi, S., 2003, Mechanistic modeling of the milling process using an adaptive depth buffer, *Computer Aided Design*, 30(8), pp 1-17.
- [31] Feng, H.Y., Menq, L.M., Chai, H., Hang, Z.L., 1995, The prediction of dimensional error for sculptured surface production using the ball-end milling process, *International Journal of Machine Tools & Manufacture*, 35( 8), pp 1149-1169.



- [32] Mounayri, H.E.I., Spence, A.D., Elbestwani, M.A., 1998, Milling process simulation-a generic solid modeller based paradigm, *ASME Journal of Manufacturing Science and Engineering*, 120(2), pp 213-221.
- [33] Habibi, M., Feb. 2010, Geometrical and tool deflection error compensation of 3-axis CNC machine tools by g-code modification, M.Sc. thesis, Amirkabir University of Technology (Tehran Polytechnic), Tehran, Iran.
- [34] Nikolaos, T., Aristomenis, A., 2012, CAD-based calculation of cutting force components in gear hobbing, *ASME Journal of Manufacturing Science and Engineering*, 134, pp 031009(1-8).
- [35] Vasilis, D., Nectarios, V., Aristomenis, A., 2007, Advanced computer aided design simulation of gear hobbing by means of three-dimensional kinematics modeling, *ASME Journal of Manufacturing Science and Engineering*, 129, pp 911-918.
- [36] Dimitriou, V., Antoniadis, A., 2009, CAD-based simulation of the hobbing process for the manufacturing of spur and helical gears, *The International Journal of Advanced Manufacturing Technology*, 41(3-4), pp 347-357.
- [37] Altintas, Y., 2012, *Manufacturing Automation: Metal Cutting Mechanics, Machine Tool Vibrations, and CNC Design*, Chap. 2, Cambridge University Press, Cambridge, UK. ISBN: 9781107001480.
- [38] Engin, S., Altintas, Y., 2001, Mechanics and dynamics of general milling cutters. Part I: helical end mills, *International Journal of Machine Tools & Manufacture*, 41(15), pp 2195–2212.
- [39] Soori, M., Arezoo, B., Habibi, M., 2015, Tool Deflection Error of Three-axis CNC Milling Machines, Monitoring and Minimizing by a Virtual Machining System, *ASME Journal of Manufacturing Science and Engineering*, doi:10.1115/1.4032393..
- [40] Soori, M., Arezoo, B., Habibi, M., 2014, Virtual Machining Considering Dimensional, Geometrical and Tool Deflection Errors in Three-axis CNC Milling Machines, *Journal of Manufacturing Systems*, 33(4), pp. 498-507, doi:10.1016/j.jmsy.2014.04.007..

- [41] Soori, M., Arezoo, B., Habibi, M., 2013, Dimensional and Geometrical Errors of Three-axis CNC Milling Machines in Virtual Machining System, *Computer Aided Design*, 45 (11), pp. 1306-1313, doi:10.1016/j.cad.2013.06.002..
- [42] Watanabe T. A, 1986, Model-Based Approach to Adaptive Control Optimization in Milling. *ASME. J. Dyn. Sys., Meas., Control.*;108(1), pp. 56-64. doi:10.1115/1.3143743..
- [43] Litvin, F.L. and Gutman, Y., 1981, Methods of Synthesis and Analysis for Hypoid Gear-Drives of “Formate” and “Helixform”, Part 1, 2, and 3 , *ASME J. Mech. Des.* 103 (1), pp. 83-113. doi:10.1115/1.3254891.
- [44] Wasif, M., 2012 A New Approach to CNC Programming for Accurate Multi-axis Face-Milling of Hypoid Gears, Ph.D. Dissertation, Concordia University, Montreal, Canada..
- [45] Fan, Q., 2005 Computerized Modeling and Simulation of Spiral Bevel and Hypoid Gears Manufactured by Gleason Face Hobbing Process, *ASME J. Mech. Des.*, v 128, n 6, p 1315-1327 , DOI: 10.1115/1.2337316..
- [46] Schrock, D.J., Kang, D., Bieler, T.R. and Kwon P., 2014, Phase Dependent Tool Wear in Turning Ti-6Al-4V Using Polycrystalline Diamond and Carbide Inserts, *ASME J. Manuf. Sci. Eng.* 136(4). DOI: 10.1115/1.4027674.
- [47] Wang, X. and Kwon P.Y., 2014, WC/Co Tool Wear in Dry Turning of Commercially Pure Aluminium, *ASME J. Manuf. Sci. Eng.*, 136(3). DOI: 10.1115/1.4026514.
- [48] Braglia, M. and Castellano, D., Diffusion Theory Applied to Tool-Life Stochastic Modeling Under a Progressive Wear Process, *ASME J. Manuf. Sci. Eng.* 136(3). DOI: 10.1115/1.4026841.
- [49] Attanasio, A., Ceretti, E., Giardini, C. and Cappellini, C., Tool Wear in Cutting Operations: Experimental Analysis and Analytical Models, *ASME J. Manuf. Sci. Eng.*, 135(5). DOI: 10.1115/1.4025010.
- [50] Bhushan, R.K., Multiresponse Optimization of Al Alloy-SiC Composite Machining Parameters for Minimum Tool Wear and Maximum Metal Removal Rate, *ASME J. Manuf. Sci. Eng.*, 135(2). DOI: 10.1115/1.4023454.

- [51] Vasilis, D., Nectarios, V., Aristomenis, 2007, A., Advanced computer aided design simulation of gear hobbing by means of three-dimensional kinematics modeling, *ASME Journal of Manufacturing Science and Engineering*, 129, pp 911-918.
- [52] Dimitriou, V., Antoniadis, A., 2009 CAD-based simulation of the hobbing process for the manufacturing of spur and helical gears, *The International Journal of Advanced Manufacturing Technology*, 41(3-4), pp. 347-357. DOI 10.1007/s00170-008-1465-x.
- [53] Antoniadis, A., 2012, Gear Skiving—CAD Simulation Approach, *Computer Aided Design*, 44(7), pp. 611–616. DOI:10.1016/j.cad.2012.02.003.
- [54] Wang, M., Ken, T., Du, S., Xi, L., Tool Wear Monitoring of Wiper Inserts in Multi-Insert Face Milling Using Three-Dimensional Surface Form Indicators. *ASME. J. Manuf. Sci. Eng.* 2015;137(3):031006-031006-8. doi:10.1115/1.4028924.
- [55] Li, B., A review of tool wear estimation using theoretical analysis and numerical simulation technologies, *International Journal of Refractory Metals and Hard Materials*, Volume 35, November 2012, Pages 143-151, ISSN 0263-4368, doi: 10.1016/j.ijrmhm.2012.0.
- [56] Yen, Y., Söhner, J., Lilly, B., Altan, T, Estimation of tool wear in orthogonal cutting using the finite element analysis, *Journal of Materials Processing Technology*, Volume 146, Issue 1, 15 February 2004, Pages 82-91, ISSN 0924-0136, doi: 10.1016/S0924-0.
- [57] Attanasio, A.A., Ceretti, E.E., Giardini, C.C., Cappellini, C.C., Tool Wear in Cutting Operations: Experimental Analysis and Analytical Models. *ASME. J. Manuf. Sci. Eng.* 2013;135(5):051012-051012-11. doi:10.1115/1.4025010.
- [58] Kuttolamadom, M.A, Laine, M.M., Kurfess, T.R., On the Volumetric Assessment of Tool Wear in Machining Inserts With Complex Geometries—Part 1: Need, Methodology, and Standardization. *ASME. J. Manuf. Sci. Eng.* 2012;134(5):051002-051002-8. doi:10.1115/1.4007.
- [59] Kuttolamadom, M.A., Laine, M.M., Kurfess, T.R., Burger, U., Bryan, A. On the Volumetric Assessment of Tool Wear in Machining Inserts With Complex Geometries—Part II: Experimental Investigation and Validation on Ti-6Al-4V. *ASME. J. Manuf. Sci. Eng.* 2012;134.

- [60] Binder, M., Klocke, F., Lung, D., Tool wear simulation of complex shaped coated cutting tools, *Wear*, Volumes 330–331, May–June 2015, Pages 600-607, ISSN 0043-1648, doi:10.1016/j.wear.2015.01.015.
- [61] Islam, C., Lazoglu, I., Altintas, Y., A Three-Dimensional Transient Thermal Model for Machining. *ASME. J. Manuf. Sci. Eng.* 2015;138(2):021003-021003-17. doi:10.1115/1.4030305.
- [62] Ding, H., Shin, Y.C., A Metallo-Thermomechanically Coupled Analysis of Orthogonal Cutting of AISI 1045 Steel. *ASME. J. Manuf. Sci. Eng.* 2012;134(5):051014-051014-12. doi:10.1115/1.4007464.
- [63] Ivester, R. W., Kennedy, M., Davies, M., Stevenson, R., Thiele, J., Furness, R., and Athavale, S., 2000, Assessment of Machining Models: Progress Report, *Mach. Sci. Technol.*, 4(3), pp. 511–538.
- [64] Lalwani, D. I., Mehta, N. K., and Jain, P. K., 2009, Extension of Oxley's Predictive Machining Theory for Johnson and Cook Flow Stress Model, *J. Mater. Process. Technol.*, 209(12–13), pp. 5305–5312.
- [65] Karpat, Y., and Ozel, T., 2006, Predictive Analytical and Thermal Modeling of Orthogonal Cutting Process—Part I: Predictions of Tool Forces, Stresses, and Temperature Distributions, *ASME J. Manuf. Sci. Eng.*, 128(2), pp. 435–444.
- [66] Iqbal, S. A., Mativenga, P. T., and Sheikh, M. A., 2007, Characterization of Machining of AISI 1045 Steel Over a Wide Range of Cutting Speeds. Part 1: Investigation of Contact Phenomena, *Proc. Inst. Mech. Eng., Part B*, 221, pp. 909–916.
- [67] <http://www.malinc.com/products/cutpro/> (retrieved orthogonal cutting parameters)
- [68] <http://hygears.com/> (calculated face-hobbing machine settings)

# **Appendix**

## **Permissions to Reproduce Copyrighted Material**

This appendix contains the permissions obtained from ASME and Elsevier publishers allowing the reproduction of the copyrighted material presented in Chapters 3-7.

**ELSEVIER LICENSE  
TERMS AND CONDITIONS**

Apr 04, 2016

This is a License Agreement between mohsen habibi ("You") and Elsevier ("Elsevier") provided by Copyright Clearance Center ("CCC"). The license consists of your order details, the terms and conditions provided by Elsevier, and the payment terms and conditions.

**All payments must be made in full to CCC. For payment instructions, please see information listed at the bottom of this form.**

|  |  |
|--|--|
| Supplier                                     | Elsevier Limited<br>The Boulevard, Langford Lane<br>Kidlington, Oxford, OX5 1GB, UK  |
| Registered Company Number                    | 1982084  |
| Customer name                                | mohsen habibi  |
| Customer address                             | 1433 Towers St.<br>Montreal, QC H3H2E3   |
| License number                               | 3842031358069  |
| License date                                 | Apr 04, 2016   |
| Licensed content publisher                   | Elsevier   |
| Licensed content publication                 | Computer-Aided Design  |
| Licensed content title                       | A semi-analytical approach to un-deformed chip boundary theory and cutting force prediction in face-hobbing of bevel gears |
| Licensed content author                      | Mohsen Habibi, Zezhong Chevy Chen  |
| Licensed content date                        | April 2016   |
| Licensed content volume number               | 73   |
| Licensed content issue number                | n/a  |
| Number of pages                              | 13   |
| Start Page                                   | 53   |
| End Page                                     | 65   |
| Type of Use                                  | reuse in a thesis/dissertation   |
| Portion                                      | full article   |
| Format                                       | electronic   |
| Are you the author of this Elsevier article? | Yes  |
| Will you be translating?                     | No   |
| Title of your thesis/dissertation            | Tool Wear Improvement and Machining Parameter Optimization in Non-generated Face-hobbing of Bevel Gears                    |
| Expected completion date                     | May 2016   |
| Estimated size (number of pages)             | 140  |
| Elsevier VAT number                          | GB 494 6272 12   |
| Permissions price                            | 0.00 CAD   |
| VAT/Local Sales Tax                          | 0.00 CAD / 0.00 GBP  |

Total 0.00 CAD

[Terms and Conditions](#)

### INTRODUCTION

1. The publisher for this copyrighted material is Elsevier. By clicking "accept" in connection with completing this licensing transaction, you agree that the following terms and conditions apply to this transaction (along with the Billing and Payment terms and conditions established by Copyright Clearance Center, Inc. ("CCC"), at the time that you opened your Rightslink account and that are available at any time at <http://myaccount.copyright.com>).

### GENERAL TERMS

2. Elsevier hereby grants you permission to reproduce the aforementioned material subject to the terms and conditions indicated.
3. Acknowledgement: If any part of the material to be used (for example, figures) has appeared in our publication with credit or acknowledgement to another source, permission must also be sought from that source. If such permission is not obtained then that material may not be included in your publication/copies. Suitable acknowledgement to the source must be made, either as a footnote or in a reference list at the end of your publication, as follows:  
"Reprinted from Publication title, Vol /edition number, Author(s), Title of article / title of chapter, Pages No., Copyright (Year), with permission from Elsevier [OR APPLICABLE SOCIETY COPYRIGHT OWNER]." Also Lancet special credit - "Reprinted from The Lancet, Vol. number, Author(s), Title of article, Pages No., Copyright (Year), with permission from Elsevier."
4. Reproduction of this material is confined to the purpose and/or media for which permission is hereby given.
5. Altering/Modifying Material: Not Permitted. However figures and illustrations may be altered/adapted minimally to serve your work. Any other abbreviations, additions, deletions and/or any other alterations shall be made only with prior written authorization of Elsevier Ltd. (Please contact Elsevier at [permissions@elsevier.com](mailto:permissions@elsevier.com))
6. If the permission fee for the requested use of our material is waived in this instance, please be advised that your future requests for Elsevier materials may attract a fee.
7. Reservation of Rights: Publisher reserves all rights not specifically granted in the combination of (i) the license details provided by you and accepted in the course of this licensing transaction, (ii) these terms and conditions and (iii) CCC's Billing and Payment terms and conditions.
8. License Contingent Upon Payment: While you may exercise the rights licensed immediately upon issuance of the license at the end of the licensing process for the transaction, provided that you have disclosed complete and accurate details of your proposed use, no license is finally effective unless and until full payment is received from you (either by publisher or by CCC) as provided in CCC's Billing and Payment terms and conditions. If full payment is not received on a timely basis, then any license preliminarily granted shall be deemed automatically revoked and shall be void as if never granted. Further, in the event that you breach any of these terms and conditions or any of CCC's Billing and Payment terms and conditions, the license is automatically revoked and shall be void as if never granted. Use of materials as described in a revoked license, as well as any use of the materials beyond the scope of an unrevoked license, may constitute copyright infringement and publisher reserves the right to take any and all action to protect its copyright in the materials.
9. Warranties: Publisher makes no representations or warranties with respect to the licensed material.
10. Indemnity: You hereby indemnify and agree to hold harmless publisher and CCC, and their respective officers, directors, employees and agents, from and against any and all claims arising out of your use of the licensed material other than as specifically authorized pursuant to this license.
11. No Transfer of License: This license is personal to you and may not be sublicensed,

assigned, or transferred by you to any other person without publisher's written permission.

12. **No Amendment Except in Writing:** This license may not be amended except in a writing signed by both parties (or, in the case of publisher, by CCC on publisher's behalf).

13. **Objection to Contrary Terms:** Publisher hereby objects to any terms contained in any purchase order, acknowledgment, check endorsement or other writing prepared by you, which terms are inconsistent with these terms and conditions or CCC's Billing and Payment terms and conditions. These terms and conditions, together with CCC's Billing and Payment terms and conditions (which are incorporated herein), comprise the entire agreement between you and publisher (and CCC) concerning this licensing transaction. In the event of any conflict between your obligations established by these terms and conditions and those established by CCC's Billing and Payment terms and conditions, these terms and conditions shall control.

14. **Revocation:** Elsevier or Copyright Clearance Center may deny the permissions described in this License at their sole discretion, for any reason or no reason, with a full refund payable to you. Notice of such denial will be made using the contact information provided by you. Failure to receive such notice will not alter or invalidate the denial. In no event will Elsevier or Copyright Clearance Center be responsible or liable for any costs, expenses or damage incurred by you as a result of a denial of your permission request, other than a refund of the amount(s) paid by you to Elsevier and/or Copyright Clearance Center for denied permissions.

#### LIMITED LICENSE

The following terms and conditions apply only to specific license types:

15. **Translation:** This permission is granted for non-exclusive world **English** rights only unless your license was granted for translation rights. If you licensed translation rights you may only translate this content into the languages you requested. A professional translator must perform all translations and reproduce the content word for word preserving the integrity of the article.

16. **Posting licensed content on any Website:** The following terms and conditions apply as follows: Licensing material from an Elsevier journal: All content posted to the web site must maintain the copyright information line on the bottom of each image; A hyper-text must be included to the Homepage of the journal from which you are licensing at <http://www.sciencedirect.com/science/journal/xxxxx> or the Elsevier homepage for books at <http://www.elsevier.com>; Central Storage: This license does not include permission for a scanned version of the material to be stored in a central repository such as that provided by Heron/XanEdu.

Licensing material from an Elsevier book: A hyper-text link must be included to the Elsevier homepage at <http://www.elsevier.com>. All content posted to the web site must maintain the copyright information line on the bottom of each image.

**Posting licensed content on Electronic reserve:** In addition to the above the following clauses are applicable: The web site must be password-protected and made available only to bona fide students registered on a relevant course. This permission is granted for 1 year only. You may obtain a new license for future website posting.

17. **For journal authors:** the following clauses are applicable in addition to the above:

#### Preprints:

A preprint is an author's own write-up of research results and analysis, it has not been peer-reviewed, nor has it had any other value added to it by a publisher (such as formatting, copyright, technical enhancement etc.).

Authors can share their preprints anywhere at any time. Preprints should not be added to or enhanced in any way in order to appear more like, or to substitute for, the final versions of articles however authors can update their preprints on arXiv or RePEc with their Accepted Author Manuscript (see below).

If accepted for publication, we encourage authors to link from the preprint to their formal publication via its DOI. Millions of researchers have access to the formal publications on



ScienceDirect, and so links will help users to find, access, cite and use the best available version. Please note that Cell Press, The Lancet and some society-owned have different preprint policies. Information on these policies is available on the journal homepage.

**Accepted Author Manuscripts:** An accepted author manuscript is the manuscript of an article that has been accepted for publication and which typically includes author-incorporated changes suggested during submission, peer review and editor-author communications.

Authors can share their accepted author manuscript:

- immediately
  - o via their non-commercial person homepage or blog
  - o by updating a preprint in arXiv or RePEc with the accepted manuscript
  - o via their research institute or institutional repository for internal institutional uses or as part of an invitation-only research collaboration work-group
  - o directly by providing copies to their students or to research collaborators for their personal use
  - o for private scholarly sharing as part of an invitation-only work group on commercial sites with which Elsevier has an agreement
- after the embargo period
  - o via non-commercial hosting platforms such as their institutional repository
  - o via commercial sites with which Elsevier has an agreement

In all cases accepted manuscripts should:

- link to the formal publication via its DOI
- bear a CC-BY-NC-ND license - this is easy to do
- if aggregated with other manuscripts, for example in a repository or other site, be shared in alignment with our hosting policy not be added to or enhanced in any way to appear more like, or to substitute for, the published journal article.

**Published journal article (JPA):** A published journal article (JPA) is the definitive final record of published research that appears or will appear in the journal and embodies all value-adding publishing activities including peer review co-ordination, copy-editing, formatting, (if relevant) pagination and online enrichment.

Policies for sharing publishing journal articles differ for subscription and gold open access articles:

**Subscription Articles:** If you are an author, please share a link to your article rather than the full-text. Millions of researchers have access to the formal publications on ScienceDirect, and so links will help your users to find, access, cite, and use the best available version. Theses and dissertations which contain embedded PJAs as part of the formal submission can be posted publicly by the awarding institution with DOI links back to the formal publications on ScienceDirect.

If you are affiliated with a library that subscribes to ScienceDirect you have additional private sharing rights for others' research accessed under that agreement. This includes use for classroom teaching and internal training at the institution (including use in course packs and courseware programs), and inclusion of the article for grant funding purposes.

**Gold Open Access Articles:** May be shared according to the author-selected end-user license and should contain a [CrossMark logo](#), the end user license, and a DOI link to the formal publication on ScienceDirect.

Please refer to Elsevier's [posting policy](#) for further information.

18. **For book authors** the following clauses are applicable in addition to the above:

Authors are permitted to place a brief summary of their work online only. You are not allowed to download and post the published electronic version of your chapter, nor may you scan the printed edition to create an electronic version. **Posting to a repository:** Authors are

permitted to post a summary of their chapter only in their institution's repository.

**19. Thesis/Dissertation:** If your license is for use in a thesis/dissertation your thesis may be submitted to your institution in either print or electronic form. Should your thesis be published commercially, please reapply for permission. These requirements include permission for the Library and Archives of Canada to supply single copies, on demand, of the complete thesis and include permission for Proquest/UMI to supply single copies, on demand, of the complete thesis. Should your thesis be published commercially, please reapply for permission. Theses and dissertations which contain embedded PJAs as part of the formal submission can be posted publicly by the awarding institution with DOI links back to the formal publications on ScienceDirect.

#### **Elsevier Open Access Terms and Conditions**

You can publish open access with Elsevier in hundreds of open access journals or in nearly 2000 established subscription journals that support open access publishing. Permitted third party re-use of these open access articles is defined by the author's choice of Creative Commons user license. See our [open access license policy](#) for more information.

#### **Terms & Conditions applicable to all Open Access articles published with Elsevier:**

Any reuse of the article must not represent the author as endorsing the adaptation of the article nor should the article be modified in such a way as to damage the author's honour or reputation. If any changes have been made, such changes must be clearly indicated.

The author(s) must be appropriately credited and we ask that you include the end user license and a DOI link to the formal publication on ScienceDirect.

If any part of the material to be used (for example, figures) has appeared in our publication with credit or acknowledgement to another source it is the responsibility of the user to ensure their reuse complies with the terms and conditions determined by the rights holder.

#### **Additional Terms & Conditions applicable to each Creative Commons user license:**

**CC BY:** The CC-BY license allows users to copy, to create extracts, abstracts and new works from the Article, to alter and revise the Article and to make commercial use of the Article (including reuse and/or resale of the Article by commercial entities), provided the user gives appropriate credit (with a link to the formal publication through the relevant DOI), provides a link to the license, indicates if changes were made and the licensor is not represented as endorsing the use made of the work. The full details of the license are available at <http://creativecommons.org/licenses/by/4.0>.

**CC BY NC SA:** The CC BY-NC-SA license allows users to copy, to create extracts, abstracts and new works from the Article, to alter and revise the Article, provided this is not done for commercial purposes, and that the user gives appropriate credit (with a link to the formal publication through the relevant DOI), provides a link to the license, indicates if changes were made and the licensor is not represented as endorsing the use made of the work. Further, any new works must be made available on the same conditions. The full details of the license are available at <http://creativecommons.org/licenses/by-nc-sa/4.0>.

**CC BY NC ND:** The CC BY-NC-ND license allows users to copy and distribute the Article, provided this is not done for commercial purposes and further does not permit distribution of the Article if it is changed or edited in any way, and provided the user gives appropriate credit (with a link to the formal publication through the relevant DOI), provides a link to the license, and that the licensor is not represented as endorsing the use made of the work. The full details of the license are available at <http://creativecommons.org/licenses/by-nc-nd/4.0>.

Any commercial reuse of Open Access articles published with a CC BY NC SA or CC BY NC ND license requires permission from Elsevier and will be subject to a fee.

Commercial reuse includes:

- Associating advertising with the full text of the Article
- Charging fees for document delivery or access
- Article aggregation
- Systematic distribution via e-mail lists or share buttons

Posting or linking by commercial companies for use by customers of those companies.

**20. Other Conditions:**

v1.8

**Questions? [customercare@copyright.com](mailto:customercare@copyright.com) or +1-855-239-3415 (toll free in the US) or +1-978-646-2777.**

---

---



Mohsen Habibi <mohsen.habibi.mech@googlemail.com>

---

## Permission Request for Two papers (MD-15-1391 and MANU-14-1658)

2 messages

---

Mohsen Habibi <mohsen.habibi.mech@googlemail.com>

Mon, Apr 4, 2016 at 1:25 PM

To: permissions@asme.org, Chevy Chen <zcchen@encs.concordia.ca>

Dear ASME,

I am writing to you to request for permission to use two of my published ASME papers out of my Ph.D. studies in my manuscript based Ph.D. thesis. These two papers are:

1- Habibi, M., Chen, Z.C., 2016, "An Accurate and Efficient Approach to Un-deformed Chip Geometry in Face-hobbing and its Application in Cutting Force Prediction", *ASME Journal of Mechanical Design*, MD-15-1391, 138(2):023302-023302-11, doi: 10.1115/1.4032090

2- Habibi, M., Chen, Z.C., 2016, "A New Approach to Blade Design with Constant Rake and Relief Angles for Face-hobbing of Bevel Gears", *ASME Journal of Manufacturing Science and Engineering*, MANU-14-1658, 138(3):031005-031005-16, doi: 10.1115/1.4030936

The permission request forms for each paper are attached.


Thank you for your help.

Best,  
Mohsen

Mohsen Habibi  
Research Assistant, Ph.D. Candidate,  
CAD/CAM Lab. EV 12.165,  
Mechanical and Industrial Engineering Department,  
Concordia University,  
Montreal, Quebec, Canada, H3G 1M8  
Office: (514)-848-2424 ext. 7948  
Mobile: (514)-826-7071

---

### 2 attachments

 permission-form\_MANU.pdf  
207K

 permission-form\_DESIGN.pdf  
208K

---

Beth Darchi <DarchiB@asme.org>

Wed, Apr 6, 2016 at 11:45 AM

To: Mohsen Habibi <mohsen.habibi.mech@googlemail.com>

Dear Prof. Habibi:

It is our pleasure to grant you permission to use **all or any part of** the following ASME papers:

- An Accurate and Efficient Approach to Undeformed Chip Geometry in Face-Hobbing and Its Application in Cutting Force Prediction, by Mohsen Habibi and Zezhong Chevy Chen, J. Mech. Des 138(2), 2015
- A New Approach to Blade Design With Constant Rake and Relief Angles for Face-Hobbing of Bevel Gears, by Mohsen Habibi and Zezhong Chevy Chen, J. Manuf. Sci. Eng 138(3), 2015

cited in your letter for inclusion in a Ph.D. Thesis entitled Tool Wear Improvement and Machining Parameter Optimization in Non-generated Face-Hobbing of Bevel Gears to be published by Concordia University.

Permission is granted for the specific use as stated herein and does not permit further use of the materials without proper authorization. Proper attribution must be made to the author(s) of the materials. **Please note:** if any or all of the figures and/or Tables are of another source, permission should be granted from that outside source or include the reference of the original source. ASME does not grant permission for outside source material that may be referenced in the ASME works.

As is customary, we request that you ensure full acknowledgment of this material, the author(s), source and ASME as original publisher. Acknowledgment must be retained on all pages printed and distributed.

Many thanks for your interest in ASME publications.

Sincerely,



**Beth Darchi**

Publishing Administrator

ASME

2 Park Avenue, 6th Floor

New York, NY 10016-5990

Tel 1.212.591.7700

[darchib@asme.org](mailto:darchib@asme.org)

**From:** Mohsen Habibi [mailto:[mohsen.habibi.mech@googlemail.com](mailto:mohsen.habibi.mech@googlemail.com)]

**Sent:** Monday, April 4, 2016 1:26 PM

## CV

### Mohsen Habibi

#### Education

- Aug. 2012 – May 2016                      Ph.D., Mechanical Engineering, Concordia University, Canada.
- Sep. 2007 – Feb. 2010                      M.Sc., Mechanical Engineering, Amirkabir University of Technology (Tehran Polytechnic), Iran.
- Sep. 2003 – Sep. 2007                      B.Sc., Mechanical Engineering, University of Mazandaran, Iran.

#### Papers in refereed journals

- J1 Habibi, M.**, Chen, Z.C., 2016, “A Semi-analytical Approach to Un-deformed Chip Boundary Theory and Cutting Force Prediction in Face-hobbing”, *Computer Aided Design*, 73, pp. 53-65, doi: 10.1016/j.cad.2015.12.001.
- J2 Habibi, M.**, Chen, Z.C., 2015, “An Accurate and Efficient Approach to Un-deformed Chip Geometry in Face-hobbing and its Application in Cutting Force Prediction”, *ASME Journal of Mechanical Design*, 138(2):023302-023302-11, doi: 10.1115/1.4032090.
- J3 Habibi, M.**, Chen, Z.C., 2015, “A New Approach to Blade Design with Constant Rake and Relief Angles for Face-hobbing of Bevel Gears”, *ASME Journal of Manufacturing Science and Engineering*, 138(3):031005-031005-16, doi: 10.1115/1.4030936.
- J4 Soori\***, M., Arezoo, B., **Habibi, M.**, 2015, “Tool Deflection Error of Three-axis CNC Milling Machines, Monitoring and Minimizing by a Virtual Machining System”, *ASME Journal of Manufacturing Science and Engineering*, doi:10.1115/1.4032393.
- J5 Soori\***, M., Arezoo, B., **Habibi, M.**, 2014, “Virtual Machining Considering Dimensional, Geometrical and Tool Deflection Errors in Three-axis CNC Milling Machines”, *Journal of Manufacturing Systems*, 33(4), pp. 498-507, doi:10.1016/j.jmsy.2014.04.007.
- J6 Soori\***, M., Arezoo, B., **Habibi, M.**, 2013, “Dimensional and Geometrical Errors of Three-axis CNC Milling Machines in Virtual Machining System”, *Computer Aided Design*, 45 (11), pp. 1306-1313, doi:10.1016/j.cad.2013.06.002.
- J7 Habibi, M.**, Arezoo, B., Vahebinojedeh\*, M., 2011, “Tool Deflection and Geometrical Error Compensation by Tool Path Modification”, *International Journal of Machine Tools and Manufacture*, 51 (6), pp. 439-449, doi:10.1016/j.ijmactools.2011.01.009.
- J8 Vahebinojedeh\***, M., **Habibi, M.**, Arezoo, B., 2011, “Tool Path Accuracy Enhancement through Geometrical Error Compensation”, *International Journal of Machine Tools and Manufacture*, 51 (6), pp. 471-482, doi:10.1016/j.ijmactools.2011.02.005.
- J9 Habibi, M.**, Shahmohammadi, H., Taraghi, V., Dinachali, S.S., Arezoo, B., 2009, “A Prototype Two-Axis Laser Scanning System used in Stereolithography Apparatus with New Algorithms for Computerized Model Slicing”, *American Journal of Applied Sciences*, 6 (9), pp. 1701-1707, doi: 10.3844/ajassp.2009.1701.1707.

#### Submitted papers in refereed journals

- S1 Habibi, M.**, Chen, Z.C., 2016, “Machining Setting Optimization for Face-hobbing of Bevel Gears with the Tool Wear Constraint”, *ASME Journal of Mechanical Design*, Submitted.
- S2 Habibi, M.**, Chen, Z.C., 2016, “A Universal Method to Five-axis Grinding of End Mills with Free-form Grinding Wheels”, *Computer Aided Design*, Submitted.